DISSERTATION

MAGNETIC FLUX DYNAMICS IN SUPERCONDUCTING FILMS STUDIED BY SCANNING HALL PROBE MICROSCOPY

Submitted by

Gheorghe Stan

Physics

In partial fulfillment of the requirements

For the Degree of Doctor of Philosophy

Colorado State University

Fort Collins, Colorado

Spring 2005

ProQuest Information and Learning Company
300 North Zeeb Road
P.O. Box 1346
Ann Arbor, MI 48106-1346

COLORADO STATE UNIVERSITY

February 4, 2005

WE HEREBY RECOMMEND THAT THE **DISSERTATION** PREPARED UNDER OUR SUPERVISION BY GHEORGHE STAN ENTITLED “MAGNETIC FLUX DYNAMICS IN SUPERCONDUCTING FILMS STUDIED BY SCANNING HALL PROBE MICROSCOPY ” BE ACCEPTED AS FULFILLING IN PART REQUIREMENTS FOR THE DEGREE OF DOCTOR OF PHILOSOPHY.

Committee on Graduate Work

Adviser Stuart Field

Department Head David A. Krueger

ABSTRACT OF **DISSERTATION**

MAGNETIC FLUX DYNAMICS IN SUPERCONDUCTING FILMS STUDIED BY SCANNING HALL PROBE MICROSCOPY

In this thesis we address two different issues in the field of flux dynamics in superconductors with constricted geometry. In our experiments we used scanning Hall probe microscopy to investigate the magnetic field profile above the samples' surface.

In the first experiment, *Vortex Nucleation in Narrow Thin-Film Strips*, we studied the magnetic flux nucleation in type-II superconducting thin-film strips of mesoscopic width. The maximum magnetic field below which vortices are completely expelled from niobium narrow thin-film strips was measured for different widths. Above this threshold field we examined the field dependence of the vortex density for the studied strips.

In the second experiment, *The Superconducting Dripping Faucet*, we analyzed, in microbridge geometry, the dynamics of the magnetic flux nucleation in a one-dimensional type-I superconducting channel. For this experiment we have developed a novel high-bandwidth Hall probe to detect in real time the nucleation and subsequent motion of the magnetic flux tubes along a fabricated one-dimensional channel in a lead film. The complex dynamics exhibited by the flux tubes nucleating from one end of the channel shares many characteristics of the well-known dripping faucet experiment. Nonlinear time series analysis was used to investigate the dynamics of the flux tubes in our experiment.

Gheorghe Stan
Physics Department
Colorado State University
Fort Collins, CO 80523
Spring 2005

Acknowledgments

After four years of working with Stuart, I would choose him as my advisor if I had to start again. We worked together to build experiments, find solutions, do physics, and have fun. Stuart helped me put together my research work and define my goals. I learned from him to be demanding and persistent in my career and look at details but not forget the whole. I thank him now for having me around, teaching me, and guiding me these years.

I address special thanks to my committee members, Siu Au Lee, Carmen Menoni, Robert Leisure, and Martin Gelfand, for their kindness and help that they gave to me.

My family, especially my wife Cristina, supported me in accomplishing this degree.

Dedication

To Cristina and Sonia.

Contents

List of Figures

List of Tables

Chapter 1

Introduction

Since the discovery of superconductivity in 1911 by Kamerlingh Onnes [1], a tremendous amount of work has been devoted to understanding the physics of the magnetic properties of superconducting materials. Many applications based on unique behavior of superconductors in a magnetic field have been developed since then, including superconducting magnets, transmission lines, levitated trains, superconducting quantum interference devices, magnetic resonance imaging of the human body, and many others.

As is well known, superconductors have zero electrical resistance and perfect diamagnetism (i.e., screening against external magnetic fields) in fields smaller than the so-called *lower critical field.* For magnetic fields between this lower critical field and the *upper critical field*, above which the material becomes normal, the magnetic field penetrates inside the superconducting sample in the form of normal flux regions. Within this higher magnetic field range, the coexistence between the superconducting and normal regions is called the *intermediate state* in type-I superconductors and the *mixed* (or *vortex*) *state* in type-II superconductors. This distinction comes from the way in which the flux penetrates inside the superconductor: either in the form of multi-quantized structures called normal domains (type-I) or singly-quantized flux lines called vortices (type-II).

The dynamics of flux lines constitutes an open area of intense research into the fundamentals and applications of superconducting materials. Much of the interest in studying the dynamics of flux lines is provided by a practical issue: when an electric current causes the motion of flux lines, then an electric resistance is induced and the superconductivity is destroyed. Over the years, the investigation of microscopic interactions between flux lines and pinning centers (material defects, artificial patterings) has continuously improved our knowledge in fabricating superconducting devices. More recently, the possibility of fabricating superconducting materials at micron and submicron scales has provided new superconducting devices: vortex pumps, superconducting ratchets, and superconducting quantum-bits. In such devices it is possible to manipulate and control the motion of flux lines along engineered patterns.

As part of the investigation of the magnetic flux structures in superconducting materials, much effort was devoted to developing and improving techniques for observing individual flux lines. A direct image of the flux line configuration gives us a better understanding of the microscopic interactions that determine the macroscopic response of the superconductor in an applied magnetic field.

During my Ph.D. program at Colorado State University I used the technique of scanning Hall probe microscopy to study the flux dynamics in superconducting samples of low dimensionality. The investigation of flux configurations in mesoscopic superconductors has been motivated by current technological applications. In this thesis I will focus on two experiments:

- Magnetic flux nucleation and vortex dynamics in narrow type-II superconducting thin-film strips.
- Dynamics of the magnetic flux nucleation in type-I microbridges. For reasons that will become clear, we have called this experiment the "superconducting dripping faucet."

Chapter 2 provides an overview of research on the dynamics of magnetic flux lines in superconductors. Flux dynamics in superconductors exhibits a rich variety of phenomena, capturing attention from both theoretical and practical standpoints. In the last few years, new fields of study have been emerged in this area, since it is now possible to control and manipulate flux lines at the submicron scale.

In **Chapter 3** we present a short review of several important magnetic imaging techniques that measure the local magnetic field above the surface of superconducting samples. Each technique has its own advantages and drawbacks and a comparison between these techniques is done in terms of their magnetic field and spatial sensitivities.

The scanning Hall probe microscopy used in our lab is presented in **Chapter 4**. An in-house manufactured scanning Hall probe microscope operates inside of a helium cryostat. Details about Hall probe fabrication are also provided in the main part of this chapter.

Chapter 5 is devoted to the first experiment mentioned above. The performance of superconducting devices is hindered by the noise induced by the presence of vortices. One solution to this problem is to design devices with leads narrow enough to expel the ambient fields, so the device contains no vortices. Using scanning Hall probe microscopy, we have measured the maximum field for which vortices are completely expelled from narrow strips made of niobium thin-film. We found that this maximal field scales with the inverse square of the strip's width and is almost independent of material parameters. Above this threshold field vortices nucleate into the strip with a density increasing approximately linearly with the field.

Chapter 6 is devoted to the second experiment. In a constricted geometry (a microbridge design), we investigated the dynamics of flux tubes in the current-induced resistive state of a type-I superconducting strip. We have developed a novel high-bandwidth Hall probe to detect the nucleation and subsequent motion of the magnetic flux tubes (containing many flux quanta) along a fabricated one-dimensional (1D) channel in a lead film. By reducing the dimensionality, we can obtain a direct understanding of the dynamics of individual flux tubes that would otherwise be difficult to observe in a system with so many degrees of freedom. It turns out that the dynamics of current-driven flux tubes shares many characteristics of the well-known dripping water faucet experiment. A model in terms of a Gibbs free energy barrier is proposed to explain aspects of this nonlinear dynamics exhibited by current-driven flux tubes.

Chapter 2

Dynamics of Magnetic Flux Lines in Superconductors

In this Chapter a short introduction to current research on the dynamics of magnetic flux lines in superconductors will be provided. This is the general framework into which our research fits. Besides theoretical models and computational modeling, direct experimental measurements provide valuable information on the static configurations and dynamics of magnetic flux lines in superconductors.

2.1 Magnetic Flux Structures in Superconductors

As is well known, two important length parameters characterize a superconducting material: the coherence length ξ and the penetration depth λ. The coherence length ($\xi \approx$ 1–100 nm) gives the characteristic length over which the order parameter (the wavefunction of the superelectrons) of the superconducting region changes at a normal-superconducting interface. The penetration length ($\lambda \approx$ 50–200 nm) measures the typical distance of the magnetic field decay at the separation between a normal and a superconducting region. The ratio between these two parameters is directly related to the surface energy associated with the boundary between the normal and superconducting regions. The separation of the two fundamental superconducting classes is done according to whether their surface energy is positive (type-I) or negative (type-II). In the framework of Ginzburg-Landau theory [2] it can be shown that the exact crossover from positive to negative surface energy is given by the value of the Ginzburg-Landau parameter $\kappa = \lambda/\xi$, with type-I superconductors having $\kappa < 1/\sqrt{2}$, while type-II superconductors are characterized by $\kappa > 1/\sqrt{2}$.

Type-I superconductors. Type-I superconductors have zero resistance and act as perfect diamagnetic materials (the *Meissner state*) for applied magnetic fields below the thermodynamical critical field H_c. Above H_c, they become normal materials. This description is valid only for a long rod-shape or sheet parallel to the applied magnetic field (see Fig. 2.1a); in this case the demagnetization factor due to the sample shape is zero, and the magnetic field at the surface sample equals the applied field. Things are more complicated when the demagnetization factor is not zero, because the field at some parts of the surface will exceed the applied field, causing the appearance of some normal regions, even though the applied field is less than the critical field H_c. For example (see Fig. 2.1b), in the Meissner state the equatorial field of a sphere is 3/2 the applied field. This will cause the first flux penetration inside of a superconducting sphere at a field of $2H_c/3$. In fields slightly higher than $2H_c/3$,

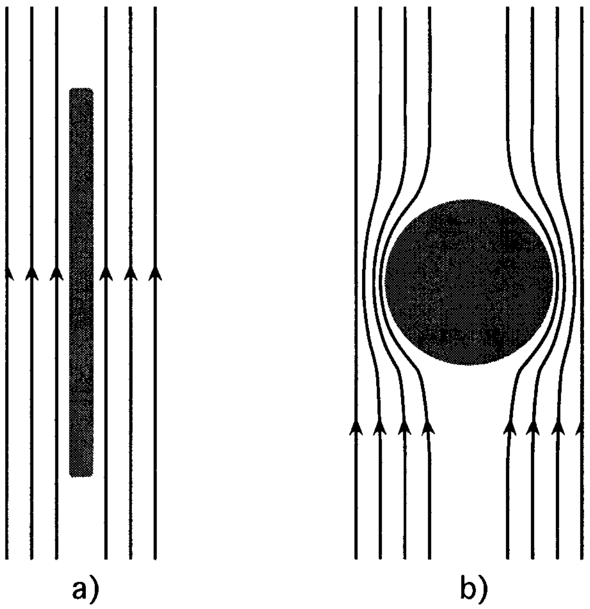

Figure 2.1: Full Meissner state occurs in fields: a) less than H_c for superconductor having zero demagnetization coefficient and b) less than $2H_c/3$ for a superconducting sphere.

flux starts penetrating at the equator where the field just equals H_c. However, once it penetrates, the field strength drops, so it is less than H_c. This would again favor the Meissner state. The only consistent solution is for a state to form which consists of alternating normal and superconducting regions; in the normal regions the field equals H_c. This is called the *intermediate state.*

In general, for ellipsoidal shapes, the intermediate state happens for applied magnetic fields H in the range [3]

$$(1-\eta)H_c < H < H_c, \tag{2.1}$$

where η is the demagnetization factor. The demagnetization factor is zero for a long, thin cylinder or thin plate in a parallel field (in which case there is no intermediate

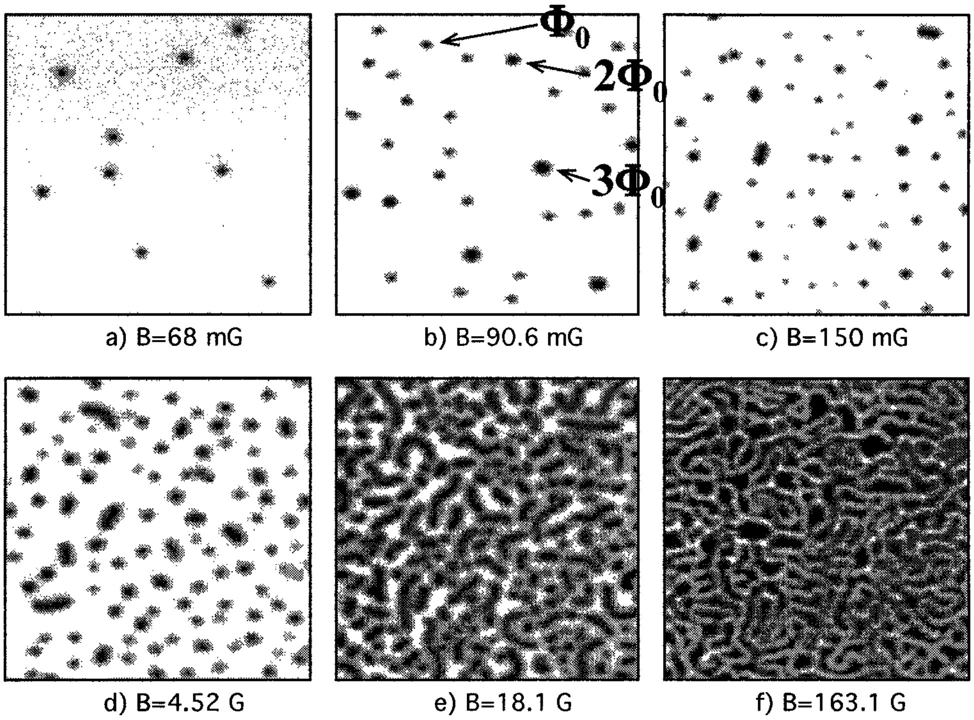

a) B=68 mG b) B=90.6 mG c) B=150 mG

d) B=4.52 G e) B=18.1 G f) B=163.1 G

Figure 2.2: Evolution of flux-containing regions (black) in a type-I lead film in an increasing magnetic field applied perpendicular on the film at 6.0 K: a) flux tubes of singly-quantum Φ_0; b) flux tubes of multiple Φ_0; c) and d) coalescing flux tubes; e) flux tubes and corrugated domains; f) branching structure of the normal-superconducting interface; $\Phi_0 = 2.07 \times 10^{-7}$ G cm^2.

state), 1/3 for a sphere, 1/2 for a cylinder in a transverse field, and 1 for an infinite flat slab in a perpendicular field. This means that in the common case of a film in a perpendicular field, the intermediate state is always present even at very small applied magnetic fields.

The magnetic flux configurations of the intermediate state of a type-I superconductor manifest as a complex pattern. In Fig. 2.2 we present several images provided by our scanning Hall probe microscope above a type-I lead film in an increasing external magnetic field. As the applied field is increased, these characteristic magnetic structures evolve from flux tubes containing many flux quanta (at low fields), to corrugations, then into a branching structure, and finally into superconducting tubes (at high fields).

The first theoretical description of the domain structure in the intermediate state was made by Landau [4], before any experimental observations. In this model, the intermediate state of a type-I superconducting slab placed in a perpendicular magnetic field is assumed to consist of a periodic array of straight superconducting and normal domains. However, experimental observations of the magnetic structures in the intermediate state display a complex pattern formed by a disordered set of intricate branched and fingered macroscopic domains like in Fig. 2.2f. This is because the competition between the magnetic field energy of the domains and the surface energy between the superconducting and normal regions causes the superconducor-normal interfaces to have a dynamically unstable evolution when the flux penetrates inside. Consequently, the flux penetrates in form of ramified domains rather than regular shapes. Typical examples of these patterns have been observed by Bitter decoration [5], scanning Hall probe microscopy [6], and magneto-optical imaging [7].

Using time-dependent Ginzburg-Landau theory, Goldstein *et al.* [8] and Dorsey *et al.* [9] proposed a more realistic treatment for the shapes of the magnetic structures

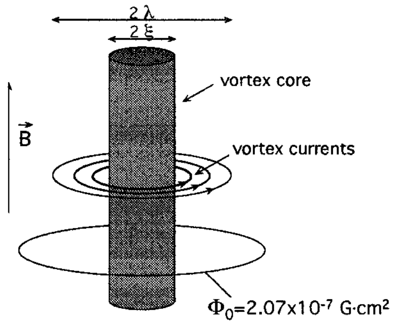

Figure 2.3: A vortex consists of a normal hard core surrounded by shielding supercurrents. The core radius is approximately the coherence length ξ and the circulating supercurrents decay from the vortex core over the penetration depth λ. Any contour of radius $r \gg \lambda$ encircling the axis of the vortex encloses one flux quantum Φ_0.

in the intermediate state. In this model, branched and fingered patterns like those observed in experiments arise from the competition between the long-range Biot-Savart interactions of the currents encircling each normal region and the superconductor-normal surface energy.

Type-II superconductors. A type-II superconductor is in the Meissner state (perfect diamagnetism) for applied fields less than the *lower critical field* H_{c1}, which is always less than the thermodynamical critical field H_c. Type-II superconductors become completely normal materials only above an *upper critical field* H_{c2}, which is significantly higher than the critical field H_c. For an applied magnetic field in the range $H_{c1} < H < H_{c2}$ type-II superconductors are in what is called *mixed* (or *vortex) state.* In the mixed state, the superconductor is no longer a perfect diamagnetic material.

The magnetic flux penetrates a type-II superconductor in the form of long, normal filaments parallel to the applied magnetic field, each filament containing exactly one flux quantum $\Phi_0 = hc/2e = 2.07 \times 10^{-7}$ G cm^2, where $h = 6.6 \times 10^{-27}$erg s is the Planck's constant, $c = 3 \times 10^{10}$cm/s is the speed of light, and $e = 4.8 \times 10^{-10}$ esu is the electron charge. The units are in c.g.s system. As is illustrated in Fig. 2.3, each filament (or *vortex*) is surrounded by a cylindrical vortex of supercurrents. In the mixed state, the energy associated with the normal-superconducting interface is negative. Thus, type-II superconductors lower their energy by creating as much normal-superconducting interface as possible when the flux penetrates inside. This favors the smallest possible flux structure, which has the quantum of Φ_0.

Vortices repel each other through their shielding currents. Consequently, at a field higher than H_{c1} vortices form, in a clean sample, a triangular array. This was predicted for the first time by Abrikosov [10] and is called the *Abrikosov vortex lattice.* Fig. 2.4 shows a scanning Hall probe image taken with our microscope over a niobium type-II superconducting film with the magnetic field applied perpendicular to the film's surface. Because niobium has an inherently strong pinning, the vortices are prevented from forming a regular triangular lattice. The entire magnetic flux threading the superconductor in the mixed state is found inside the vortices. The average magnetic flux density is then $\langle B \rangle = n_V \Phi_0$, where n_V is the density of the vortices. Thus as the field is increased the vortex density becomes greater and greater, and at the upper critical field H_{c2} the normal cores of vortices overlap and the entire sample goes normal.

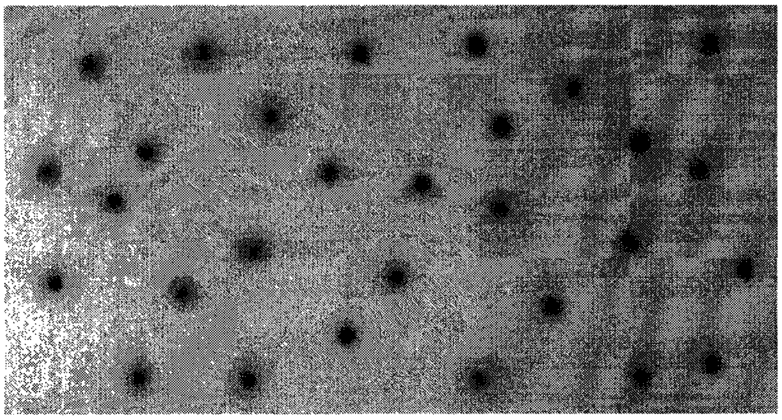

Figure 2.4: A typical scanning Hall image showing the magnetic field profile above of a niobium film. As in any type-II superconductor, magnetic flux penetrates in form of vortices.

Experimentally, the Abrikosov lattice of vortices in type-II superconductors has been imaged using Bitter decoration [11, 12], scanning tunneling microscopy [13], Lorentz microscopy [14], magnetic force microscopy [15], scanning superconducting quantum interference device microscopy [16], scanning Hall probe microscopy [17], and magneto-optical imaging [18].

2.2 Magnetic Flux Dynamics in Superconductors

2.2.1 Flux tube dynamics in type-I superconductors

Flux motion in a type-I superconductor in the intermediate state can be induced by an electrical current density **J**. Under the influence of the Lorentz force $\mathbf{F}_L = \mathbf{J} \times \mathbf{\Phi}/c$, a magnetic flux structure $\mathbf{\Phi}$ will move in a direction perpendicular to the current and the magnetic field (see Fig. 2.5). According to Faraday's law

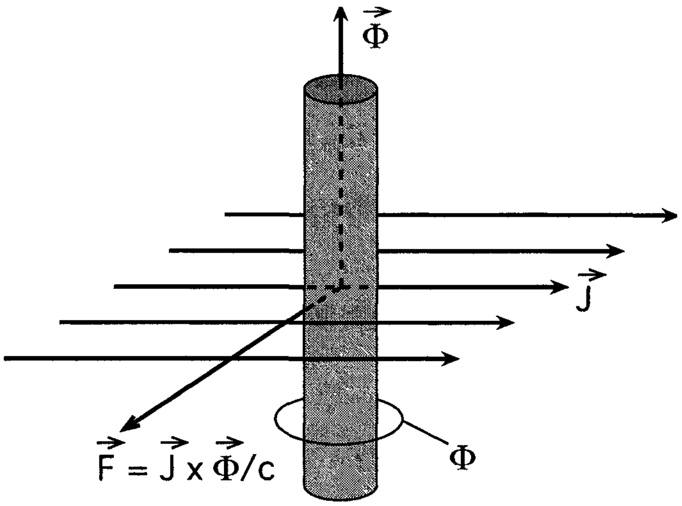

Figure 2.5: Lorentz force $\mathbf{F} = \mathbf{J} \times \mathbf{\Phi}/c$ exerted on a tube of flux Φ by a transport current $\mathbf{J}$.

curl $\mathbf{E} = -(1/c)\partial\mathbf{\Phi}/\partial t$, the flux change $\partial\mathbf{\Phi}/\partial t$ generates an electric field perpendicular to the flux motion and parallel to the current. Thus, a voltage drop can be measured along the current direction and the superconductor is no longer resistanceless. The first descriptions of flux flow as a resistive mechanism in a type-I superconducting wire were made by London (static model) [19] and (dynamical model) [20] for a current flowing along a wire. In this model, for currents exceeding a critical current, the superconducting wire becomes divided into a cylindrically symmetric mixture of normal and superconducting domains. As the current is increased, the normal-state region expands and this gives rise to the electrical resistance.

In a planar geometry, edge effects play an important role in the dynamics of the flux flow. In a type-I superconducting strip, at low currents, Meissner currents flow along the edges [21, 22]. These Meissner currents shield the magnetic field due to the applied current. However, when the magnetic field of the applied current exceeds the critical field at the sample edges, normal regions will start to form at different locations along the edges [23]. These normal regions grow and extend toward the center of the strip. Therefore, normal flux channels are formed across the strip as the current is further increased. Magneto-optical imaging showed that the channels of normal flux consist of trains of moving flux tubes, with each flux tube containing hundreds of single-flux quanta [24]. In the voltage-current characteristic, each new flux-tube train nucleated across the strip gives rise to a step in the voltage [23, 25].

The dynamics of a single flux-tube train flowing along a 1D channel has been studied in type-I superconducting strips having a microbridge constricted geometry. The microbridge is defined across the strip as a few-micron-wide weak link between two adjacent bulk superconducting regions. By applying a current along the strip, the flux tubes will nucleate and move along the link. The periodic flux-tube flow along such a 1D channel was studied by stroboscopic magneto-optical detection [26] and time-resolved measurements of the flux-flow voltage [27].

Using scanning Hall probe microscopy we have analyzed, in a microbridge geometry, the current-driven dynamics of the magnetic flux nucleation in a 1D type-I superconducting channel. Not only the periodic regime was investigated as in the previous experiments, but the entire dynamics of the flux tube-flow determined by the variation of a dc current perpendicular to the channel. This is presented in Chapter 6.

2.2.2 Vortex dynamics in type-II superconductors

A rich and interesting dynamics is developed by vortices when a current density $\mathbf{J}$ is passed through a type-II superconductor that is in the mixed (vortex) state. At a given temperature and a given magnetic field, the equilibrium configuration of vortices is determined by the competition between two different contributions: repulsive vortex-vortex interactions and attractive vortex-pinning interactions. When vortices are driven by a current, a vortex line will also experience a Lorentz force per unit length perpendicular to the current direction given by

$$\mathbf{F} = \mathbf{J} \times \mathbf{\Phi_0}/c, \tag{2.2}$$

$\mathbf{\Phi_0}$ being a vector along the flux filament and having the magnitude of a flux quantum. A vortex trapped by a pinning center will move as soon as the driving Lorentz force exceeds the maximum force due to the pinning and nearby vortices. The sample then enters into the flux flow regime and vortices move through the sample.

As was explained at the beginning of this section, the motion of a normal flux line in an applied magnetic field causes energy dissipation. This energy-dissipating motion of vortices can be viewed as a viscous damping. A good approximation for the viscous damping is to consider that the viscous force per unit length of a moving vortex line is proportional to the vortex velocity v_ϕ, so that $\mathbf{f} = -\eta \mathbf{v}_\phi$; η is called the viscous drag coefficient.

The general behavior of vortices in the flux flow regime is described by two basic models. An early simple model was developed by Bardeen and Stephen [28].

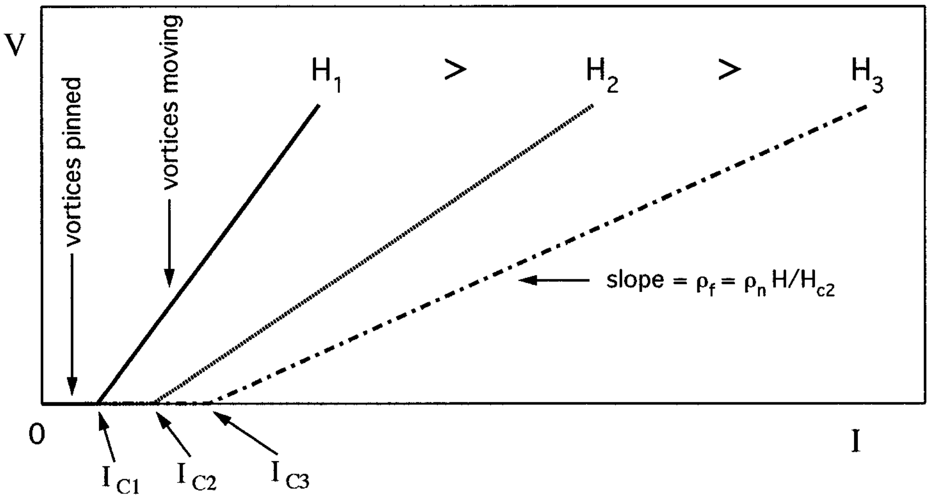

Figure 2.6: The field dependence of the current-voltage characteristics in the mixed state.

In this model the flux flow regime is characterized by the field-dependent flux flow resitivity $\rho_f = \rho_n H/H_{c2}$ and the vortex velocity $v_\phi = \Phi_0 J/\eta$, ρ_n being the normal resistivity. A more rigorous model based on the time-dependent Ginzburg-Landau theory was subsequently developed [29, 30, 31]. In Fig. 2.6 is shown the basic field dependence of the current-voltage characteristic for the flux flow regime. The current at which the superconductor first enters the flux flow regime is called the *critical current* I_c, and is determined by the pinning landscape of each sample; it is also temperature and field dependent. As the field is increased the vortices start to move at lower currents (low critical current) and the flux flow resistivity becomes higher. From a practical point of view it is desired to increase the critical current, since this allows the use of superconducting materials at higher currents without dissipation of energy that occurs when vortices flow.

At present it is not possible to experimentally observe the continuous motion of large assemblies of vortices so as to have a statistical description of their motion. The flux penetration in superconductors can happen at a speed as high as 50 km/s [32]. Real-time observation of the evolution of small assemblies (like chains) of vortices has been provided by high-resolution Lorentz microscopy [33, 34] at a time scale of 0.1 s and high-speed magneto-optical imaging [32] at a time scale of 10 ns.

Detailed information of vortex dynamics at a microscopic scale can be obtained by numerical simulations. Using, in general, the Bardeen-Stephen model to describe the flux flow, numerical simulations allow an adjustment of the microscopic parameters like vortex density, pinning strength, and pinning density, which are otherwise difficult to accurately control in experiments.

Vortex dynamics in superconductors with disordered pinning. Neutron scattering [35], voltage-current $V(I)$ measurements [36, 37], decoration experiments [38, 39], and theoretical work [40], as well as numerical simulations [41, 42, 43], have suggested a variety of topological phases occurring in a vortex lattice driven across a disordered pinning landscape. As the driving current is increased from zero, three main dynamical phases are likely to be formed: a *pinned phase* at currents smaller than the critical current (vortices are not moving and the superconductor has zero electrical resistance), an amorphous *plastic flow phase* at intermediate currents, and an ordered *uniform flow phase* at high driving currents. The *plastic flow phase* begins as soon as the driving current overcomes the critical current. In this phase some portions of vortex lattice move while others portions remain pinned. Consequently, the flux flows occurs in the form of percolation-like paths and in general the vortex lattice is not ordered [40, 41, 42]. At high driving currents, the entire lattice is flowing in an ordered phase. In this current range, numerical simulations [43] identified two different uniform phases: when the flux lattice is soft (low vortex-vortex interactions) the vortices flow in independent channels but with an overall smectic order. On the other hand, the flow of a rigid flux lattice is expected to show crystalline order over limited areas. Crystalline phases have both positional and orientational order whereas smectic phases have orientational order but only some degree of positional order. Both these phases have been observed in decoration experiments [38], the smectic phase at low fields, and the crystalline phase at high fields.

Vortex dynamics in superconductors with periodic pinning. Advanced noanofabrication and high-quality film deposition have enabled the production of submicron structures comparable in size with the coherence length and penetration depth of the superconducting materials. A regular pattern of pinning centers (microholes or magnetic dots) induce characteristic commensuration effects between the vortex lattice and the pinning array. These are manifested in temperature and magnetic field dependences of the bulk magnetization, electrical resistance, and critical current [44, 45, 46, 47]. The commensuration effects are observed at "matching fields" $H_n = n\Phi_0/A$ for which the density Φ_0/A of flux lines coincides with the density of pinning centers (called also antidots). Here A is the unit-cell area of the pinning array and n is an integer. Each pinning center can trap either a single quantum vortex (at the first matching field, with $n = 1$) or a multiquantum vortex (at higher matching fields, $n > 1$). Therefore, when the applied field is tuned through to the matching field H_n the total flux through the sample nucleates entirely into microholes; each microhole accommodates exactly n flux quanta. However, there is a maximum number $n_s \approx D/4\xi(T)$ of flux quanta per pinning center that can be trapped in a periodic pinning lattice, where D is the diameter of a microhole (the size of the pinning center) and $\xi(T)$ is the temperature-dependent coherence length. For fields higher than the maximum matching field $H_n(n_s)$ vortices start to form an interstitial Abrikosov lattice between the pinning centers. Commensurability effects at non-integer and submatching fields ($n = 1/2$, $1/3$, $1/4$, etc.) have been observed directly with Lorentz [33] and scanning Hall probe [48, 49] microscopies and indirectly with magnetization and transport measurements [50, 51].

Vortex dynamics in constricted geometries. From the perspective of better controlling vortices in superconducting devices, recent interest has been focused on studying the vortex dynamics in *constricted* geometries. Such spatial localization allows small vortex assemblies to be directly manipulated by either the magnetic field or the driving current.

Recent numerical simulations [52] investigated the distribution of vortex velocities inside of pinning-free channels surrounded by a strong pinning material. The longitudinal motion of vortices along the channels is induced by a current applied perpendicular to the channels. The widths of channels are mesoscopic, which means that only a few vortices can fit across the channels at low magnetic fields. The vortex dynamics in such channels is governed by the vortices' shear interactions with strongly pinned vortices in the adjacent parts. At low driving currents, there is a continuous shearing of vortex rows: the outer rows (near to the channel edges) are immobile whereas the middle ones are moving. However, at higher driven currents, the outer moving vortex rows show an oscillatory shearing dynamic phase which is determined by the interaction with the "bottleneck" potential due to the pinning from the strong-pinning regions adjacent to channels.

The dynamics of the vortex matter confined to mesoscopic channels was investigated experimentally by transport measurements [53, 54]. A double layer structure of a-NbGe (very weak pinning material) and NbN (very strong pinning material) has been used to fabricate an array of narrow weak-pinning channels surrounded by a strong-pinning environment. At low applied magnetic fields (no more than six vortex rows in a channel), commensurability effects between vortex spacing and the channel width appear in the field dependence of the critical current and vortex velocity [55, 53]. Contrary, at higher fields, the vortex flow exhibits a more fluidlike behavior, the shear interaction being reduced. Detailed information on how the vortex dynamic configuration evolves as the field is varied is provided by means of "mode locking technique" [54, 56]. The interference between the washboard frequency of the driven vortices in channels and the frequency of a superimposed rf-drive causes steps or plateaus in the dc-IV curves. These mode-locking voltage steps provides the number of vortex rows in a channel and also shows how the vortex lattice structure in each channel changes with the magnetic field.

Mesoscopic channels with more complex patterns could be used to manipulate vortices in superconducting devices [57, 58, 59]. A controllable rectification of the vortex motion can be realized by means of a nanoscale asymmetric pinning potential. Ac-driven vortex flow along such asymmetric patterned channels would make possible the construction of vortex lenses that funnel vortices in superconducting nanodevices and removed the unwanted trapped flux in superconducting quantum interference devices.

The dynamics of vortex nucleation in such mesoscopic channel is still under investigation. One topic of interest is how the vortex dynamics depends on the width of the channel. Using scanning Hall probe microscopy we investigated magnetic flux nucleation in type-II niobium thin-film strips of mesoscopic width when the applied magnetic field is perpendicular to the strips. One physical quantity that we measured was the maximum magnetic field below which there are no vortices present in the strips. We found the width dependence of this lower critical field for vortex nucleation in narrow strips. The physics of the vortex nucleation at fields above the lower critical field was investigated for three different widths. General and particular features of the vortex nucleation have been revealed for narrow strips in fields above the lower critical field. The experiment is presented in Chapter 5.

Chapter 3

Magnetic Imaging Techniques

Over the years many techniques have been employed to measure the local magnetic field above the surface of superconducting samples. Among the most popular magnetic imaging systems are Bitter decoration [11], magneto-optical imaging [60], scanning Hall probe microscopy [61], scanning superconducting quantum interference device (SQUID) microscopy [62], magnetic force microscopy [63], and Lorentz microscopy [14]. Most of them provide static images of magnetic structures above the samples, but some of them also allow a direct record of the dynamics of magnetic structures. In Fig. 3.1 is shown a diagram of the current state of the art of these techniques, giving their magnetic field and spatial sensitivities. The notations in Fig. 3.1 are as following:

- MO - Magneto-optical imaging
- LM - Lorentz microscopy
- MFM - Magnetic force microscopy
- SHPM - Scanning Hall probe microscopy

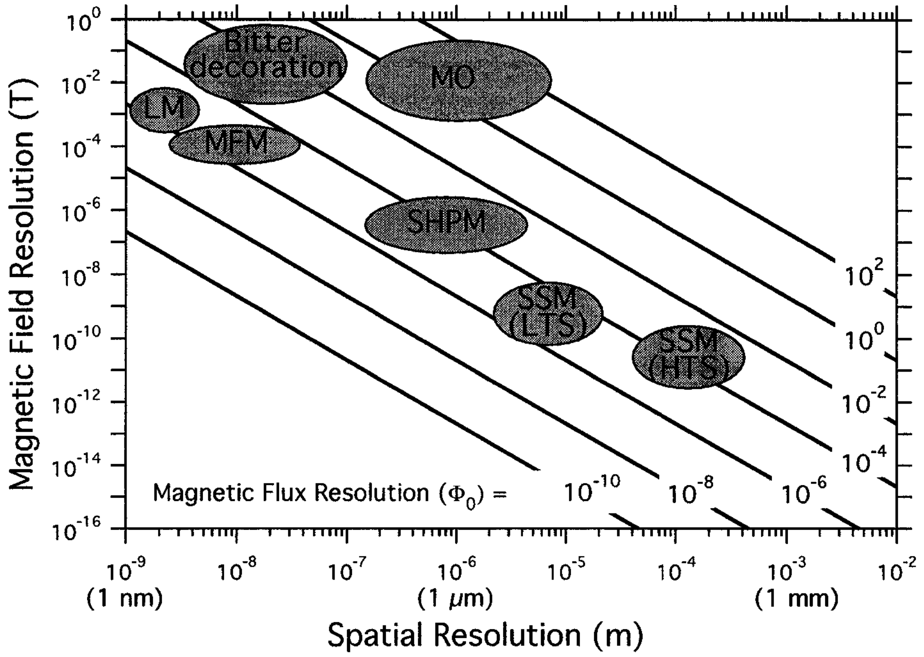

Figure 3.1: Field sensitivity versus spatial sensitivity of different magnetic imaging techniques used to image magnetic flux structures in superconductors.

- SSM (LTS) - Scanning SQUID microscopy with low-temperature superconductors
- SSM (HTS) - Scanning SQUID microscopy with high-temperature superconductors

The plot was adapted (and updated) from Ref. [64, 65]. A recent review of these techniques, with a particular emphasis on imaging vortices in superconductors, can be found in Ref. [65]. Fig. 3.1 shows the trade-offs between field sensitivity and spatial resolution of the different techniques. For example, very high spatial resolution (about 10 nm) can be achieved by Lorentz microscopy but with a modest field resolution (about 1 $\mathrm{mT}/\sqrt{\mathrm{Hz}}$). At the other extreme, scanning SQUID microscopy is the technique with the highest field sensitivity (less than 10^{-10} $\mathrm{T}/\sqrt{\mathrm{Hz}}$) but rather poor spatial resolution (about 5 μm), being limited by current microfabrication capabilities. As can be seen, scanning Hall probe microscopy provides a good compromise between spatial resolution (0.5–1 μm) and field sensitivity (10^{-7}–10^{-6} $\mathrm{T}/\sqrt{\mathrm{Hz}}$).

The diagonal lines in Fig.3.1 indicate the equivalent magnetic flux resolution in units of flux quantum, $\Phi_0 = 2.07 \times 10^{-15}$ $\mathrm{T/m^2}$. The flux sensitivity is given by the product between the field sensitivity and the square of the spatial sensitivity, $B_{\mathrm{min}} \times l^2_{\mathrm{min}}$. We can see that many techniques have a flux sensitivity in the range 10^{-4}–$10^{-6}\Phi_0$. It is possible to see the internal magnetic structure of a vortex with a flux sensitivity better than 10^{-5} Φ_0. In the following I will shortly describe all of these techniques and point out their advantages and disadvantages.

3.1 Bitter Decoration

Bitter [66] pioneered the use of small ferromagnetic particles for decorating the magnetic domains in ferromagnetic materials. A major improvement of the Bitter decoration technique was developed by Essman and Träuble [11] for use on superconducting samples. They have used this technique to investigate the intermediate state structures in thick type-I lead samples [67], flux motion in thick type-I lead foils [68], and Abrikosov mixed state structures in bulk type-II superconductors [69].

In this technique fine ferromagnetic particles are formed by vacuum evaporation and allowed to settled on the surface. The evaporation is done in low pressure helium gas in order to reduce the kinetic energy of atoms and allow them to adhere into 10 nm particles as they move towards the surface.

The resulting configuration of these particles over the surface of the sample is determined by the local magnetic field distribution, the feromagnetic particles being attracted to where the field gradient is larger. After the particles have settled on the surface, magnetic images of the sample surface are obtained by direct observation of the particle distribution either by optical or electron microscopy. The spatial resolution depends, of course, on the size of the ferromagnetic particles (iron or nickel) used for decoration. In their experiments, Träuble and Essmann used small ferromagnetic particles with diameters less than 80 Å, and this provided a spatial resolution of about 100 Å.

This method is restricted to observation of static magnetic flux structure configurations and large magnetic field modulations only, is an invasive technique, uses a sample only once, and provides only a qualitative analysis. Also, the Bitter decoration technique is limited to low fields (less than 10 mT) where vortices are well separated and their field gradients are large enough to assure a good contrast.

3.2 Magneto-Optical Imaging (MOI)

The principle of this technique is based on Faraday rotation of a polarized beam of light through a magnetic-optical material. A magneto-optical layer is evaporated on the top of a superconducting film previously covered with a thin, highly reflecting film. An external applied magnetic field determines a specific magnetic-flux structure through the superconducting film. A polarized beam of light is sent in from the top and passes through the magnetic-optical layer before and after its reflections from the reflecting film. Consequently, the light experiences a Faraday rotation with the rotation angle depending on the local magnetic field strength. The outgoing light is passed through an optical analyzer, so a magneto-optical image of the magnetic field distribution near the surface of the superconducting film can be obtained.

The Faraday effect used for the observation of the magnetic flux structures in superconductors was first demonstrated by Alers [70]. A major development of this technique was done by Kirchner [60]. He used as the magneto-optical material rare-earth compounds (EuO, EuS, or EuSe) which exhibit a very high Faraday rotation, enough to give a good domain contrast in superconducting films.

The spatial resolution of the magneto-optical technique is roughly determined by the thickness of the magneto-optical layer. Though these magneto-optical layers can be made thinner than 100 Å, the magnetic structures at low fields generally suffer from poor contrast, resulting from small Faraday rotations. The high-resolution magneto-optical technique provides a spatial resolution of about 0.5 μm with a magnetic field sensitivity of about 20 G.

Though the spatial resolution of this technique is less than that of the Bitter decoration, a continuous observation of the dynamics of the magnetic flux structures is possible with the magneto-optical method. Moreover, the same sample can be used to image many different configurations (not only one as in Bitter decoration) and it is also possible to make a quantitative measurement of the magnetic field profile above the sample, not just a qualitative analysis.

The magneto-optical imaging was used by Chimenti and Huebener [26] to investigate the dynamics of the current-induced resistive state. Using stroboscopic illumination in combination with magneto-optical flux detection they studied flux motion in type-I superconducting films with a high time resolution better than tenth of a microsecond. More recently, Leiderer *et al.* [32] has been able to achieve 10 ns temporal resolution in recording the time evolution of flux instabilities induced by a laser pulse in a YBCO film.

Magneto-optical imaging is the only technique available to study vortex dynamics on sufficiently short time scale and provide information about individual motion of vortices. Though usual magneto-optical images show the distribution of "average" flux density, it is now possible to observe even individual vortices at low flux densities [18].

3.3 Scanning Superconducting Quantum Interference Device (SQUID) Microscopy (SSM)

The most field-sensitive microscopic magnetic imaging technique is scanning SQUID microscopy (SSM), currently developed with low-temperature superconducting SQUIDs [62]. In this instrument a superconducting pickup loop is coupled magnetically to a dc SQUID which is scanned in two directions over the surface of the sample to map out the magnetic field modulations above that surface. A dc SQUID is a very sensitive detector of magnetic flux consisting of a loop with two weak links (two Josephson junctions). Any flux changes in the loop produces oscillatory variations in the voltage across the two weak links, each oscillation being associated with a flux quantum. The first developed SSM [71] had a spatial resolution of 20 μm (determined by the size of the SQUID's loop) and a flux sensitivity of $10^{-5}\ \Phi_0/\sqrt{\mathrm{Hz}}$.

In the original design [71], the dc SQUID sensor and flux transformer are located inside a vacuum can, being positioned and scanned by a room temperature translation stage driven by a stepping motor. The room-temperature-controlled positioning was used in order to assure a large scan area. Some other scanning SQUID microscopes also include an additional piezoelectric scanner [72]. The SQUID sensor is either mounted on a hinge [62] or on a cantilever [72] and runs in direct contact with the sample to compensate for height variations while scanning. Kirtley *et al.* [72] fabricated a single-chip miniature SQUID magnetometer with the pick-up loop and leads forming an integral part. They claim that their direct coupled single-chip design is about ten times more sensitive than the discrete design where the pick-up loop is inductively coupled to the SQUID [62].

Typically, the magnetic flux sensors used in SSM are all-Nb square-washer dc SQUIDs. The Josephson junctions are fabricated by a standard Nb/AlO/Nb trilayer process with junction areas of 1–2 μm^2.

Compared to all the other magnetic imaging techniques, SQUID detection has the best magnetic field sensitivity (10^{-7}–10^{-6} $\text{T}/\sqrt{\text{Hz}}$). The spatial resolution is rather poor (not less than 5 μm) being limited by current microfabrication capabilities. However, the flux sensitivity of the SSM is extremely high, allowing, for example, accurate measurements such as the first direct observation of 1/2 integer flux quanta in high-Tc superconducting rings [73]. A current drawback of SSM is that SQUID sensors are fabricated from low-temperature superconductors (niobium is the most common choice). This limits the scanning temperature below the critical temperature of the SQUID sensor (9.2 K for niobium). The solution would be to use SQUIDs fabricated from high-temperature superconductors. Currently, these have a better field resolution but a worser spatial resolution comparative to those fabricated from low-temperature superconductors (see Fig. 3.1). This is because it is still difficult to pattern high-temperature superconducting films at the submicron scale.

3.4 Scanning Hall Probe Microscopy (SHPM)

Scanning Hall probe microscopy provides a direct and versatile method of measuring the local magnetic field above the sample's surface. It is a noninvasive way of imaging over the same area different magnetic field configurations determined by the change of experimental parameters like the external magnetic field, temperature, and current through the sample.

A scanned Hall probe patterned on a bismuth film was first used by Goren and Tinkham [6] to investigate flux configurations of the intermediate state of type-I superconducting films in perpendicular applied magnetic field. A field sensitivity of 0.1 G, a spatial resolution of about 4 μm, and a distance of 5 μm between the Hall probe and the sample limited the attractiveness of the method.

In 1992, Chang *et al.* [61] developed the first reliable scanning Hall probe microscope. Their Hall probe had a field sensitivity of 0.1 G and a spatial resolution of 0.35 μm, and could map out the magnetic field at a height of only 0.2 μm above the sample. These characteristics were achieved by patterning the Hall probe onto the two-dimensional electron gas (2DEG) of a GaAs/AlGaAs heterostructure, and by using a scanning tunneling microscopy (STM) positioning technique. Initially, the GaAs/AlGaAs material was chosen to have a low mobility of 50 000 cm^2/Vs, people being concerned about the quenching of the Hall effect associated with ballistic transport in a junction. Subsequently, it was proved that high mobility 2DEG ($\sim$ 300 000 cm^2/Vs) improves the quality of Hall probes at low temperatures. The electron density in the 2DEG is about $2 \times 10^{11}\mathrm{cm}^{-2}$.

A Hall probe consists of a conducting cross made into a 2DEG to measure the magnitude of the magnetic field by using the Hall effect. Thus, charge carriers moving along the "current arm" of the Hall cross are deflected by an applied magnetic field, creating a voltage across the "voltage arm" of the Hall cross. This voltage is directly proportional to the average magnetic field over the active region. The active area is defined by the intersection of the "current" and "voltage arms".

Such a microscope typically incorporates a Hall probe mounted on the piezoelectric scanner of a fabricated low-temperature STM. The active Hall sensor is patterned in about 10 μm away from the chip corner. To assure scanning in close proximity to the sample's surface, the Hall probe is tilted by a few degrees with respect to the sample's surface. The Hall probe is brought to about 0.1–0.5 μm above the sample's surface, and the scan is done at this height. This distance is established as in STM by detecting a tunneling current between the sample and the gold layer that covers the probe's corner. A typical scanning range of a STM piezotube used in SHPM is about 10 μm at 4.2 K.

Some of the highest-quality Hall probes have been reported by Bending's group at the University of Bath (UK) with a magnetic sensitivity of 0.3 $\mathrm{mG}/\sqrt{\mathrm{Hz}}$ and a spatial resoultion of about 0.85 μm at 77 K [74]. Currently, several groups are trying to reduce the size of the sensor active area, and in this way to increase the spatial resolution, by using electron beam lithography to pattern the Hall probes on

GaAs/AlGaAs 2DEG heterostructures. In this way it may be possible to reduce the size of the active region to about 200 nm.

Scanning Hall probe microscopy forms an integral tool in our experimental investigations of magnetic field profile above superconducting films. A detailed description of our scanning Hall probe microscope is provided in Chapter 4.

3.5 Magnetic Force Microscopy (MFM)

Magnetic force microscopy is based on measuring the magnetic interaction between a force probe —a magnetized tip— and the sample. As the tip is scanned over the sample's surface it feels a force due to the local magnetic field gradient. The small deflection due to this force is measured and added into a magnetic raster image.

The field gradient is mapped out as a variation of the force on the tip, this being moved at a constant height over the investigated sample. The technique was proposed by Martin and Wickramasinghe [75] who used an iron tapered tip with a tip radius of 1000 Å to image a thin-film magnetic recording head.

Ideally, the scanning tip should be a microscopic single-domain ferromagnetic particle with a high coercive force in order to provide a high magnetic field sensitivity. Usually, the tips are made by depositing thin magnetic films over sharp atomic force microscope tips. Therefore, the magnetic structure of the tip is unknown and it can be difficult to interpret the obtained MFM image. Further, the image can change from scan to scan as a result of interactions which occur between the tip and the scanned magnetic structures.

The best MFM images of vortices in superconductors have been reported by Güntherodt's group at the University of Basel [76, 77, 15]. Scanning at 20 nm above the surface this microscope is capable of detecting magnetic forces as small as 0.4 pN. Though the spatial resolution is quite good (about 50 nm), the magnetic field resolution is rather poor (about 10 $\mathrm{G}/\sqrt{\mathrm{Hz}}$).

3.6 Lorentz Microscopy (LM)

Lorentz microscopy was first used to image magnetic domain structures in feromagnetic thin films [78]. In this technique, a beam of electrons is passed through a magnetic film and deflected by Lorentz force due to the local magnetization, the deflecting angle depending by the magnetization strength.

In superconductors, with an in-focus electron beam it would not be possible to see any magnetic image of flux lines, these being perfect phase objects (the Aharonov-Bohm effect due to the flux vortex core). However, the phase shift produced by the flux vortex filaments in a tilted sample with respect to both the incident electron beam and the applied field is visible in a defocused plane. Vortices appear as spots having one side light and one side dark, with the separation line parallel to the projection of the vortex on the image plane.

Using a 300kV field-emission transmission electron microscope, Harada *et* *al.* [14] have been able to observe the dynamics of vortices in Nb thin films. Compared to the other imaging techniques, Lorentz microscopy can be used to directly observe in real time both the dynamics of individual vortices and their interaction with pinning sites. By analyzing successive frames of recorded video tape, with a time resolution of 1/30 s, it was possible to trace out the intricate motion trajectory of vortices in a Nb thin film [79]. Only MO imaging has a better temporal resolution, though Lorentz microscopy has not been fully developed in this direction.

Although the spatial resolution is very good (about 10 nm), the field resolution of Lorentz microscopy is rather poor (10 $\mathrm{G}/\sqrt{\mathrm{Hz}}$), and it is difficult to extract quantitative information from the magnetic images. A further drawback of the Lorentz technique is the requirement of using only very thin samples (few tens of nanometers) in order to achieve adequate electron transmission. Consequently, the sample dimensions can considerably influence the observed flux configurations.

Chapter 4

Scanning Hall Probe Microscopy

Among the different magnetic imaging techniques, scanning Hall probe microscopy (SHPM) is one which most successfully fulfills the tradeoff between spatial resolution and magnetic field sensitivity. In this chapter I will describe the SHPM developed in our group at Colorado State University. I used this SHPM in all the experiments that I carried out during my Ph.D. program. As with any magnetic imaging scanning instrument, this SHPM comprises of a magnetic sensor (the Hall probe) which is moved above a sample (a superconducting film) while recording the sensor's output. The positioning and raster scanning of the Hall probe above the sample is provided by a piezo-scanning unit. The Hall signal, proportional to the magnetic field normal to the sample, is recorded during the scanning using lock-in detection. In this way the magnetic field profile above the sample can be mapped out. A schematic drawing of the scanning part of our microscope is presented in Fig. 4.1.

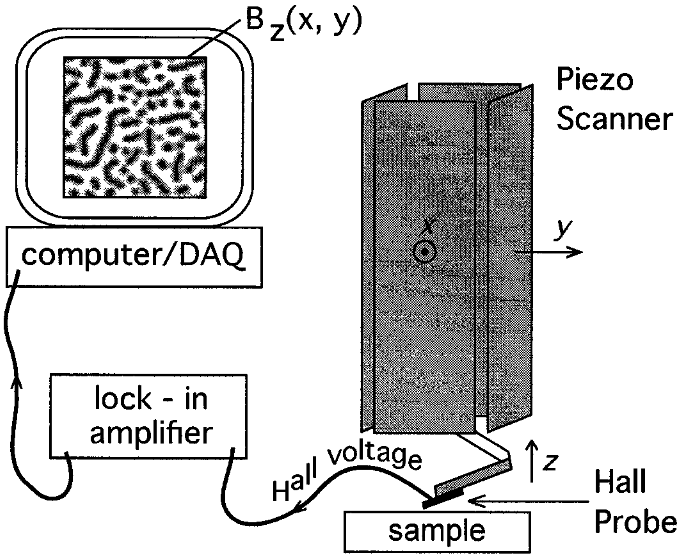

Figure 4.1: Schematic drawing of the scanning Hall probe microscope.

4.1 Cryostat and Microscope Design

4.1.1 The helium cryostat.

Utilizing liquid helium (LHe) as coolant agent, our custom manufactured Janis cryostat operates in a temperature range from less than 2 K to 300 K with precise temperature control capability (± 1 mK). As shown in Fig. 4.2, the system consists of a vacuum can at the bottom of cryostat, a stainless steel wireway and pump out tubes, electrical feedthrough ports, and a custom superconducting magnet. This system is then inserted into a liquid helium dewar. Inside the vacuum can there is a sample holder with provisions for thermometry, temperature control, electrical connections, and a x-y mechanical and piezoelectric positioning mechanism.

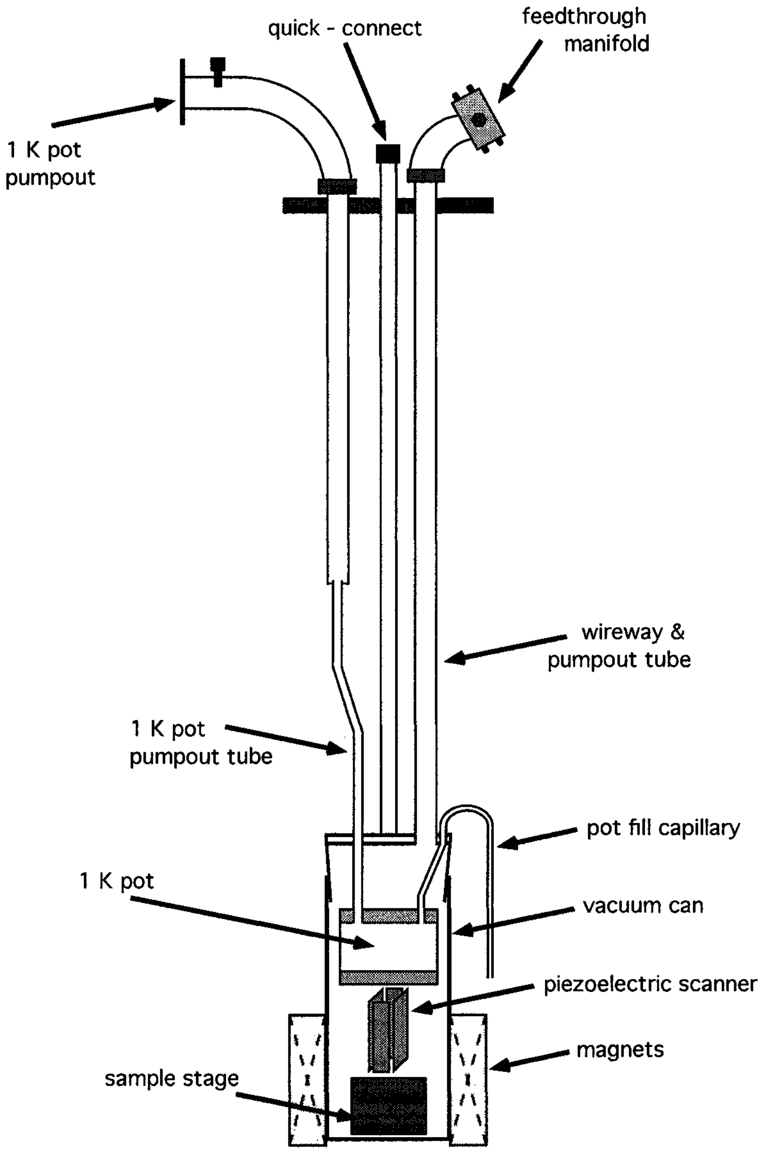

Figure 4.2: Simplified drawing of the Janis cryostat.

Cryostat preparation. After the sample and Hall probe are mounted there are several important steps to perform before the dewar can be filled with LHe. First, we need to seal and pump out the vacuum can. This is necessary to get good thermal isolation inside the can. A vacuum leak check is done at this point. Prior to filling with LHe the dewar bath is precooled with liquid nitrogen (LN). This takes some 8 to 10 hours, so we leave the dewar overnight to attain the temperature of LN (74 K). After it is cooled to LN temperature, the liquid nitrogen is completely removed from cryostat bath by blowing it out with helium gas. To do this, a stainless steel tube is inserted to the bottom of the cryostat bath and then, by over-pressurizing the bath with helium gas, the liquid nitrogen is forced up the tube and out of the bath. Helium gas is used in order to prevent any nitrogen freezing. After a second leak check on the vacuum can, we are ready for the LHe transfer. Liquid helium has the smallest latent heat of vaporization among all cryogenic liquids. For this reason the sensible heat of the vapor should be used in precooling rather than just the latent heat of the vaporizing liquid. To do this, the transfer is done very slowly until the bottom vacuum can is well covered with LHe. In general we transfer about 15 liters of LHe. In about 30 minutes the cryostat vacuum can is cooled down to 4.2 K and ready for operation.

Working at low temperatures. Temperatures below 4.2 K are achieved by pumping on a LHe pot. The pot is a small vessel of several cm^3 located inside the vacuum can and connected through a fill capillary to the cryostat bath (see Fig. 4.3).

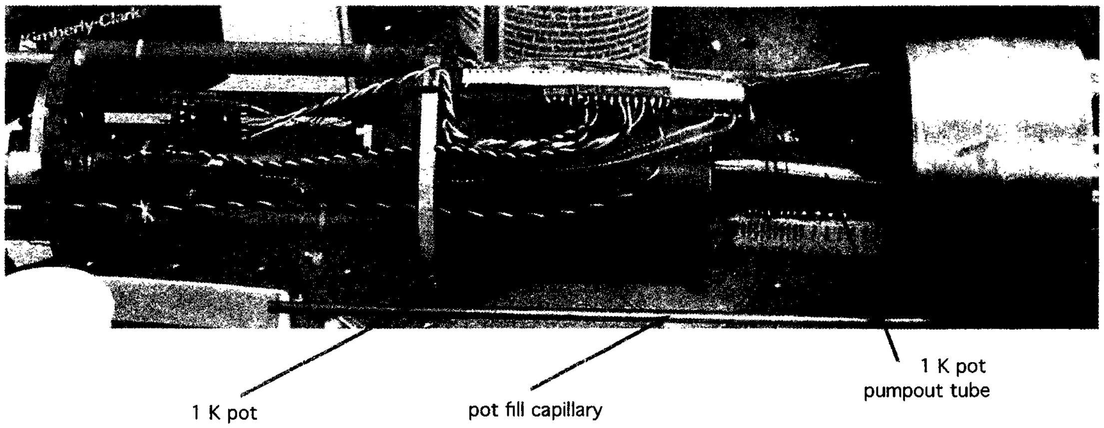

Figure 4.3: The 1 K pot of Janis cryostat.

Before and during the LN precooling process, the pot and fill capillary are purged with pure helium gas in order to prevent liquid nitrogen from entering the fill capillary and freezing. Once the cryostat is filled with LHe, the liquid from the cryostat at 1 atm is isenthalpically expanded through the capillary and arrives at a lower temperature into the pot. The pot will continue to fill until the cooling power due to evaporation of liquid is balanced out by the external heat flowing to the pot. With our cryostat the lowest achieved temperature is around 1.5 K. The reason why we can not go below 1.5 K is due to the existence of different heat leaks. For example, we use a long rod to mechanically adjust from outside the x-position of the sample stage. Clearly, a significant heat is dissipated inside the vacuum can through this rod.

Piezoelectric Scanner. The main part of our microscope is, of course, the scanning unit located inside the vacuum can. To accomplish a large scanning range in both the x and y-directions, our scanning unit was built after a design proposed

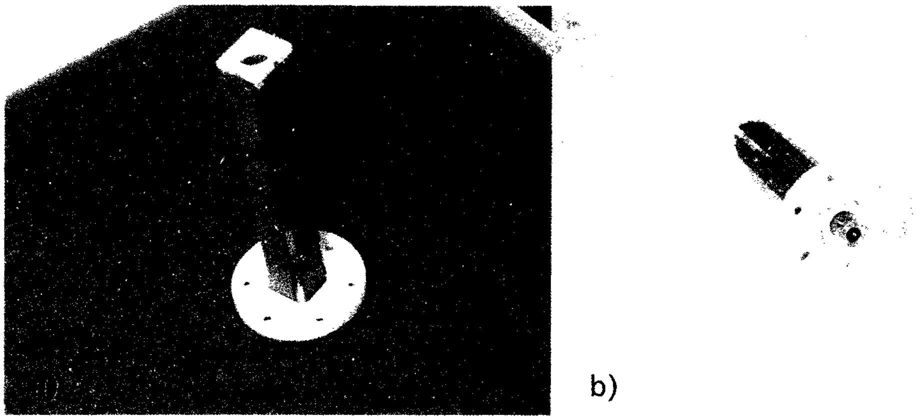

Figure 4.4: Top (a) and bottom (b) view of the piezo-scanning unit.

by Siegel *et al.* [80]. It consists of four piezo benders connected together by three Macor ceramic pieces: a base, a top stage, and a scanning head stage (see Fig. 4.4). Macor was used because it has a thermal expansion similar to that of piezoelectric elements. The base is attached to the main copper frame of the microscope. Each of the four piezoelectric elements is a ceramic piezoelectric bimorph. This means that each piezo is made of a double plate ceramic element. The two plates are polarized in opposite directions. Under an applied voltage one layer is in tension while the other is in compression so they will be forced to bend and, in this way, their piezoelectric action will be amplified. The bias voltages applied on the piezo benders are supplied by a high-voltage amplifier which can provide up to ±150 V. The voltage difference between the electrodes can therefore swing between +300 V and −300 V. The corresponding electric field is below the depolarization field of piezoelements. The measured scanning range provided by these bias voltages was about 2 mm at room temperature and 275 μm at 4.2 K.

To realize the motion in the vertical z-direction a short piezoelectric bender is attached to the scanner head (see Fig. 4.5a). This is because, besides scanning in a x-y plane parallel to the sample's surface, we also need motion along the vertical axis for a fine approach to the sample's surface. The short bender is mounted between two Macor pieces. On the lower Macor piece of this z-scanning unit is attached the Hall sensor which is tilted by about 3° with respect to the scanning plane. The whole deflection range in the z-direction is about 40 μm. At room temperature, we have made a calibration of the z-piezo in two ways, directly under the microscope, and by measuring the capacitance between two copper plates mounted on the two macor pieces of z-piezo unit. We find in both cases that the z-piezo displacement is about 0.42 μm/V.

Capacitive sensor position. In general, piezoelectric elements show nonlinearity and hysteresis and this makes it difficult to have a direct relationship between the bias voltage and the resulting displacement. Consequently, a position sensor is desirable in order to map the position of the Hall sensor during the scan. With such a position map it is possible to make accurate correlations between different features in recorded magnetic image and their actual surface topographical location. A versatile capacitive position sensor, used in our microscope, was developed by Field and Barentine [81] (see Fig. 4.5b). The position sensor consists of a flat base electrode divided into four quadrants, with the gaps between quadrants defining the x and

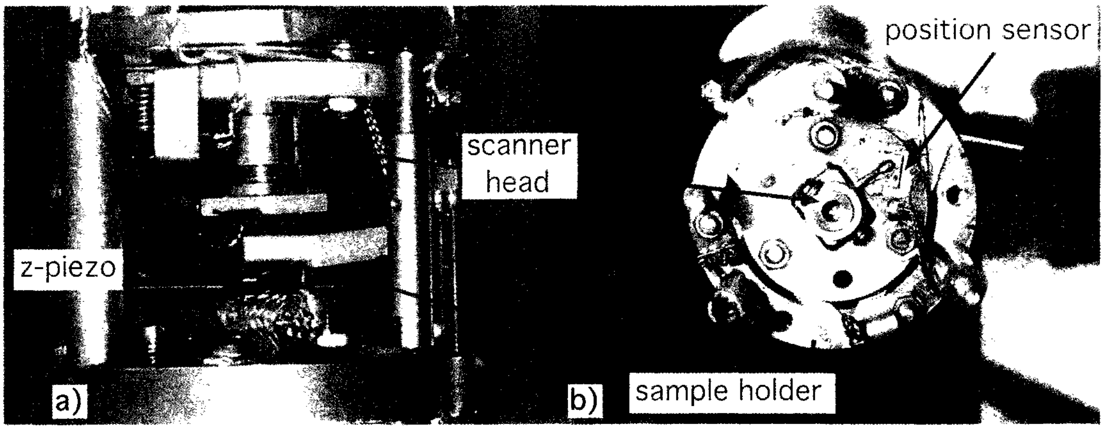

Figure 4.5: The head of the piezo-scanning unit.

y-directions. A second flat electrode sits at a small distance above the base electrode. This second electrode is rigidly attached to the piezo scanning head and, consequently, executes the same scanning motion as the scanning head. The four base electrodes are excited simultaneously with phases which increase by 90° in a counterclockwise circulation around the base (i.e. $-45°, 45°, 135°$, and $225°$). The current capacitively injected into the moving electrode will have an in-phase and an out-of-phase part; the in-phase component is directly proportional to x-position, with no y-dependence, and the out-of-phase component is directly proportional to y-position, without any x-dependence. Thus, using a lock-in amplifier, we can accurately measure the two current components and map out the topography in a scanning picture.

Sample holder. The sample is attached on a stage unit which has several functions: to hold the sample; to roughly adjust the scanning plane by mechanically tilting the sample stage with respect to this plane; and to capacitively detect the

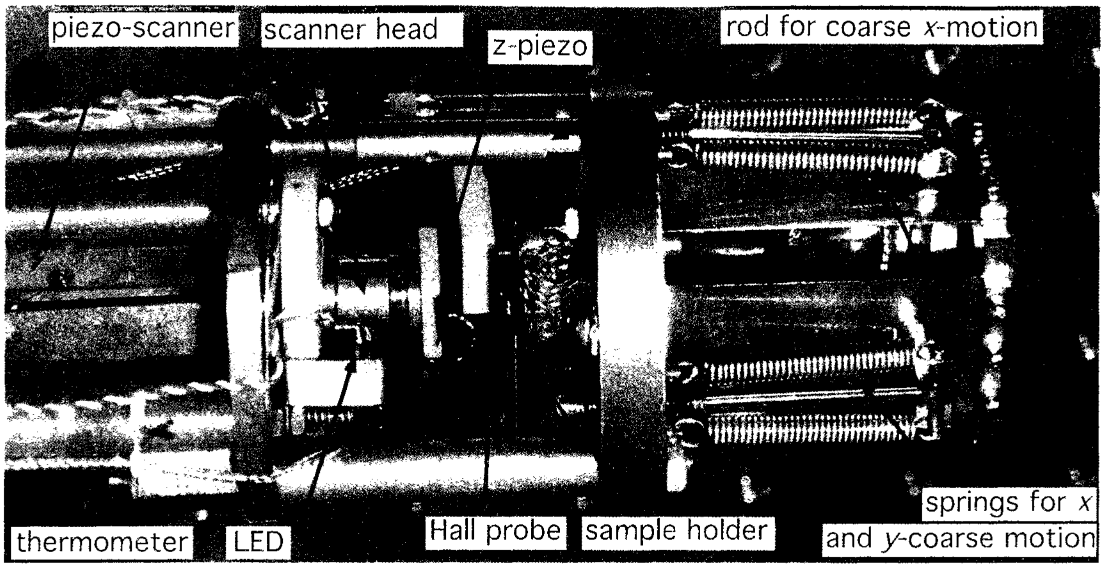

Figure 4.6: The top part of our scanning Hall probe microscope.

contact between the Hall sensor and sample's surface. In most scanning near-field microscopies, the tunneling current between the sensor and the sample is used to detect when the scanning head becomes close to the sample's surface. However, we use a simpler method that is still quite accurate, by detecting mechanically the direct contact between Hall sensor and sample's surface. We do this by mounting the sample on a bendable cantilever, which is a thin brass plate fixed by two screws on the stage unit (see Fig. 4.5a). The small deviations of the cantilever plate are detected by the change in the capacitance of a capacitor which has one plate glued on the cantilever plate and the other on the stage unit. Thus, the change in capacitance will tell us when the Hall sensor comes in direct contact with the sample. We detect this impact by measuring 0.01 pF changes of the capacitance which correspond to a

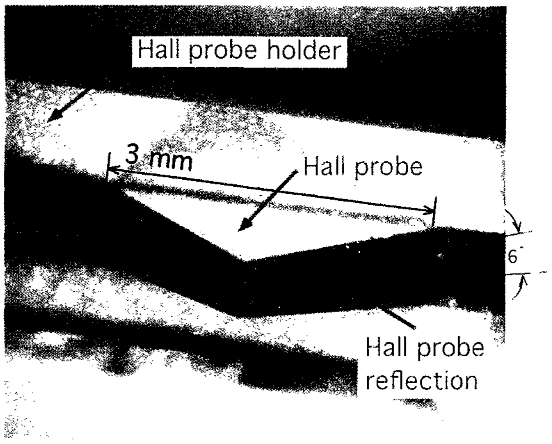

Figure 4.7: Positioning the Hall probe above the sample.

gentle press-down of the sample by the Hall probe over about 1 nm.

The stage unit also incorporates mechanical means for coarse tilt adjustments of the sample. Using this adjustment we first do a room-temperature mechanical compensation, in order to make the scanning plane and the surface sample's plane parallel.

We also have the possibility of exploring, at cryogenic temperatures, different regions of the sample over about 2 mm range in x-direction. A long rod coming from the cryostat top is screwed into the base stage and allows the mechanical coarse motion of the stage in the x-direction at any temperature. In this way, we can map a large area on x-directions, each time covering an area of 150 μm × 150 μm. A detailed picture of the top part of our microscope is presented in Fig. 4.6.

Scanning operation. At low temperature, the Hall probe is first approached mechanically from outside of the microscope using a long rod which pushes the whole scanning unit towards the sample. Actually, this operation entails the biggest risks; the approach is quite nonuniform and hard to do in small steps. Usually we move off from the area which is intended to be scanned in order to reduce as much as possible any surface damage. However, we also can make, over short distances, a much safer electrical approach using the z-piezo unit. Therefore, it is possible to make, tediously but safely, a mechanical approach in very tiny steps, each coarse step being previously explored by a z-piezo motion. In any case, after the sample's surface is touched, the Hall probe is retracted about 1 μm above the surface and the scanning is initiated. Fig. 4.7 shows the Hall probe positioned above the sample at room temperature. The Hall probe is tilted about 3° with respect to the scanning plane; in Fig. 4.7 this angle is half of the angle between the Hall probe and its reflection on the sample's surface.

Before scanning at low temperature it is necessary to make the scanning plane accurately parallel to plane of the sample's surface. First, at room temperature we make a coarse adjustment between these planes by using a mechanical compensation. For fine adjustment at low temperatures, we can add some of the x or y scanning voltage into the z piezo voltage. Thus as the scanner moves in, say, x, it also moves slightly in z, effectively changing the plane of the scan. In this way we can accurately adjust the plane of scanner, but the tradeoff is a possible reduction of the scanning length along the x or y directions. Thus it is preferable to start with as good as possible of a mechanical compensation at room temperature, in order to add only small amount of offset bias voltages at low temperature.

The number of steps that make a sweep in the x and y directions can be set to either 128 (low resolution) or 256 (high resolution), each step being covered in 5 ms. At each step the Hall probe will report a measured voltage proportional to the magnetic field strength at that point. In a LabView program, the response of the Hall probe is continuously plotted, so after each scan we get the profile of the normal component of the magnetic field above the sample.

4.2 Hall Probe Technology

4.2.1 The Hall effect in heterostructure Hall probes

The Hall effect in a conductor (metal or semiconductor) is well known from a textbook: when charge carriers move along a direction perpendicular to an applied magnetic field, they are deflected on a direction normal to both these directions by the Lorentz force. Consequently, the charge carriers accumulate on the sample' edges and a voltage (called the Hall voltage) can be measured across the two sides of the sample (Fig. 4.8). The Hall voltage is proportional to the current I and the magnetic field B:

$$V_{\mathrm{H}} = IB/qnd = R_{\mathrm{H}} IB/d, \tag{4.1}$$

where n is carrier charge density, d is the sample thickness, and q is equal to either $-e$ (for electrons) or e (for holes); $e = 4.8 \times 10^{-10}$ esu is the elementary charge. The Hall coefficient is defined as $R_{\mathrm{H}} = 1/qn$. By measuring the Hall voltage V_{H} and knowing

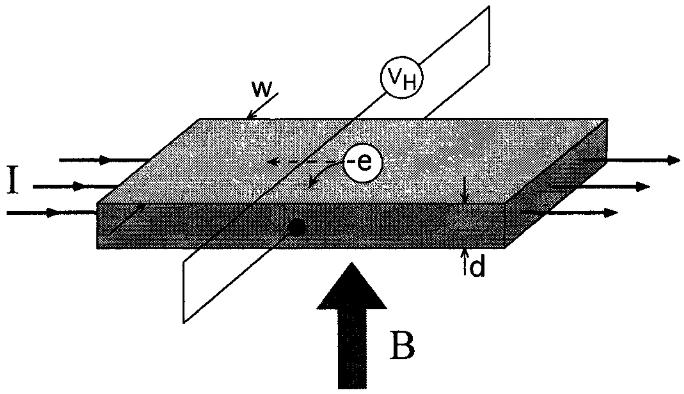

Figure 4.8: Hall effect in a conducting strip.

the current I, the thickness d, and the Hall coefficient R_{H}, one can determine the applied magnetic field. Thus, a conducting strip with Hall geometry can be used to map out the magnetic field above of a sample by measuring the Hall voltage while the sample's surface is explored in a scanning operation.

The first experiments using Hall sensors to image the flux profile above the surface of superconductors were made some 30 years ago. Hall bars fabricated into thin evaporated films of semimetal bismuth [6] had a spatial resolution as high as 4 μm with a field resolution of 0.1 G. A tremendous improvement in the Hall probe's performance (field sensitivity of 0.3 mG/$\sqrt{\mathrm{Hz}}$ [74]) was accomplished after the invention of the modulation doped semiconductor heterostructure [82]. This breakthrough was made possible by the very large mobility (higher than 1 $\times 10^6$ cm^2/Vs) of the 2D electron gas trapped at the interface between two layers of a doped heterostructure such as GaAs/AlGaAs heterostructures, coupled with an extremely low 2D electron density of a few times 10^4 cm^{-2}. In contrast, the best reported epitaxially grown bismuth

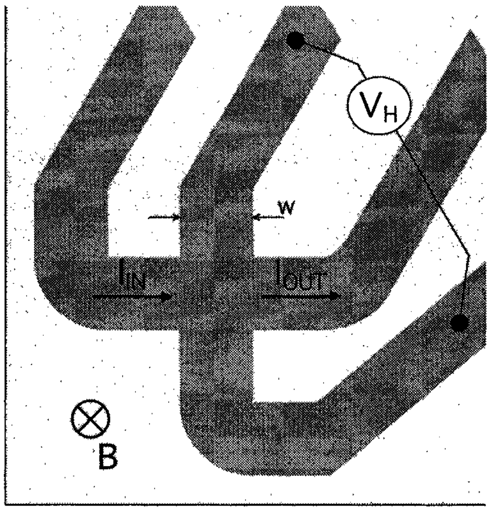

Figure 4.9: Hall cross design adjusted over a wafer corner.

films (45 μm thick) have an electron mobility of only 1 $\times 10^5$ cm^2/Vs [83]. Further, although bismuth has a very low electron density for a metal ($\sim$ 9 $\times$ 10^{17} cm^{-3}), a thin film of thickness 100 nm will still have a 2D density of around 10^{13} cm^{-2}, much higher than for a doped heterostructure. As we will see, high quality Hall probes require high electron mobility and low electron density, but a trade-off between these parameters is necessary to assure a good electrical conductivity.

To understand what parameters affect a material's suitability for Hall probes, we consider in Fig. 4.9 the planar Hall circuit (gray traces) used for local measurement of the magnetic field. Here, the electrons moving along the "current arm" of the Hall cross in an applied perpendicular magnetic field are deflected from their straight path by the Lorentz force; a bias voltage, proportional to the current and to the magnetic field, is created across the "voltage arm" of the Hall cross. In equilibrium the Lorentz force is compensated by the electric force due to the developed Hall field E_{H}:

$$ev_{\mathrm{d}}B = eE_{\mathrm{H}}, \tag{4.2}$$

where v_{d} is the drift velocity of electrons. Thus,

$$E_{\mathrm{H}} = v_d B = \frac{J_{2\mathrm{D}}}{n_{2\mathrm{D}}e}B = R_{\mathrm{H}}J_{2\mathrm{D}}B, \tag{4.3}$$

where $J_{2\mathrm{D}} = n_{2\mathrm{D}}ev_d$ is the 2D current density. Thus, the Hall field E_{H} is proportional to both the current density $J_{2\mathrm{D}}$ and the field B, with the constant of proportionality

$$R_{\mathrm{H}} = \frac{1}{n_{2\mathrm{D}}e}, \tag{4.4}$$

called the *Hall coefficient.* Clearly, for the largest Hall voltage one desires a large Hall coefficient; we note that this implies a *low* two-dimensional electron density $n_{2\mathrm{D}}$.

An important parameter measuring the quality of the material used to fabricate Hall probes is the Hall sensitivity S, defined as the ratio between the measured Hall voltage V_{H} and the applied magnetic field B:

$$S = R_{\mathrm{H}}I = V_{\mathrm{H}}/B. \tag{4.5}$$

The Hall voltage, $V_{\mathrm{H}} = wE_{\mathrm{H}}$, is measured between the voltage leads, and $I = wJ_{2\mathrm{D}}$ is the current flowing along the current leads of the Hall cross. Again, a low 2D electron concentration is desired in order to get higher Hall sensitivity. We note that the Hall sensitivity S doesn't depend on w (the arm width of the Hall cross).

A second important parameter that characterizes a 2D electron system is the electron mobility μ. The electron mobility is the ratio between the drift velocity of the electrons and the magnitude of the driving electric field, $\mu = v_\mathrm{d}/E$. Although μ doesn't affect the Hall coefficient R_H or the sensitivity S, it does affect the sheet resistance of the circuit:

$$R(\Omega/\Box) = \frac{R_\mathrm{H}}{\mu} = \frac{1}{n_\mathrm{2D}e\mu}. \tag{4.6}$$

The above relation shows us that for a given electron concentration (which establishes the Hall sensitivity), the sheet resistance will be reduced by increasing the electron mobility. With a low sheet resistance, the noise (mainly the Johnson noise) will be reduced, the frequency response will be improved, and the offset voltage (due to slight misalignments of opposite arms in the Hall cross) will be reduced. However, another way to lower the sheet resistance is to increase the electron concentration, which implies a reduction of Hall sensitivity. So, there is a trade-off in choosing the wafer's parameters.

4.2.2 Selecting the wafers for Hall probe fabrication

In the previous section we concluded that in Hall probe fabrication we have to look for materials with low electron concentration and high electron mobility. Today, high-resolution Hall probes are patterned onto a GaAs/AlGaAs (or GaSb/InAs/GaSb) two-dimensional electron gas (2-DEG) heterostructure. The 2-DEG trapped into a doped heterostructure is the most important low-dimensional system for electronic transport. The achievement of high mobility (about 0.1–2 $\times 10^6$ cm^2/Vs) in 2-DEGs is possible because nearly perfect crystalline quality III-V heterostructures can be grown in which the carriers are separated from the impurities that provide them. These high mobility GaAs/AlGaAs 2-DEG heterostructures are used commercially in field-effect transistors like modulation-doped field-effect transistors (MODFET) and high electron mobility transistors (HEMT).

In classical electronic devices the carriers are produced by doping the region where they are needed. The performance of these devices is affected by the scattering of the carriers off their donors through the Coulomb interaction (ionized-impurity scattering). A tremendous improvement was made by a *modulation doping* in which the doping is grown in one region but the carriers subsequently migrate to another place. At a heterostructure made between n-AlGaAs and undoped GaAs the electrons are released from the doped layer and cross into the GaAs layer. Here they lose energy (because of the difference in the band energies of the two layers) and become trapped into the GaAs layer, making an accumulation layer of electrons at the heterostructure's interface. This is because the electrons cannot climb back over the potential barrier and the electric field squeezes them against the interface. Usually only the lowest energy level for motion perpendicular to the interface is occupied. Thus, almost all the electrons are in the same state for motion in z-direction (perpendicular on the interface) but remain free to move in the x and y-directions. This is the *two-dimensional electron gas* (2-DEG). A schematic structure of a such GaAs/AlGaAs 2-DEG heterostructure, similar to our wafers' structure, is shown in Fig. 4.10; the density of its 2-DEG was calculated by using a modeling program for self-consistent

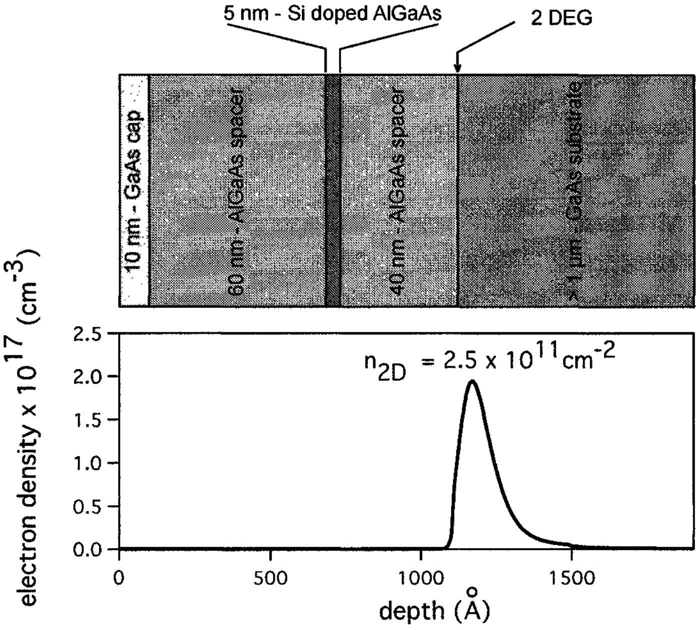

Figure 4.10: GaAs/AlGaAs 2-DEG heterostructure.

solving of 1-D Poisson's equation in a semiconductor structure [84].

Thus, modulation doping achieves two important things:

- The separation of electrons from their donors is realized. In this way the scattering on ionized impurities is reduced;
- The electrons are confined into a two-dimensional system, allowing us to design devices in the planar geometry.

A further reduction of scattering is obtained by increasing the separation between electrons and their donors, leaving a spacer layer of undoped AlGaAs between the doped n-AlGaAs and GaAs. This is done in devices where it is desired to achieve a higher electron mobility, at the cost of a lower density of electrons in the 2-DEG.

layer	material	thickness	doping
cap	GaAs	10 nm	
spacer	AlGaAs	60 nm	
2-DEG channel	AlGaAs	40 nm	8.0×10^{18} cm^{-3}
spacer	AlGaAs	40 nm	
spacer	GaAS	80 nm	
substrate	GaAs	> 300 μm	

Table 4.1: Structure of Gossard group GaAs wafer. The top surface of the wafer is at the top of the table.

Consequently, the criterion in choosing the wafer for Hall probe fabrication is to have high electron mobility and low density electron density in the 2-DEG in such a way to maximize the conductivity $\sigma = ne\mu$. We need high electron mobility in order to assure a high electron conductivity, and low electron density in order to provide a large Hall coefficient $1/ne$. Also, working at low temperatures is in our favor because the electron mobilities are limited there only by scattering from impurities, defects, and interfaces rather than phonons.

For the experiments discussed in this thesis we used wafers provided by two different research groups that specialize in growing high-quality heterostructure wafers, Professor Arthur Gossard's group from University of California-Santa Barbara and Professor Hadas Shtrikman's group from Weizmann Institute of Science (Rehovat, Israeli). The structure of a wafer provided by Professor Arthur Gossard's group is presented in Table 4.1. The electron mobility is $\approx 3.9 \times 10^5$ cm^2/ Vs and the electron density $\approx 2.4 \times 10^{11}$ cm^2. We fabricated very good Hall probes with this wafer: at 4.2 K the magnetic field sensitivity is $S = 9.24$ μV/G for $I_{\mathrm{Hall}} = 50$ μA, with a voltage

wafer	n_{2D} (cm^{-2}) $\times 10^{11}$	μ (cm^2/Vs) $\times 10^4$	R_H (Ω/mT)	S (μV/G) ($I_H = 50\ \mu$A)	σ^{-1} ($\Omega/\Box$)	e_B (mG/$\sqrt{\text{Hz}}$)	SNR ($B =$ 1G)
1a	2.4	39	2.60	theoretical: 13 measured: 9.30	66	6.25	28.2
1b	2.4	39	2.60	theoretical: 13 measured: 9.24	66	4.46	40.2
2a	12	7	0.52	theoretical: 2.6 measured: 2.80	75	4.60	37.8
2b	12	7	0.52	theoretical: 13 measured: 2.80	75	5.35	33.3

Table 4.2: Hall probes parameters at low temperatures.

noise $e_n = 13.2$ nV/$\sqrt{\text{Hz}}$, and a magnetic noise $e_B = e_n/S = 4.46$ mG/$\sqrt{\text{Hz}}$.

Parameters of Hall probes. In Table 4.2 there are presented parameters of Hall probes fabricated from wafers provided by the two mentioned groups: wafers 1a and 1b were provided by Gossard's group and wafers 2a and 2b by Shtrikman's group.

The size of the Hall probes are similar, with the width of Hall cross arms being about 1.5 μm. However, we were unable to accurately measure this size (with AFM for example); only an estimate has been made using an optical microscope. This means that the comparison is not quite as meaningful as it would be for Hall probes having exactly the same size.

From Table 4.2 we can see that Wafers 1 would appear to be much better than Wafers 2, since Wafers 1 have a much higher electron mobility and a lower electron concentration. Indeed, the Hall coefficient R_H (column 4 in Table 4.2) and the Hall sensitivity S (column 5 in Table 4.2) are much larger for Wafers 1 than Wafers 2. The electrical conductivity $\sigma = ne\mu$ is also a little higher for Wafers 1 than Wafers 2.

However, there is more to a quality Hall probe than just its electron density and mobility. Its *noise* must be low as well. In principle, the main contribution to the noise of Hall probes at low temperatures should come from the Johnson noise of the Hall voltage contacts:

$$e_J = \sqrt{4k_\mathrm{B}TR_\mathrm{v}\Delta f}, \tag{4.7}$$

where k_B is Boltzmann constant, T is the temperature in Kelvin, R_v is the probe resistance (including the voltage leads), and Δf is the frequency measurement bandwidth. For some of our Hall probes we reduced the probe resistance as low as 1.5 kΩ at 4.2 K, which gives a Johnson noise of about 0.5 $\mathrm{nV}/\sqrt{\mathrm{Hz}}$. This would be incredibly low, and indeed the noise of the room-temperature amplifier will be higher. Unfortunately, the measured noise of our Hall probes at low temperatures is always much higher than the Johnson noise. In general, the noise is highly non-Gaussian.

Also is present the noise characteristic of two-level systems, which suggests the existence of impurity centers in the active area of the probe, probably around the doped layer. Such imperfections can cause trapping and emission of electrons and thus make the electron transport much noisier than expected. Another argument which sustains this explanation is the large offset voltage superimposed on the Hall signal, even at zero field. This offset voltage is due in part to the slight misalignment of opposite contact, but most of it must be explained in terms of microscopic inhomogeneities which are present in the heterostructure. Fortunately, the offset voltage of the Hall probe can be subtracted, and we measure the value of the magnetic field relative to a zero reference.

In column 7 of Table 4.2 is the measured magnetic noise $e_{\rm B}$, which is the ratio between the voltage noise and the Hall sensitivity, so that $e_{\rm B} = e_{\rm n}/S$. In column 8 is the estimated *signal to noise ratio* SNR $= V_{\rm H}/e_{\rm n}$ at an applied field of 1G; here $e_{\rm n}$ is the rms voltage noise measured over the normal ($\approx$ 30 Hz) bandwidth used during scanning, rather than per root Hertz as before. We see that although Wafers 1 have better parameters n and μ than Wafers 2, the SNR of Hall probes fabricated from Wafers 1 is not necessarily better than those fabricated from Wafers 2.

4.2.3 General concepts in GaAs photolithography

Photolithography is the technology which uses light to selectively remove parts of a photosensitive coating (called the photoresist), defining the desired pattern in the coating over the sample's surface. The pattern is subsequently replicated over the sample's surface with different techniques like etching or evaporation. The exposure of the photoresist can be done in different ways: by using light (*photolithography*), an electron beam (*e-beam lithography*), x-rays (*x-ray lithography*), or an ion beam (*ion-beam lithography*). Though photolithography has been used extensively in silicon process engineering, the same general concepts are applied in GaAs processing: apply a photoresist to the wafer, expose it through a mask, develop it to the desired patten (defined by the mask), replicate this pattern by using a specific etchant, and finally dissolve the photoresist with a solvent.

There are different types of photolithography. The most popular are:

- **proximity printing** The mask is placed in close proximity to the wafer but not in contact with it.
- **contact printing** The mask is placed in proximity to the wafer for alignment and then vacuum clamped directly against the wafer for exposure.
- **projection printing** The mask pattern is optically projected on the wafer.

Each of these techniques has its advantages, but for reasons of simplicity and convenience we chose to use projection printing photolithography. High quality features like integrated circuits are usually achieved in optical lithography by using special masks. These are made by patterning the desired features onto a chromium film evaporated on a fused quartz plate. The standard size of these plates are 6 in × 6 in, and they cost more than $ 500. Considering the continual changes and improvements needed in our fabrication process, it would be difficult to operate with such masks. We circumvented this issue by fabricating home-made masks on black and white photographic film which are framed in plastic slide mounts. This gives a tremendous savings of expenses, and a fast and easy fabrication process. To project our photographic masks onto the photoresist that covers the wafer we use an ordinary

Nikon optical microscope. The linewidths achieved in patterning the photoresist are not determined by such photographic masks, but rather by the wavelength of the light that we use, and the projection of the light through the optical lenses of the microscope.

In general, we can improve the resolution by using shorter wavelengths. As is well known, if a point is imaged onto a surface by a perfect (diffraction limited) optical system, the image will not be a point but a spot, with a nonuniform Airy pattern distribution. The distance r in the image plane between the central peak of the distribution and the first minimum is called the resolution of the system: $r = 1.22\lambda/(2\ \mathrm{NA})$, where λ is the wavelength of the light and $\mathrm{NA} = n \sin\alpha$ is the numerical aperture of the optical system (n is the index of refraction and α is the half-angle of the aperture of the objective). Thus, a shorter wavelength allows greater resolution. This is why ultraviolet (UV) light (λ = 100–400 nm) is used in the lithography process.

We use a tungsten halogen lamp (OSRAM HLX 64610) which provides light with wavelength in the range of 350–1700 nm. The 100 magnification objective of our Nikon microscope has a numerical aperture NA = 0.9. This means that, using the above formula, the resolution can not be better than 300 nm. The achieved resolution in our lithographical projection is about 500 nm.

The photoresists are either *positive* or *negative*. Positive photoresist is removed from the exposed area by a developer, while negative remains only in the exposed portions. In general, the positive photoresists are believed to have a better resolution. We use positive photoresists manufactured by Shipley Company Inc. We use different Shipley photoresists to get the desired thickness of resist: S1805 for 0.5 μm, S1813 for 1.2 μm, S1818 for 1.7 μm, and S5405 for 5 μm thickness. The developers for these Shipley photoresists are from the Microposit MF-319 metal-ion-free developer family.

After photoresist coating is patterned over the GaAs wafer's surface, the next step is to translated this pattern on the surface by a wet chemical etch process. In this process the uncovered area is subjected to the etchant action and the GaAs material is removed from that window. Wet etching proceeds through a chemical reaction that occurs at the surface of the material. Almost all GaAs etchants act by first oxidizing the surface and then dissolving the oxide, thereby removing some of the gallium and arsenic atoms. A typical GaAs etchant is H_2SO_4-H_2O_2-H_2O. In this case, the hydrogen peroxide is the oxidizing agent and the sulfuric acid dissolves the resulting oxide.

Though there is a wide choice of GaAs etchants, since almost any combination of oxidizer and oxide-dissolver will operate as an etchant, we chose to use an etching solution of H_3PO_4-H_2O_2-H_2O [85]. This GaAs etchant has a reliable and reproducible etching rate of less than 0.1 μm/min with an accuracy of several tens of angstroms. A formulation of 1:1:78 of H_3PO_4-H_2O_2-H_2O gives an etching rate of about 900 Å/min. Because GaAs has an anisotropic zinc-blende crystalline structure, any etching agent will have an anisotropic etching action on the GaAs lattice. In general we use GaAs wafers cut along the crystallographic planes (100) (the wafer's faces are parallel to the (100) crystallographic planes). There are two natural cleavage directions perpendicular to each other in these planes: direction $[1, 1, 0]$ and direction $[\bar{1}, 1, 0]$. We use these two directions for scribing when the wafer is broken into separated chips. The etchant has different rates on each crystallographic direction, but in general will make either an outward or an inward slope profile under the photoresist. When we etch for a longer time (about ten minutes to get a deep mesa corner of the Hall probe) we watch the action of etchant under the microscope in order to stop the etch before it damages the patterned area.

4.2.4 Hall probe fabrication

Wafer cutting process. Hall probe fabrication starts by cutting apart a 6 mm × 6 mm piece of material from which we will eventually get four independent Hall probes on 3 mm × 3 mm chips. We do this by scribing fairly deep grooves to separate 6 mm × 6 mm pieces from the original wafer, and then breaking them apart. Though the resulting edges are not clean, this isn't important because the key features will be located in the middle of these 6 mm × 6 mm chips.

Thinning of the Wafer. Our original GaAs/AlGaAs wafers are about 350–450 μm thick. Because we can use only very light scribes in breaking them into four probes, we have to thin them to facilitate the scribe/break process. We do this by grinding them to a thickness of about 250 μm. We first spin a thick photoresist (about 6 μm) on the top surface of the chips in order to protect the surface. Then we take the chips and glue them with crystal bond face down on a glass disk. Usually we glue three uniformly distributed chips on the glass disk. This disk is fit inside of a teflon puck in such a way that the chips remain above the puck's rim. For grinding we use a 5 μm granulated alumina powder mixed in DI water. By lightly pressing down on puck and slowly pushing it in a figure-eight pattern on a glass plate, we can grind in a very controllable way. After the grinding the chips are rinsed in acetone-methanol-deionizer (DI) water (see below) and glued onto microscope cover glasses.

Wafer mounting process. For easy manipulation we mount each chip on a cover glass using crystal bond. On a 100°C hot plate we place the cover glass, and in the middle of this we put a few pieces of crystal bond. When the crystal bond is melted, the chip is set on top of it and by slowly moving the chip with tweezers, a uniform spread of the crystal bond between the cover glass and the chip is assured. In this way we make a good contact and prevent the crystal bond from being washed out by acetone in subsequent rinses. If some crystal bond accidentally covers part of the chip surface, an acetone-methanol-DI water rinse is done. At the very end of fabrication process the chip is removed from the cover glass on the hot plate.

Wafer cleaning process. The cleaning step is made by rinsing the wafer in acetone, methanol and DI water. The chip is held by its cover glass and rinsed with a steady stream of acetone. Before the acetone starts to dry we rinse the chip with methanol. This removes the acetone and any organic remains. The last step is to rinse the chip surface very well with DI water. Then, placing the chip on a filter wiper, we blow it dry with N_2 gas. If the surface looks dirty or contaminated, a cleaning in acetone for a few minutes in an ultrasound bath is usually tried.

Photoresist application process. Before applying any photoresist the chips are rinsed and cleaned once more with acetone-methanol-DI water. The sample (mounted on cover glass) is prebaked for 1 to 2 minutes on a 120°C hot plate to remove all moisture and ensure a good adhesion of the photoresist. Then the sample is placed on a spinner chuck and covered with a few photoresist drops. Usually we spin the photoresist at a speed of about 5000 rpm for 30 s. This will assure a uniform spread out photoresist layer over the sample's surface, especially in the central part of the chip where the micro-size features will be patterned. After spinning, the sample is soft baked on a 95°C hot plate. This is intended to harden the photoresist, which leads to improved linewidth control, elimination of some standing wave effects, and an overall increase in contrast.

Lithography steps in Hall probe fabrication. The first major step is to generate the desired pattern onto a mask. In a conventional photolithography masks are made from glass covered with hard surface materials such as chromium or iron oxide. The patterns are generated using computer-aided design (CAD) systems; the digital CAD output drives a pattern generator that transfers the patterns directly to the photosensitive masks. This is quite expensive and impractical for Hall probe development because the mask pattern needs to be continually changed as the process is optimized. We avoid all these issues by making our masks on regular camera film framed into slide mounts. The mask pattern is projected onto the photoresist under a Nikon microscope which has 4 different objectives: 5, 20, 40, and 100 magnification. Each magnification is used to shoot features of different sizes (100x is used for micron-size features, whereas 5x for mm-size features).

On each 6 mm × 6 mm chip, four independent Hall probes are projected. The micron-size features (the "small features") of these four Hall probes are shot at 100x in the middle of the chip. These are the thinnest features of the Hall probe. The small features include four Hall crosses with short lead extensions, the projection area size at 100x being of about 200 μm in diameter (see Fig. 4.11). We project the small features in the central part of the chip because the photoresist coating (made in spinning process) has a uniform thickness only in the middle. The rough mask alignment is made at 5x magnification where we can see the projection of the mask on the chip. Also at 5x magnification the light uniformity is checked over the projection area by measuring the light intensity at different places. The four Hall probes are separated by 20 μm crossing gaps. These gap regions are reserved for a final scribing when we separate apart the four Hall probes.

To do the lithography of the small features we have used Shipley 1818 photoresist (about 1.2 μm thick) and MF-319 for developing. A couple of test exposures are made at different exposure times in order to get the best-looking profile of the pattern

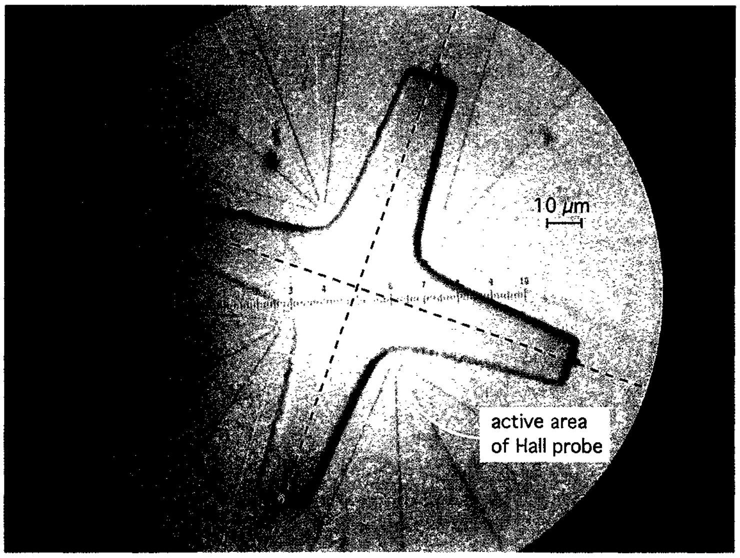

Figure 4.11: Micron-scale features in the Hall probe lithography. The middle etched cross separates four independent Hall probes. At the end of fabrication process, these four probes will be separated apart by breaking the chip along the dotted lines.

onto photoresist coating. After we open the correct windows in the photoresist coating, the H_3PO_4-H_2O_2-H_2O etching solution is used to etch these small features onto the GaAs chip. Before each run the action of the etchant on a test GaAs chip must be checked in order to be sure that the right depth will be achieved on the real chip. It is possible that over time the etchant solution changes somewhat. An Alpha-Step thickness profiler is used to measure the depth of etching.

As is shown in Fig. 4.10, the important layer structures that give the high-mobility 2D gas are located in our GaAs wafer about 1000–2000 Å below the top surface. However, in order to make a circuit pattern in the 2D gas we needn't etch so deeply. It is sufficient to etch only about 1000 Å deep, because the etched regions cause surface states that deplete the donors so that there is no 2D electronic gas below the etched areas.

After the small features are made, we proceed to fabricate the "intermediate features" and the "large features". These serve to extend the lead pattern from the micron area (where the Hall crosses are made) to near the chip edges where the contacts will be evaporated. Because the photoresist tends to bead up near the chip edges, it is necessary to do a separate exposure for them in order to clear out the photoresist and open sharp edge windows into it. Of course, the separation between these lead extensions is done using the same wet chemical etching procedure.

A particularly difficult step, since it can damage the small features, is to make a deep cross-shaped etch in the gap regions between the four Hall probes. This cross is shown in Fig. 4.11. This deep etch is intended to make a round mesa corner on the four Hall probes in close proximity to the Hall cross. The distance from the etched corner to the Hall cross center is about 7 μm. In a scanning experiment, the Hall probe is tilted with respect to the sample plane, and the contact with the sample is done by this etched mesa corner, not by the actual corner of the chip. Thus, we need to make the etch quite deep (about 4 μm) in order to be sure that the contact is done by the mesa corner and not the chip edge. Because the etching proceeds laterally towards the small features as well as down, we observe the etch process under the microscope in order to be sure that there will be not any damage to the small features area. Sometimes it is necessary to make two consecutive etchings to get the desired

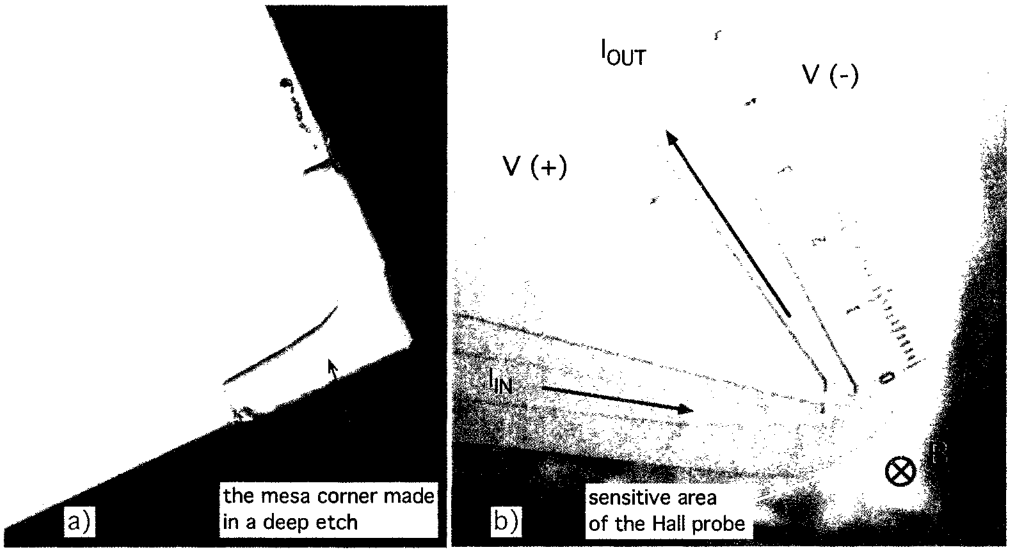

Figure 4.12: The corner with active area of the Hall probe (micron-scale features). In b) is shown the electric diagram of the Hall sensor with the magnetic field pointing perpendicular on the surface of the chip. One small division is 1 μm.

depth.

In Fig. 4.12 is shown the corner with the active area of two fully processed Hall probes. In Fig. 4.12a we can see very clearly the deep etch around the corner of the chip. Generally, the current and voltage leads have the same width (which gives them the same resistance) as in Fig. 4.12a. In Fig. 4.12b, the voltage leads are spread over larger area in order to reduce their resistance compared to that of current leads. We used Hall probes with this modified design to detect high speed flux-flow, in which case we wanted to reduce the resistance of voltage leads in order to obtain a large bandwith for our measurement line. This experiment is discussed in Chapter 6.

The arms of the Hall cross on our sensors are 1–1.5 μm wide (see Fig. 4.12b) which defines an active area of about 1.5 μm^2. It was shown [86] that the Hall response doesn't depend on the magnetic field distribution $B(x, y)$ inside of the cross but, simply, is the average magnetic field over the cross area $\langle B\rangle = \int B dx dy/A = \Phi/A$, where A is the Hall active area. This is the reason why people try now to reduce the size of the Hall active area. Reducing the size of the Hall cross will allow us to see smaller magnetic flux structures which otherwise are washed out in the averaging response of the Hall probe.

The last lithographic step is to project a pattern for contacts. In order to get a low electrical resistance of the Hall leads, I have made the contact leads all the way from the outer chip edges near to the region of the small features. At the inner part, the separation between leads is only limited by the realization of a good lift-off of the metal evaporated for contacts (this separation is about 10 μm on our Hall probes). So, after this last step, the whole chip is covered by a thick photoresist coating excepting the open windows for contacts. We use 5 μm thick photoresist in order to have an easy lift-off.

Contact metallization. Ohmic contacts on GaAs wafers are fabricated by applying a particular metallization and then alloying the metal into GaAs. The most common procedure for contacting n-type GaAS is to use a combination of gold-germanium-nickel. A very instructive description of this procedure and details about the involved chemistry can be found in Williams' book [87]. The germanium dopes the GaAs during the alloy. The nickel serves as a wetting agent and favors the Ge

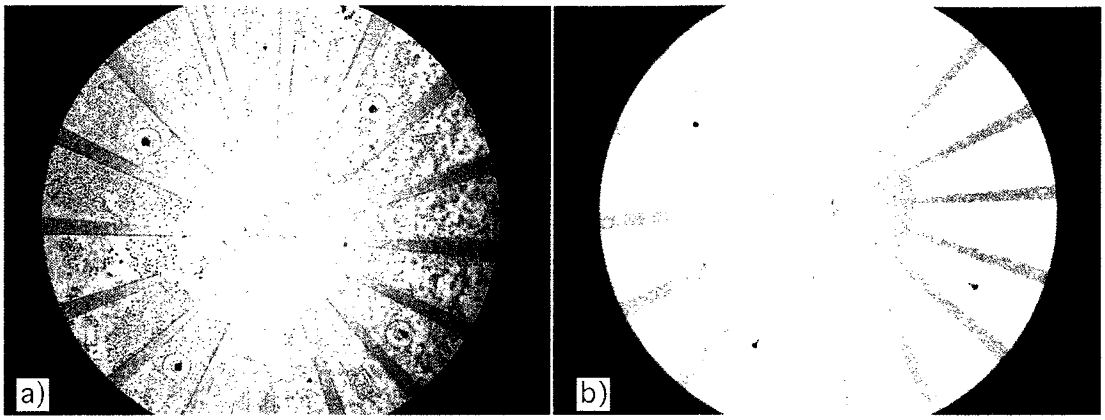

Figure 4.13: Ohmic contacts on GaAs wafer are done by alloying a AuGe/Ni/Au metallization into wafer. The diameter of the circle of view is 3.65 mm.

diffusion into GaAs. The recipe suggested by Williams and used by us is as follows: we deposit first a layer of AuGe (1300 Å thick), then a layer of Ni (365 Å thick), and finally a last layer of Au (1200–1300 Å thick). We use a AuGe eutectic alloy (88/12 weight percent ratio). A fairly thick overcoat of Au is recommended in order to decrease the sheet resistance of AuGeNi metalization (about 2 $\Omega/\square$).

Before evaporating the desired amounts of AuGe/Ni/Au, we rinse the GaAs chips in HCl for one minute in order to remove the oxide layer formed on the GaAs surface. Then, the chips are blow dried with nitrogen gas and very quickly placed in the evaporator. The pressure during the evaporation is about 10^{-6} Torr. After evaporation, we do a thermal annealing of the chips to alloy the metallization into the GaAs wafer. The wafer is heated to 400°C and the AuGe alloy diffuses into wafer and acts as a dopant. In Fig. 4.13 are shown two Hall chips with contacts on them: in a)

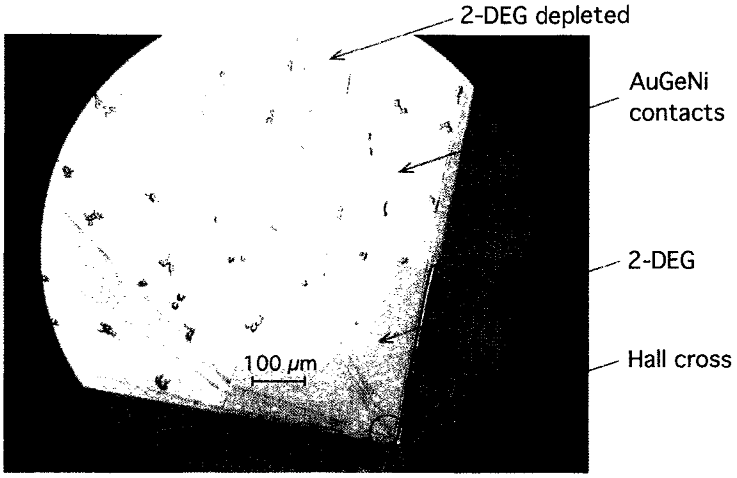

Figure 4.14: The bottom part of Hall probe's contacts.

the whole AuGe/Ni/Au metallization was annealed whereas in b) the last Au layer was evaporated after annealing. We found better ohmic contacts for the first case. As can be seen in a) after annealing some unusual structures have been occasionally observed. These are believed to be gallium atoms puddling on the surface of gold overlayer. In Fig. 4.14 is shown the bottom part of the contacts of a Hall probe used in detecting high speed flux flow. The narrow separation between the contacts (at their very ends) is about 10 μm, enough to assure a good lift-off of metallization between contacts.

Chapter 5

Vortex Nucleation in Narrow Thin-Film Strips

Vortex dynamics in low-dimensional materials has received a renewed interest from the perspective of possible applications of these materials in novel superconducting devices. Vortices play a fundamental role in the magnetic behavior of superconducting state: they determine the critical fields for superconductors; they determine many of the transport properties of superconductors, such as critical current and electrical resistance; and their dynamics is interesting not only as a physical process but also from the perspective of vortex-control devices such as periodic pinning arrays, Josephson-junction devices, vortex pumps, and ratchets.

One major issue in designing high performance superconducting devices such as SQUIDs or future superconducting qubits is the possible noise induced by the presence of vortices. This is because, although vortices become trapped to pinning centers when the temperature is reduced below a threshold value, they still have a

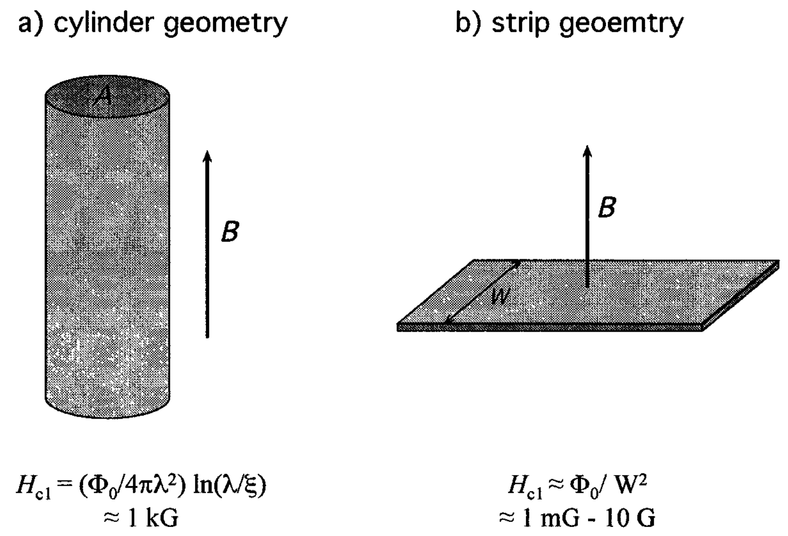

Figure 5.1: The lower critical field for two different geometries: a) thin-long cylinder in a parallel magnetic field and b) thin, narrow strip in perpendicular magnetic field.

temperature-dependent jiggling around to their locations. Consequently, the measurement of the flux over some area, done by example with a SQUID, will be affected by this tiny flux change caused by a vortex present in the investigated area. One solution is to design devices with leads narrow enough to expel the ambient fields; in this way there will be no vortices present [88].

The textbook case of a superconductor in a magnetic field treats the case of a long superconducting cylinder in a parallel applied magnetic field. In this case, the lower critical field H_{c1}, at which vortices first penetrate, is easy to calculate. It depends *only* on material parameters (i.e., the coherence length ξ and the penetration depth λ) and is *independent* of any geometrical dimensions such as the cross-section A (see Fig. 5.1a).

However, the common geometry used in superconducting devices, that of a long, narrow thin-film strip of width W in a field directed perpendicular to its planar face, has received much less attention. Although some theoretical work has been done on this particular geometry, our experiment is the first one which directly images the flux configuration in superconducting strips of different width at low magnetic fields.

Using scanning Hall probe microscopy, we have measured the maximum field for which vortices are completely expelled from a thin-film niobium superconducting strip [89]. We found that the maximum field B_m below which the vortices are expelled from a superconducting narrow strip scales with the strip's width W as $B_m \approx \Phi_0/W^2$ and is almost independent of material parameters (see Fig. 5.1b). Above this field vortices nucleated into the strip with a density increasing approximately linearly with the field. These results are presented in Section 5.4.

In Section 5.1, the particular features of vortices in thin-films are compared to those of bulk vortices. In Section 5.2, we will see how the first vortex nucleation occurs in a narrow strips. A theoretical model describing the vortex nucleation in narrow thin-film strips is presented in Section 5.3. Finally, the results of our experiment on vortex nucleation in narrow strips are presented in Section 5.4.

5.1 Abrikosov versus Pearl Vortices

Magnetic flux penetrates bulk or thick-film type-II superconductors ($\lambda > \xi$) in the form of quantized vortices which, in a clean sample, form a triangular lattice

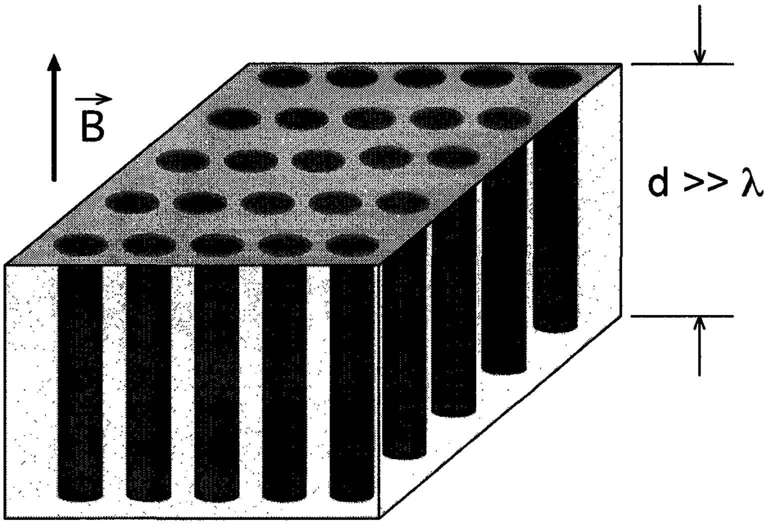

Figure 5.2: Abrikosov vortices in a thick type-II superconducting film; "thick" means that the thickness is much larger than the London penetration depth of the film.

(see Fig. 5.2). They are called Abrikosov vortices, being first predicted by Abrikosov in 1957 [10]. Each vortex has a single magnetic flux quantum $\Phi_0 = ch/2e = 2.07 \times 10^{-7}$ G cm^2 associated with it. In the London approximation [90] (valid for $\lambda >> \xi$), the Abrikosov vortex is modeled as consisting of a long cylindrical normal filament of radius ξ (normal core), surrounded by annular supercurrents. As the field is increased, the vortices become denser and denser, their normal cores start to overlap, and the sample goes normal in fields higher than the upper critical field.

The London equation considers the electromagnetic field and supercurrents of a single vortex in an bulk isotropic, high-κ superconductor ($\kappa = \lambda/\xi$ is the Ginzburg-Landau parameter). In an applied magnetic field **h** parallel to the z-axis, the London equation for a single vortex located in the origin of the coordinates system and having the core centered along the z-axis is (in CGS units) [91]

$$\mathbf{h} + \frac{4\pi\lambda^2}{c}\,\mathrm{curl}\,\mathbf{j} = \Phi_0 \hat{\mathbf{z}} \delta_2(\mathbf{r}), \tag{5.1}$$

where λ is the bulk London penetration depth, $\mathbf{j}$ is the supercurrent density in the (x, y) plane, and $\hat{\mathbf{z}}$ is the unit vector along the z-axis; $\mathbf{r} = (x, y)$. The vorticity due to the vortex supercurrents is included in the right part of the equation, $\delta_2(\mathbf{r})$ being the two-dimensional delta function which considers the singularity along the z-axis at the vortex location. Outside the vortex core, the magnetic field is given by

$$h(r) = \frac{\Phi_0}{2\pi\lambda^2} \mathrm{K}_0\left(\frac{r}{\lambda}\right), \tag{5.2}$$

where K_0 is the zeroth order Bessel function of the second kind. Near to the vortex core, the magnetic field behaves as

$$h(r) = \frac{\Phi_0}{2\pi\lambda^2} \ln\left(\frac{\lambda}{r}\right) \qquad (\xi \leq r \ll \lambda). \tag{5.3}$$

whereas, far way from the core, the magnetic field decays exponentially as

$$h(r) = \frac{\Phi_0}{2\pi\lambda^2} \sqrt{\frac{\pi\lambda}{2r}} \exp\left(-\frac{r}{\lambda}\right) \qquad (r \gg \lambda). \tag{5.4}$$

In an ideal superconductor (without defects), the interactions between Abrikosov vortices (mainly given by the interaction between their screening currents) is described by a short range repulsive potential:

$$V(r) = \frac{\Phi_0^2}{8\pi^2\lambda^2} K_0(r/\lambda), \tag{5.5}$$

where r is the distance between the two vortices. Thus, at short distances, the interaction energy—the energy per unit length of the vortex filament—diverges as $\ln(|\ \lambda/r\ |)$ and at large distances decreases as $(1/\sqrt{r})\mathrm{e}^{-r/\lambda}$.

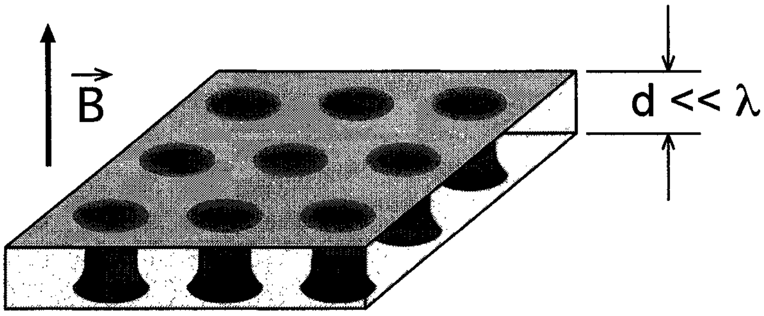

Figure 5.3: Pearl vortices in a thin type-II superconducting film; "thin" means that the thickness is much smaller than the London penetration depth of the film.

In contrast to the bulk vortices discussed above, in a superconducting thin film ($d \ll \lambda$, where d is the film thickness), vortices interact primarily through their magnetic fields in the free space above and below the film. This case was first discussed by Pearl [92] (see Fig. 5.3). In the London approximation, the electrodynamics of a single Pearl vortex is given by the London equation averaged over the film thickness d [91]:

$$h_z + \frac{4\pi\Lambda}{c}(\mathrm{curl}\,\mathbf{j}_s)_z = \Phi_0\delta(\mathbf{r}), \tag{5.6}$$

where $\mathbf{j}_s = d\mathbf{j}$ is the sheet current density and $\Lambda = \lambda^2/d$ is the effective penetration depth for a thin film. Either by following the method described in deGennes's book (p. 60) [91] or by solving the Laplace equation with boundary conditions given by the averaged London equation [93, 94] we can get the field distribution of a single Pearl vortex:

$$h_z(z,\mathbf{r}) = \frac{\Phi_0}{2\pi}\int_0^\infty k\frac{J_0(kr)}{1+2\Lambda k}\mathrm{e}^{-k|z|}dk, \tag{5.7}$$

where J_0 is the zeroth order Bessel function of the first kind. Thus, for a thin film, the magnetic decay of the vortex field is characterized by the effective penetration depth Λ. We consider here only the z-component of the vortex field because this is what we measure in a magnetic imaging: the average of the z-component of the magnetic field over the active sensor's area.

From Eq. 5.7 it may be shown that, just above the film, the magnetic field of a Pearl vortex will behave as $\Phi_0/4\pi\Lambda r$ at short distances ($\xi < r \ll \Lambda$) whereas far away from the core ($r \gg \Lambda$) the decay will be as $2\Phi\Lambda/\pi r^3$. Accordingly, the sheet current density is $j_s = c\Phi_0/8\pi^2\Lambda r$ near the core and $c\Phi_0/4\pi^2r^2$ far from the core.

In conclusion, for an Abrikosov-type vortex the magnetic field decays almost exponentially from the vortex core over the penetration depth λ, whereas for a Pearl type-vortex the decay is as a power law, $1/r^3$, at large distances. This increases the interaction between Pearl vortices compared to the case of bulk Abrikosov vortices.

5.2 First Magnetic Flux Penetration in Superconducting Strips

The lower critical field H_{c1} for a type-II superconductor is defined as the field at which a single vortex is thermodynamically favored to be into the material. In this section we will discuss the physical meaning of this magnetic field penetration.

In the case of a long cylinder in a parallel applied field (mentioned in the previous section) for example, H_{c1} is calculated by comparing the Gibbs free energies of the Meissner state (no vortices) and the state with only one vortex present. The Gibbs free energy is used as a thermodynamic potential in the case when the magnetic field H is held constant. When B is held constant rather than H then we used the Helmholtz free energy F in thermodynamic considerations.

Let's see how the Meissner state is actually defined. There are two ways to put a magnetic field inside of a superconductor. The first one, called *zero field cooled* (ZFC), is when the material is cooled below the critical temperature T_c without any magnetic field present and then an external magnetic field is turned on. At low values of the field, below H_{c1}, the magnetic field is *excluded* from the material whereas at high values the field *penetrates* inside. The second way is called *field cooled* (FC): the field is turned on when the material is in its normal state (above T_c) and thus penetrates inside; then the material is cooled below T_c in the presence of the magnetic field. If the field is lower than H_{c1} it will be *expelled* from the material. This last case is the right situation to get *the Meissner state.* Consequently, the lower critical field can be seen as the highest field at which, in a FC process, the superconductor will still retain the Meissner state. This is the procedure that we followed in our experiment, to be described in Section 5.4, to measure the lower critical field for narrow thin film strips in a perpendicular applied field.

The Meissner state (perfect diamagnetism) follows from the reaction of the superconductor in the presence of an external magnetic field. When a magnetic field exists outside of the superconductor, shielding currents (or Meissner currents) start

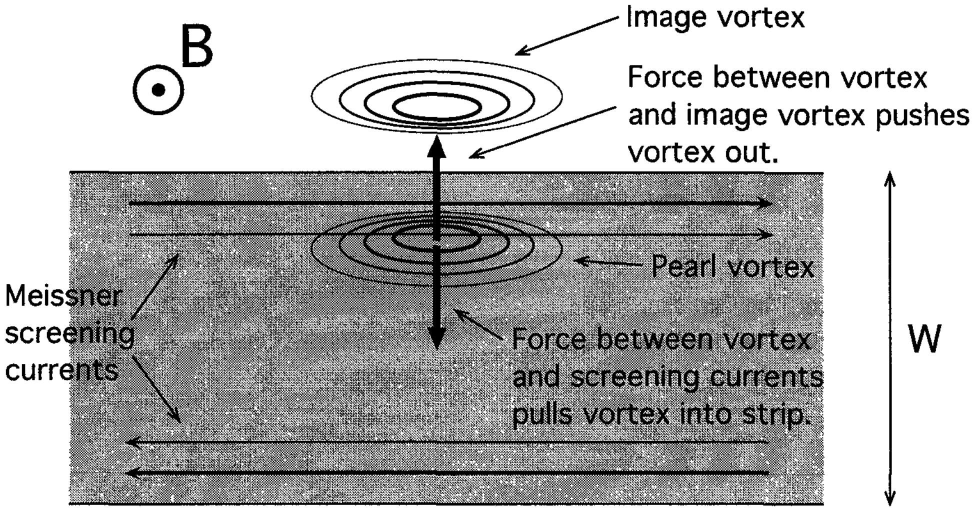

Figure 5.4: First vortex penetration inside of a narrow strip in a perpendicular applied magnetic field.

to flow in a surface layer of thickness λ around the superconductor. They shield (or screen) the interior of the superconductor by producing a field that cancels the applied field in such a way that inside the magnetic induction will be zero.

The first vortex penetrates inside of the superconductor when the Gibbs free energy of the superconductor is lower with a vortex in than with no vortices. The process is determined by the competition between two separate forces which act on the vortex near to the sample's edge. In Fig. 5.4 is shown the first vortex penetration near to one edge of a narrow strip in a perpendicular applied magnetic field. First, the external applied field (having the same sign as the field of the nucleated vortex) induces Meissner currents flowing parallel to the sample edge. The interaction between the Meissner currents and the nucleated vortex is described by a Lorentz force, $\mathbf{F}_L = \mathbf{J} \times \Phi_0/c$, which pushes the vortex towards the center of the sample. Second, the vortex screening currents are distorted near the edge enforcing a boundary condition of zero current normal to the edge. This can be satisfied by placing an image vortex (antivortex), of opposite sign, outside the sample. Thus, there is an attractive force (an image force) on the nucleated vortex towards the edge.

The inward Lorentz force is proportional to the screening currents, and is thus proportional to the applied magnetic field. Therefore, at high enough fields this inward force overcomes the outwards image force, creating a position of stable equilibrium along the centerline of the film. Thus, the competition between these two forces gives a potential well that tends to hold the vortex in the middle of the film at high enough fields.

For the sake of simplicity, Fig. 5.4 shows only the one image vortex that enforces the boundary condition at the edge where the nucleation occurs. However, for this narrow strip geometry, satisfying the boundary conditions at both edges requires a whole set of image vortices and image antivortices (multiple images of the nucleated vortex in the two mirror edges).

In addition to the above description, there is also some contribution to the Gibbs free energy due to the shape of the sample. Thus, wide strips (the width $W >> \lambda$) present large demagnetization factors. In this case there is a strong distortion in the field lines around the sample edges and this affects the distribution of the screening currents inside the sample. Moreover, if the sample is thicker than the penetration depth, then the curved field lines can cause the entry of tilted vortex filaments at the sample corners. However, for the case that we analyze here, that one of narrow thin-film strips, these shape effects are negligible.

In the next section, the onset of the vortex nucleation into a narrow thin-film strip is analyzed in terms of Gibbs free energy associated to the nucleated vortex.

5.3 Vortex Expulsion from Thin-Film Superconducting Strips: Theoretical Model

In the following a theoretical model for vortex expulsion from type-II superconducting narrow thin-film strips will be presented. This presentation is based on Clem's derivation [95, 96]. The main result is that for any magnetic field there is a strip width below which no vortices will be present.

We consider a type-II superconducting film of width W $(0 \leq x \leq W)$ and thickness d $(0 \leq z \leq d)$ in an applied magnetic field $\mathbf{B} = (0, 0, B)$. The origin of the coordinate frame is chosen at the left edge of the strip with the y axis along the edges and x axis perpendicular to them. The edges are thus located at $(0, y, 0)$ and $(W, y, 0)$ (see Fig. 5.5). The strip is assumed to be narrow and thin: $\xi < d < W \ll \lambda_\perp$, where $\lambda_\perp = 2\lambda^2/d$ is the in-plane penetration depth, λ the London penetration depth, and ξ the coherence length of the superconductor. Since the in-plane penetration depth is much greater than the width of the strip we will have a weak magnetic screening and the field will penetrate almost uniformly through the strip.

Let's see how the vortex configuration evolves with the magnetic field at different temperatures. Suppose that the applied magnetic field is high enough to induce vortices into the strip. When the strip is cooled just below T_c, the nucleated vortices are very weakly pinned and quite mobile, moving around and trying to find a lower energy configuration. As the temperature is further decreased, the pinning rapidly increases and the vortex motion freezes out at a temperature T_f very close to T_c. Below T_f the vortex configuration will not change any more so the calculation should be done for a temperature range of $T_f < T < T_c$. For example, for the niobium (Nb) films, discussed in Section 5.4, the critical temperature is $T_c = 8.848$ K and the corresponding freeze-out temperature is found to be $T_f = 8.835$ K [89]. The in-plane penetration depth $\lambda_\perp$ will decrease rapidly during the cooling process between T_c and T_f but still will be many microns at T_f. Thus for our Nb strips with $d = 210$ nm, $\lambda_\perp = 24$ μm at T_f. This fact enables us to analyze the vortex energetics during freeze-out using thin-film expressions that are valid in the domain where the in-plane penetration depth is larger than the width of the strip.

Let's find the Gibbs free energy of a single vortex inside the strip in a perpendicular applied magnetic field B. According to the above considerations, in thin films ($d \ll \lambda_\perp$), the vortex will have a Pearl structure (see Section 5.1) and, for a narrow geometry ($W \ll \lambda_\perp$), it will be enough to consider only the short-distance expression for the fields and currents: $h_z(r) = \Phi_0/2\pi\lambda_\perp r$ and $j(r) = c\Phi_0/4\pi^2\lambda_\perp r$. The outward force acting on a vortex placed at x from the the origin is the sum of Lorentz forces,

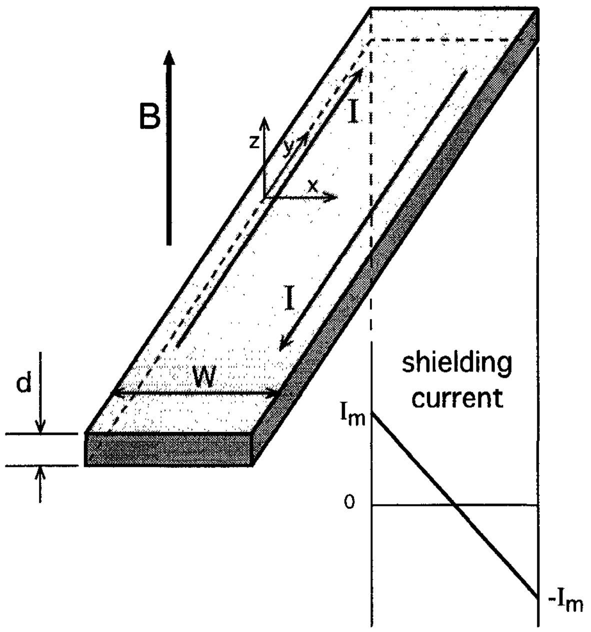

Figure 5.5: In the narrow strip geometry Meissner currents can be considered as having a linear dependence across the witdh.

$\mathbf{F}_L = \mathbf{j} \times \mathbf{\Phi}_0/c$, coming from all its image antivortices placed at $-x + 2nW(n = 0, \pm 1, \pm 2, \ldots)$ and image vortices placed at $+x + 2mW(m = \pm 1, \pm 2, \ldots)$ [95, 96]:

$$\begin{aligned} F(x) &= \frac{\Phi^2}{2\pi^2\lambda_\perp}\left(-\sum_{n=-\infty}^{0}\frac{1}{x-(-x+2nW)}+\sum_{n=1}^{\infty}\frac{1}{x-(-x-2nW)}\right) \\ &+\frac{\Phi^2}{2\pi^2\lambda_\perp}\left(-\sum_{m=-\infty}^{-1}\frac{1}{x-(x+2mW)}+\sum_{m=1}^{\infty}\frac{1}{x-(x-2mW)}\right) \\ &= -\frac{\Phi_0^2}{8\pi\lambda_\perp W}\cot\left(\frac{\pi x}{W}\right). \end{aligned} \tag{5.8}$$

As can be seen from the Eq. 5.8, the main contribution comes from the interaction with nearest antivortex image placed at $-x$. In the London approximation vortices are considered as having a hard core of radius ξ, the coherence length. Consequently, at the strip edge, a vortex and its image can not be closer than ξ. To satisfy this we need to impose a lower cutoff at the core radius ξ, the position of a vortex inside the strip being restricted to the interval $\xi/2 < x < W - \xi/2$. Now, since the force is the negative gradient of the potential, the self-energy of the vortex inside the strip is given by

$$U_s(x) = -\int_{\xi/2}^{x} F(x)dx = \frac{\Phi_0^2}{8\pi^2\lambda_\perp} \ln\left[\left(\frac{2W}{\pi\xi}\right)\sin\left(\frac{\pi x}{W}\right)\right], \quad \xi/2 < x < W - \xi/2. \tag{5.9}$$

We note that this self-energy U_s of the vortex is a function of vortex position inside the strip, having a dome-like shape with a maximum at the middle of the strip. This tends to move the vortex out of the strip. However, as it was explained in Section 5.2, when a magnetic field is applied perpendicular to the strip, there is a second force pushing the vortex towards the center of the strip, caused by the Meissner screening currents. An expression for the Meissner currents can be obtained by using the fluxoid condition for the sheet geometry [91],

$$\int_\Sigma \mathbf{h} \cdot d\sigma + \frac{2\pi\lambda_\perp}{c} \oint_C \mathbf{j}_s \cdot d\mathbf{l} = n\Phi_0 \tag{5.10}$$

applied to a small area Σ enclosed by a contour C. In the Meissner state $n = 0$ because there are no vortices present. In the limit $\lambda_\perp \gg W$, the screening currents are weak and the magnetic field is almost uniform and equal to the applied field B. Taking a rectangular contour as in Fig. 5.6 and using the symmetry of the involved geometry $[(\mathbf{j}_s)_y(x = W/2) = 0]$, we obtain the y-component of the supercurrent induced

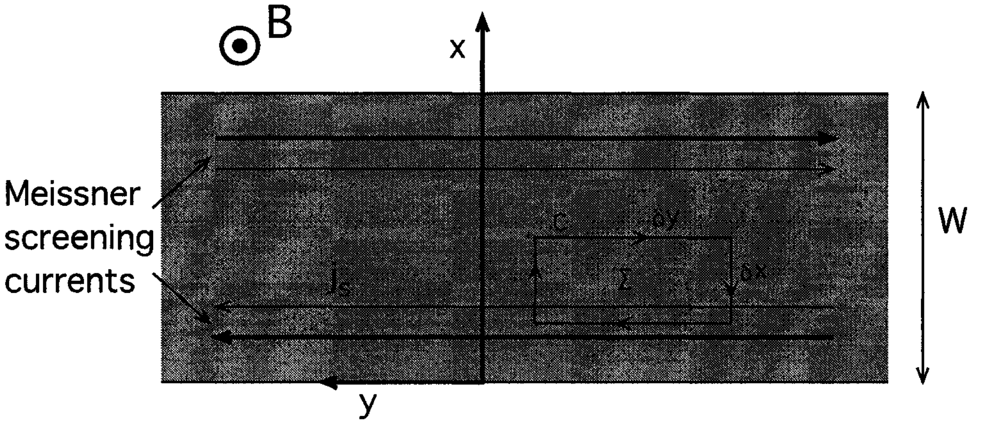

Figure 5.6: In the Meissner state the contour C includes no vortices but only the flux generated by the screening currents in response to the applied magnetic field B.

in response to the applied magnetic field (Fig. 5.5):

$$(\mathbf{j}_s)_y(x) = -\frac{cB}{2\pi\lambda_\perp}(x - W/2). \tag{5.11}$$

The Lorentz force pushing the vortex towards the middle of the strip is:

$$F_L(x) = (\mathbf{j}_s)_y \Phi_0/c = -\frac{\Phi_0 B}{4\pi\lambda_\perp}(2x - W), \tag{5.12}$$

and the corresponding interaction energy is

$$U_i(x) = -\int_{\xi/2}^{x} F_L(x)dx = -\frac{\Phi_0 B}{4\pi\lambda_\perp}\left[x\,(W - x) - \frac{\xi}{2}\left(W - \frac{\xi}{2}\right)\right]. \tag{5.13}$$

For consistency, we imposed here the same lower cutoff used above to calculate the self-energy of a nucleated vortex. The Gibbs free energy of a nucleated vortex at position x inside the strip is then the sum of the two contributions from equations 5.9 and 5.13:

$$G(x) = U_s(x) + U_i(x), \tag{5.14}$$

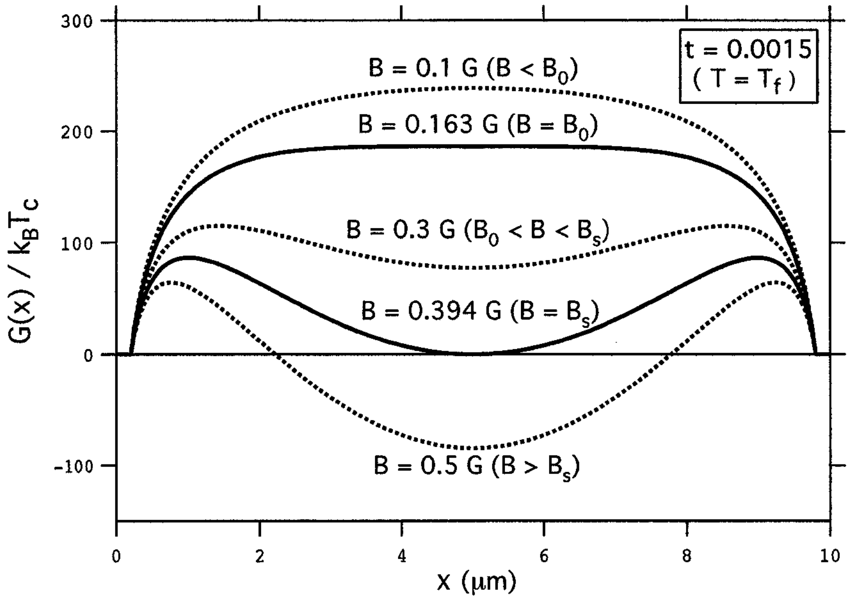

Figure 5.7: Gibbs free energy as a function of the applied magnetic field at the vortex freeze-out temperature for a 10 μm wide niobium strip.

having the value

$$G(W/2) = \frac{\Phi_0^2}{8\pi^2\lambda_\perp} \ln\left(\frac{2W}{\pi\xi}\right)\left[1 - \frac{B}{B_s}\right] \tag{5.15}$$

in the middle of the strip. In the above equation, B_s is

$$B_s = \frac{2\Phi_0}{\pi W^2} \ln\left(\frac{2W}{\pi\xi}\right). \tag{5.16}$$

Now we can analyze the behavior of the Gibbs free energy of a vortex as a function of the applied magnetic field. To make the calculation specific, we consider the situation at our experimentally-measured freeze-out temperature, $T_f = 8.835$ K. We define the reduced temperature as $t = 1 - T/T_c$. At the freeze-out temperature this is $t_f = 0.0015$. As shown in Fig. 5.7, at low applied fields, the Gibbs free energy has a dome-like shape that expels vortices; this corresponds to the Meissner state. At fields larger than

$$B_0 = \frac{\pi \Phi_0}{4W^2} \tag{5.17}$$

the Gibbs free energy exhibits a minimum in the middle of the strip, with two adjacent local maxima being present on either side of this at $x_{max} = W/2 \pm \Delta x$, where:

$$\frac{\tan(\pi \Delta x/W)}{\pi \Delta x/W} = \frac{B}{B_0}. \tag{5.18}$$

Thus, for $B > B_0$ vortices may be metastably trapped at this local minimum, since a vortex here may be unable to move over the adjacent maxima.

However, the central minimum becomes *absolutely* stable at the field B_s (given by Eq. 5.16) at which $G(W/2) = 0$. In fields higher than B_s, a vortex is definitely trapped inside, the Gibbs free energy of a strip having a vortex being lower than with no vortex. Thus, there are two fields, B_0 and B_s, which may be identified as the possible critical field for complete vortex expulsion.

A related derivation has been performed by Maximova regarding the mixed state in narrow thin superconducting strips [97]. The field for first vortex entry was found to be $(\pi\Phi_0)/(4W^2)$. The magnetic field at which the Gibbs free energy reaches zero in the middle of the strip has the same expression as given by Eq. 5.16.

On the basis of a different approach, Likharev [98] concluded that the relevant field for vortex expulsion is $(2\Phi_0/\pi W^2)\ln(W/4\xi)$, above which vortices become absolutely stable in the middle of the strip. The slightly small difference between the values obtained by Clem and Likharev comes from the choice in cutting off the vortex radius at $\xi/2$ or ξ near to the edge, respectively.

5.4 Vortex Expulsion from Thin-Film Superconducting Narrow Strips: Experiments

In order to investigate these issues, we have used scanning Hall probe microscopy to measure the maximum field at which vortices are completely expelled from narrow-thin strips [89]. Below this critical field there are no vortices trapped in the strip.

Type-II superconductors in strip geometry are of technological interest. Consequently, a lot of work has been devoted for this particular geometry, especially for wide, thick strips ($\xi < \lambda_\perp \ll d \ll W$) [99, 100, 101, 102] and wide, thin strips ($\xi < d \ll \lambda_\perp \ll W$) [103, 104, 105, 106]. The geometry that we analyze here, narrow and thin strips ($\xi < d < W \ll \lambda_\perp$), though of major technological interest, have been examined only theoretically [95, 98, 97, 89].

In our experiments, the narrow thin-film strips were cooled to below T_c at a fixed field B (FC method), in order to get the Meissner state. In this case the physical argument for correct identification of the lower critical field favors B_s, not B_0. Consider, for example, the situation in Fig. 5.8a, when the applied magnetic field is between B_0 and B_s at some temperature below T_c. Although at low temperatures (say $t \sim 0.0015$) a vortex could be trapped in the metastable well at $x = 0$, to get to $t \sim 0.0015$ we must pass through temperatures closer to T_c, such as $t \sim 0.0005$. At that higher temperature, the escape barrier is much smaller than the re-entry barrier.

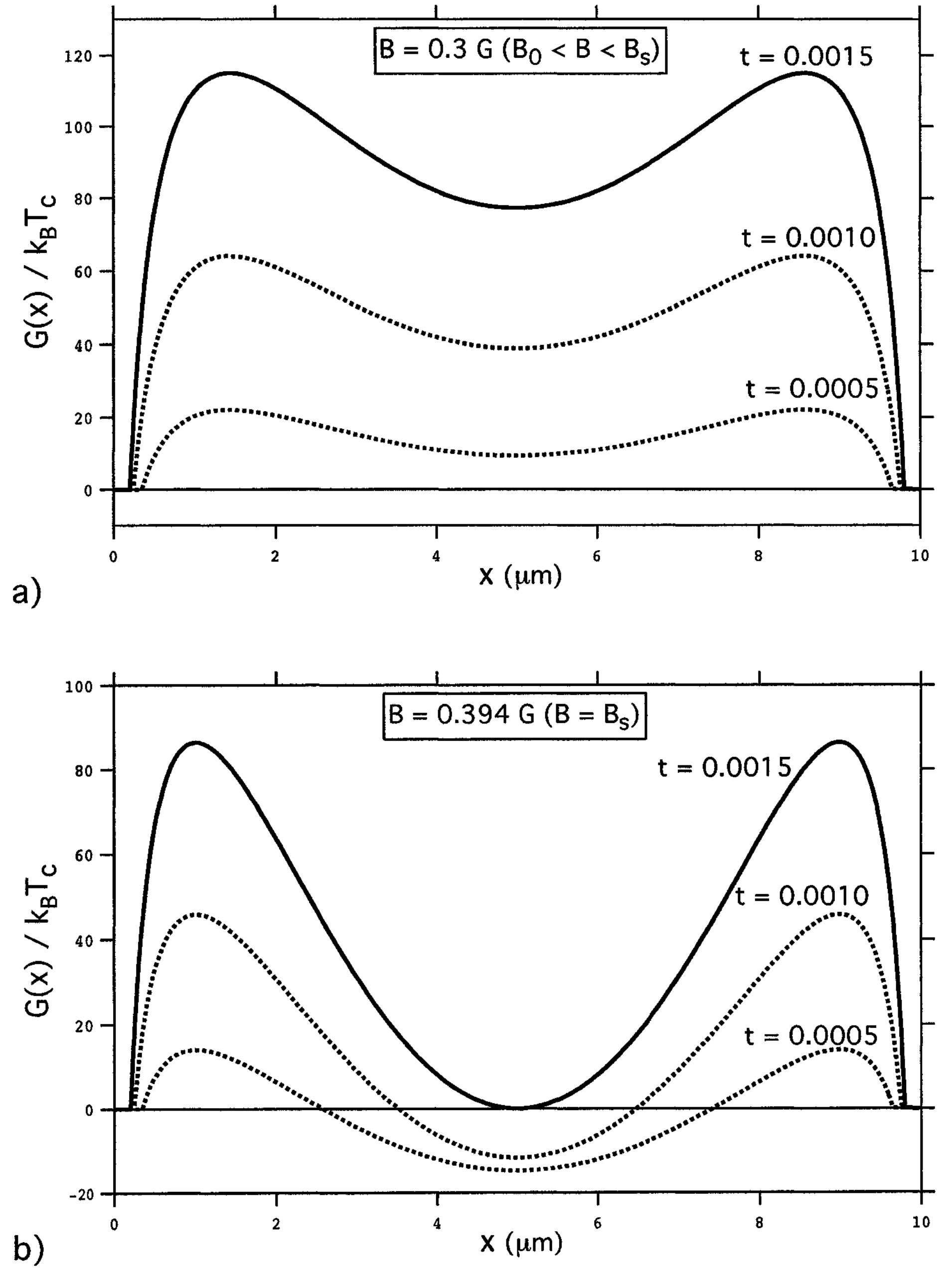

Figure 5.8: Temperature dependence of the Gibbs free energy of a 10μm wide strip at: a) a field smaller than the lower critical field B_s and b) a field equal to the lower critical field B_s.

So, it is very likely that any such metastable vortex would escape and not be able to return. This is not the case, however, when the strip is field-cooled in a field just above B_s (Fig. 5.8b). In this case, a vortex trapped in the middle would be absolutely stable at all temperatures below T_c since $G(x = 0) \leq 0$.

Strip Parameters. Our strips were fabricated at NIST-Boulder from sputtered niobium films of thickness $d = 210$ nm using photolithography and subsequent reactive ion etching. They were 4 mm long and had widths of 1.6, 10, and 100 μm. These three widths cover the range over which the strips can be called "narrow" ($W \ll \lambda_\perp$). Our strips had a transition temperature $T_c = 8.848$ K and, as mentioned earlier, a vortex freeze-out temperature $T_f = 8.835$ K, so that the corresponding reduced temperature is $t_f = 1 - T_f/T_c = 0.0015$. The error in these temperature measurements was ±1 mK.

We measured T_f as follows. After field-cooling a 10 μm strip from above T_c in a field of 840 mG, we remove the field and then made a one-dimensional scan over the center line of the strip, thereby imaging the trapped vortices. During the scan the temperature was very slowly raised from T=8.820 K to above T_c (at a rate of 0.1 mK/s). This scan is shown in Fig. 5.9, where the vortices appear as dark vertical traces. We see that the first vortex-defreezing (the middle trace) occurs at 8.835 K and this was identified as the freezing temperature T_f. The last vortex-defreezing happens at the critical temperature $T_c = 8.848$ K. The freeze-out temperature is local material parameter which depends on the local pinning landscape. Thus measurements over

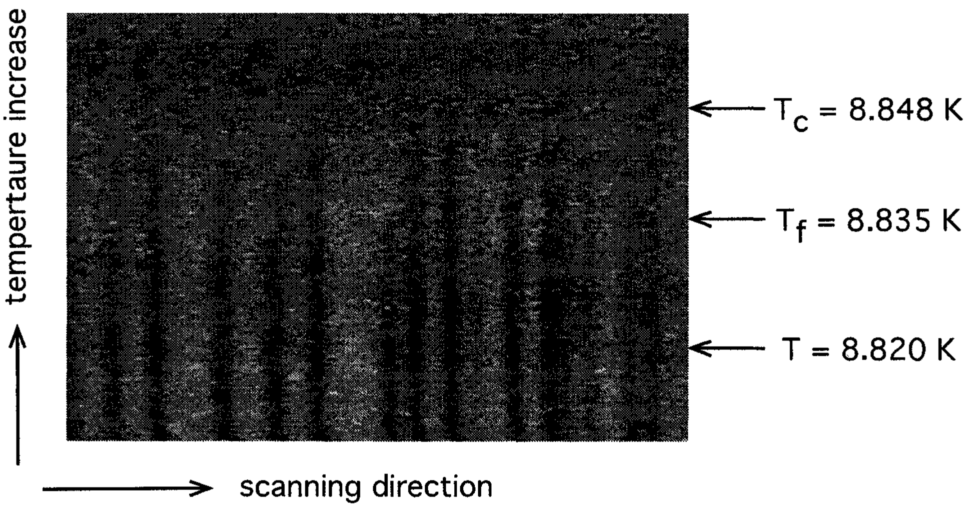

Figure 5.9: One-dimensional scanning over several vortices along a 10 μm strip while the temperature was varied by 0.1 mK/s near the superconducting-normal transition.

different areas should provide a distribution of this parameter's values. However, our measured value of $T_f = 8.835$ K is consistent with previous measurements [107, 108] which found that vortex depinning in niobium films occurs in a range of 50–200 mK below the critical temperature.

The temperature dependence of the Ginzburg-Landau coherence length near T_c for a dirty superconductor such as our films is given by [109]:

$$\xi(t) = 0.855\sqrt{\frac{\xi_0 l}{t}}, \tag{5.19}$$

where ξ_0 is the Pippard coherence length, which for niobium is 38.9 nm [110]. In the above equation, $t = 1 - T/T_c$ is the reduced temperature and l is the electron mean free path. The electron mean free path can be calculated by assuming that the product $\rho_n l$ remains unchanged upon adding the impurities, ρ_n being the residual resistivity, that is, the resistivity just above T_c. For niobium $\rho_n l = 3.75 \times 10^{-16}\ \Omega\ \mathrm{m}^2$ [111]. From our measurements $\rho_n = 6.7 \mu\Omega$ cm, so we estimate the electron mean free path to be $l = 5.4$ nm for our films near the transition temperature. At the freezing-out temperature T_f, below which vortices become pinned, we estimated a coherence length $\xi = 320$ nm, by taking 38.9 nm for ξ_0 in Eq. 5.19.

Another parameter used in our calculations is the Ginzburg-Landau parameter $\kappa = \lambda/\xi$. The impurity dependence of κ can be estimated based on the Gor'kov-Goodman relation [112]:

$$\kappa = \kappa_0 + 2.37 \times 10^6 \gamma^{1/2} \rho_n, \tag{5.20}$$

where $\kappa_0 = 0.713$ is the Ginzburg-Landau parameter for a clean niobium film and $\gamma = 720\ \mathrm{J/K^2m^3}$ [110] is the Sommerfeld constant, the coefficient of the linear temperature dependence of the electronic specific heat just above T_c. Thus, using ρ_n from our measurements we find that the Ginzburg-Landau parameter for our films is $\kappa \approx 5.0$. We note that, though in the clean limit niobium has $\kappa_0 = 0.713$, which is just above the limiting value ($1/\sqrt{2} = 0.707$) for type-II superconductors, in our case, where the films are not clean, the Ginzburg-Landau parameter is $\kappa \approx 5.0$. This allows us to use the London approximation for type-II superconductors, which is valid for $\kappa \gg 1/\sqrt{2}$.

Magnetic Strip Images. In order to investigate the critical field at which vortices are completely expelled from narrow thin-film niobium strips we imaged the magnetic field profile above the strips by using our low-temperature scanning Hall probe microscope. The wide-field scanning allows us to image many vortices and

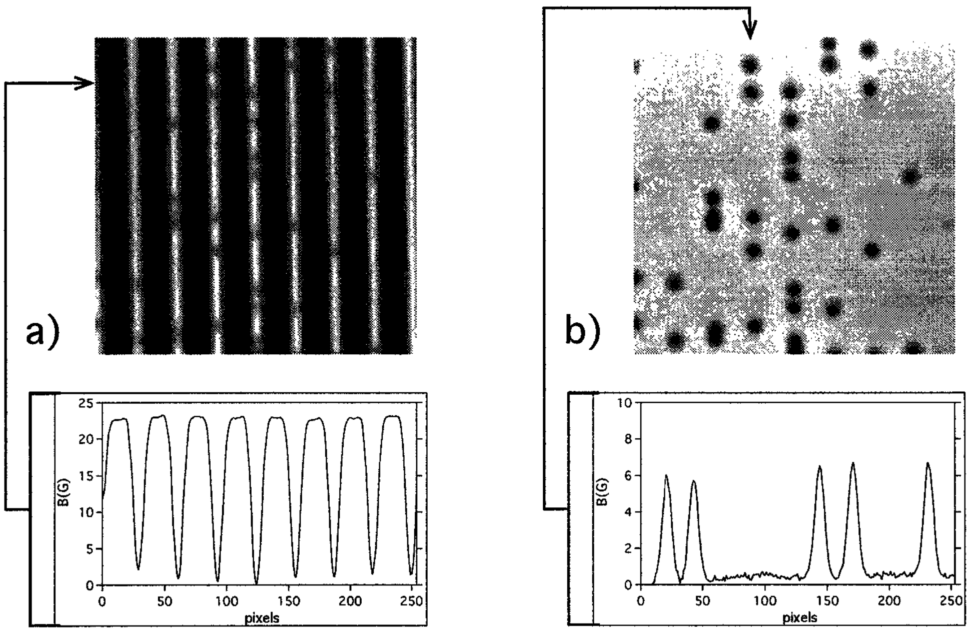

Figure 5.10: Vortices in 1.6 μm strips after field-cooling to 7.0 K in a field of 23 G. In a) the applied field is on whereas in b) the applied field was removed right after the scanning presented in a). In the lower insets is shown the field modulation along the direction indicated by the arrow: a) modulation due to Meissner currents; b) modulation due to vortices.

thus get good counting statistics of the vortex configurations at different applied magnetic fields. The vortex density was determined by applying a magnetic field B and then cooling the strips through T_c to 7.0 K where the SHM images were taken. Though we make the vortex imaging at low temperatures as 7.0 K, we are actually imaging the configuration at T_f when the vortices become frozen. Also, because the penetration depth λ decreases with the decrease of temperature, vortices "shrink" at low temperatures and this improves the resolution of the magnetic images.

In Figs. 5.10, 5.11, and 5.12 we present images for each width (1.6, 10, and 100 μm), respectively, at several magnetic fields. For the narrowest strips, 1.6 μm

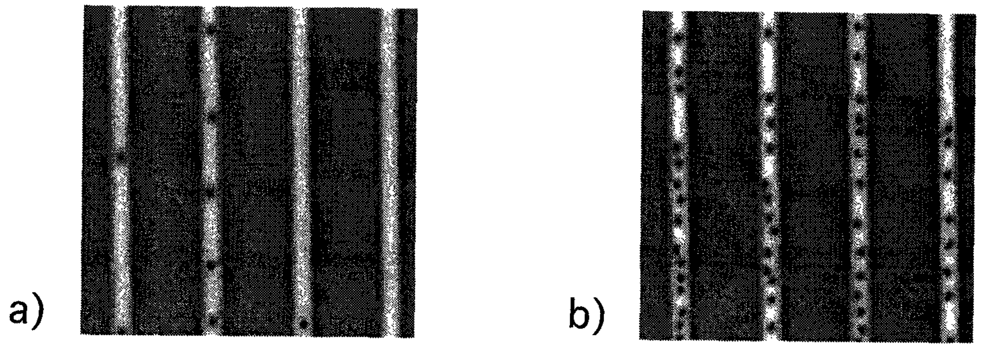

Figure 5.11: Vortices in 10 μm strips after field-cooling to 7.0 K in a field of a) 670 mG and b) 840 mG

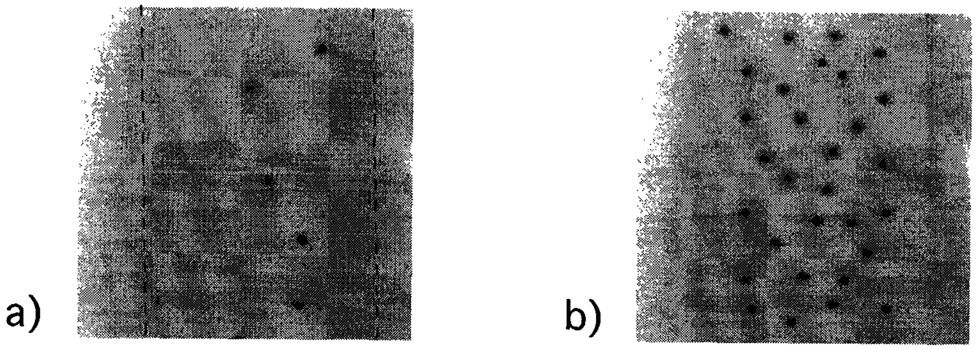

Figure 5.12: Vortices in 100 μm strips after field-cooling to 7.0 K in a field of a) 12.5 mG and b) 53.8 mG. In a) the field modulation is too weak to make the strip's edges visible so we marked them by dashed lines.

(Fig. 5.10), we show vortices in an applied magnetic field of 23 G. The vortices are faint in Fig. 5.10a because, when the field is on, there is a large modulation in the magnetic image due to the difference between the applied field outside the strips (black areas) and the Meissner-screened areas over the strips (light areas). If we remove the field (Fig. 5.10b), the vortices remain frozen in position at this low temperature where the image was taken. But now we can not see the strips any more because in zero field there is no Meissner screening. In the bottom panels of Fig. 5.10 we have the field modulation along the lines indicated by the arrow.

For 10 μm strips (Fig. 5.11), the applied field at which vortices first occur is much lower, about 650 mG. This means that when vortices first appear the Meissner screening is much weaker than for the 1.6 μm strips. Now, the vortices stand out sharply even with the field on.

In the images of 100 μm strips (Fig. 5.12) we can see vortices at even lower magnetic fields (of order of mG). At very low fields (Fig. 5.12a) vortices tend to lie along the middle line of the strip where their energy is the lowest. However, some vortices are pinned away from the center because niobium films are strong-pinning materials. At higher fields (Fig. 5.12b), vortices start to spread out over the whole width of the strip because of intervortex repelling interactions and form a lattice. Because the strip is so wide, we can image only one strip at a time.

The estimate for the highest critical field for complete vortex expulsion was done by imaging the strips at many applied magnetic fields. In this way, the critical

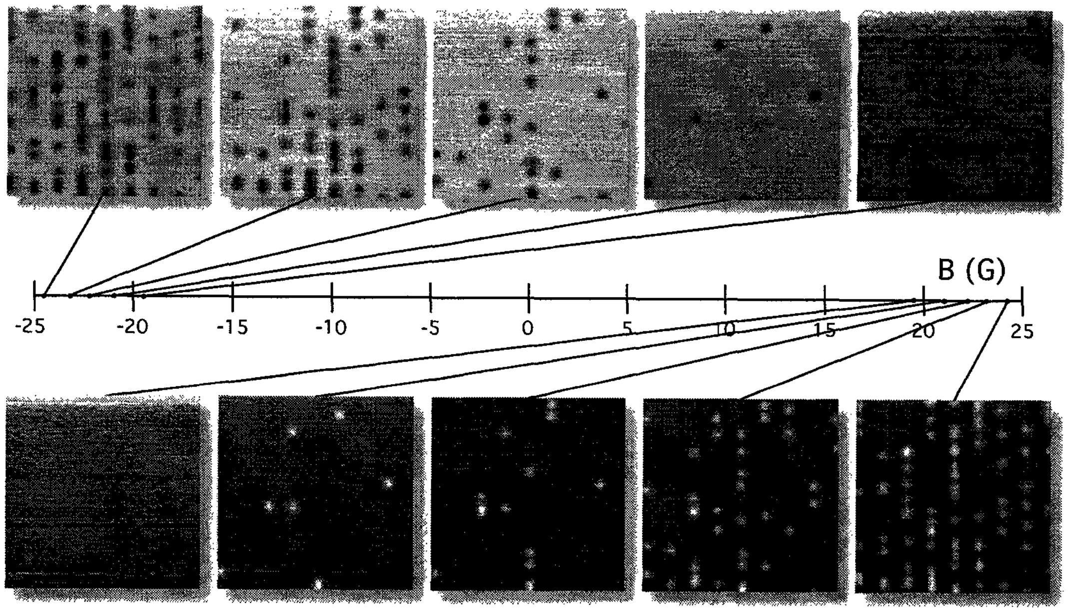

Figure 5.13: Vortices in 1.6 μm strips. At each given field, we first field-cooled the strips to 7.0 K, removed the field, and then took the image.

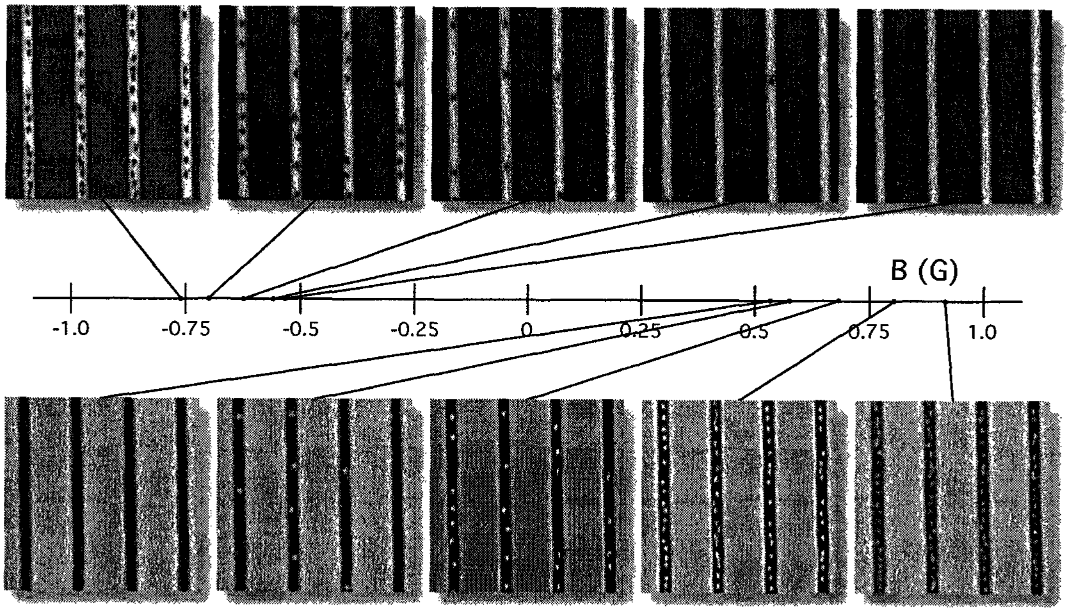

Figure 5.14: Vortices in 10 μm strips. At each given field, the strips have been first field-cooled to 7.0 K, and then imaged.

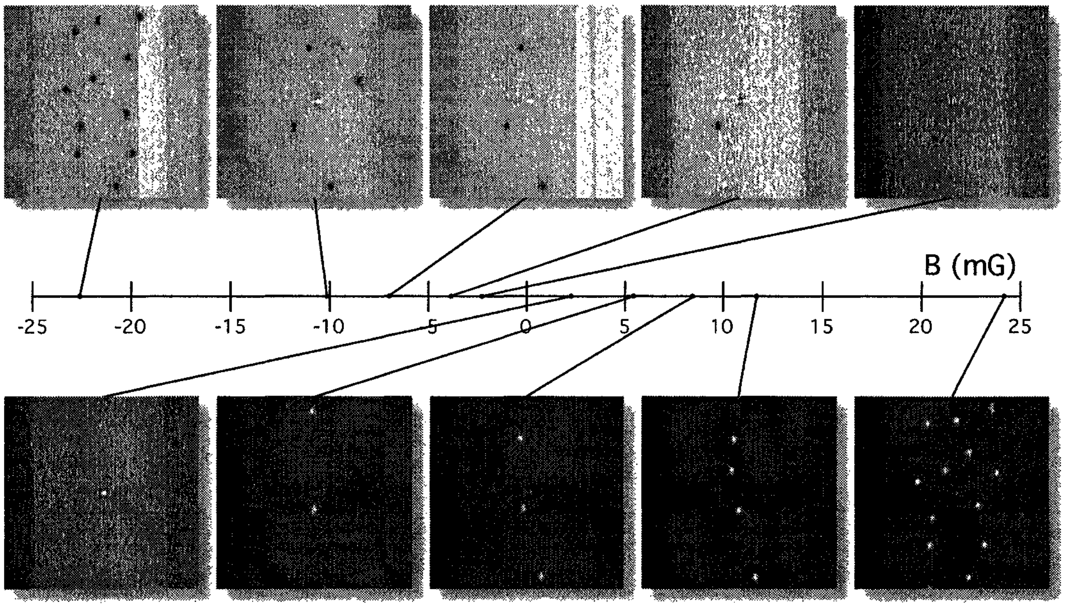

Figure 5.15: Vortices in a 100 μm strip. At each given field, the strip has been first field-cooled to 7.0 K, and then imaged.

field will be the magnetic field below which there are no more vortices present in the strip. In Figs. 5.13, 5.14, and 5.15 we show images of vortices in 1.6, 10, and 100 μm strips, respectively, at several negative and positive magnetic fields. At each given field, the strips have been first field-cooled to 7.0 K, and then imaged. The images shown in Figs. 5.13, 5.14, and 5.15 don't have the same contrast since they were not made at the same height above the sample's surface. This is because scanning many times over a large area, we have to readjust from time to time the height at which the scan is made. For each width we found a field range centered about zero for which all vortices are expelled from the strip. By counting how many vortices are present in each image we get the field dependence of the vortex density for each width (see Fig. 5.16).

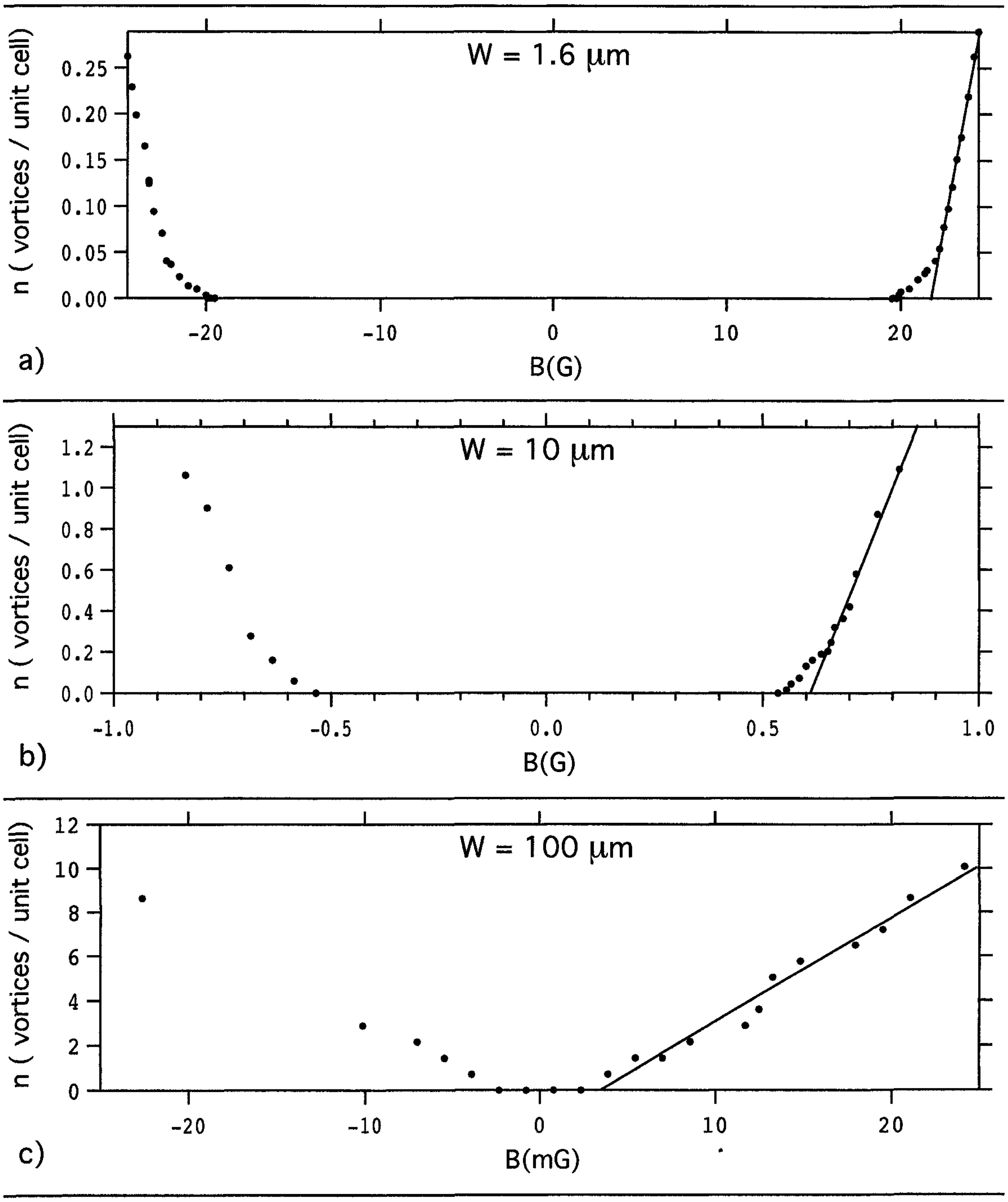

Figure 5.16: The field dependence of the vortex density for each studied width.

Experimentally-Determined Critical Field. We determined the lower critical field for each width from the plot of the vortex density versus the applied magnetic field. The vortex density n was calculated from the number of vortices N per image in the following way. First, the effective imaged area $A = L \times W$ was divided into unit cells of area W^2, L and W being the total length and the width of the strip. Then, the vortex density was defined as the number of vortices per unit cell, $n = N/(A/W^2)$. In Fig. 5.16 we show the vortex density n versus the applied field B. We consider a linear fit for the field dependence of the vortex density

$$n = a + bB = b(B + \frac{a}{b}), \tag{5.21}$$

where a and b are fitting parameters. These parameters have the following physical meaning. First, because the flux penetrates inside in form of vortices, the parameter b will be related to the ratio of the flux per unit cell and the flux quantum Φ_0. Second, the ratio b/a gives the magnetic field at which the vortex density is zero. With these considerations, the above fitting equation was rewritten as

$$n = (B - B_m)W^2/\Phi_0^\star, \tag{5.22}$$

where B_m and $\Phi_0^\star$ are now the fitting parameters. By extrapolating this linear dependence of n down to $n = 0$ we find B_m which is defined as the maximum field for the complete vortex expulsion. From the slope we find $\Phi_0^\star$, which can be compared to the flux quantum Φ_0. The fitting lines are also shown in Fig. 5.16 for each strip.

We note in Fig. 5.16 that at fields slightly less than B_m there is a region

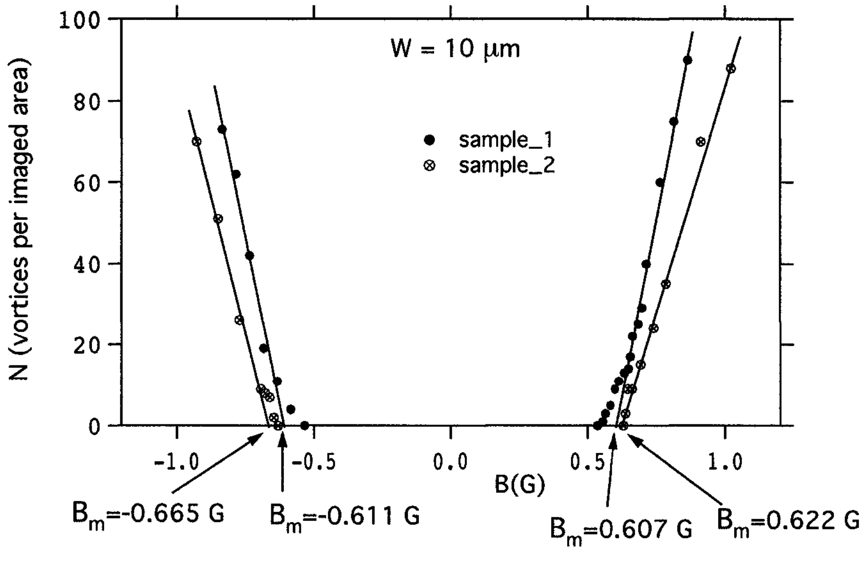

Figure 5.17: The determination of the critical field B_m from scanning over two different samples with 10 μm strips.The results for sample_1 are also shown in Fig. 5.16b.

width (μm)	B_m (G)
1.6	21.7
10	0.62 ± 0.03
100	0.003

Table 5.1: Critical field for complete vortex expulsion.

(especially for narrower strips) where the slope of the linear dependence is reduced. We will later explain this shoulder in terms of the inherent pinning of niobium films.

To see if our measurements are affected by errors we repeated the experiment for the 10 μ strip several times on different samples. Possible sources of errors could be represented by pinning distribution over strip area and edge defects introduced by fabrication. In Fig. 5.17 we present the results from scanning over two different samples patterned with 10 μm strips. We chose to plot here the actual number of vortices N from the scanned area rather than the vortex density as in Fig. 5.16. The number of vortices N is given by

$$N = (B - B_m)A/\Phi_0^\star, \tag{5.23}$$

where A is the effective scanned area, and B_m and $\Phi_0^\star$ are the same fitting parameters as in Eq. 5.22. The fitting lines given by Eq. 5.23 are also shown in Fig. 5.17.

As can be seen from Eq. 5.23, the determination of the critical field B_m comes from the ratio of the y-intercept and the slope. Though we don't need to use the value of W in calculating this ratio, the critical field B_m has an intrinsic dependence of W. We stress here that the critical field B_m is determined only by the width of the strip and is not affected by the particular pinning landscape over the imaged area and the detail fabrication structures along the strip edges. From these fits the critical field B_m for the 10 μ strip was found to be 0.6 ± 0.03 G. This means that the error in determination of the critical field B_m is not bigger than 5 percent. We assume that uncertainties in determination of the critical field for the other two strips, 1.6 and 100 μm are of the same order of magnitude. The slope of the fitting line is related to the vortex nucleation in fields above the critical field and this can depend on pinning and edge structures which are characteristic for each sample. For the measurements shown in Fig. 5.17, we found the slope parameter $\Phi_0^\star = 1 \pm 0.2\Phi_0$, which means that the error is 20 percent. Thus, we see that, for different samples, the slope of the fitting line shows larger variations than those of B_m.

Our experimentally-determined data points B_m for the three studied widths (Table 5.1) are plotted along with the theoretical curves for B_0 and B_s [95, 96] in Fig. 5.18. On this log-log plot the errors due to the measurement of the freeze-out temperature and determination of B_m are insignificant small than the point size. As can be seen, the strong width dependence $B_m \approx \Phi_0/W^2$ is revealed in this range of strip widths. The prediction of B_0 is consistently below our data, which supports the argument that a metastable minimum in the Gibbs free energy cannot hold in vortices; to do so, a deeper minimum and hence higher field is required. Thus, the experimental results support the physical argument that the relevant critical field for complete vortex expulsion is not B_0, but B_s, the field for which the Gibbs free energy reaches zero in the middle of the strip.

We see in Fig. 5.18 that the theoretical curve B_s matches the determined critical field for the 10 μm strip fairly well, but there is not a good agreement for 1.6 and 100 μm strips. There are several reasons for this.

First, we note that the theoretical assumption $\xi < W \ll \lambda_\perp$ is well satisfied only for the intermediate width ($W = 10$ μm). For the narrowest strip, ξ/W is about 0.2 at the freeze-out temperature T_f. In this case, the size of the vortex core becomes comparable to the sample size and, consequently, the London model used in the theoretical models ceases to be well satisfied. The London model assumes that the magnetic penetration depth is much larger than the coherence length, in which case the order parameter is constant outside the vortex core and the vortex core is

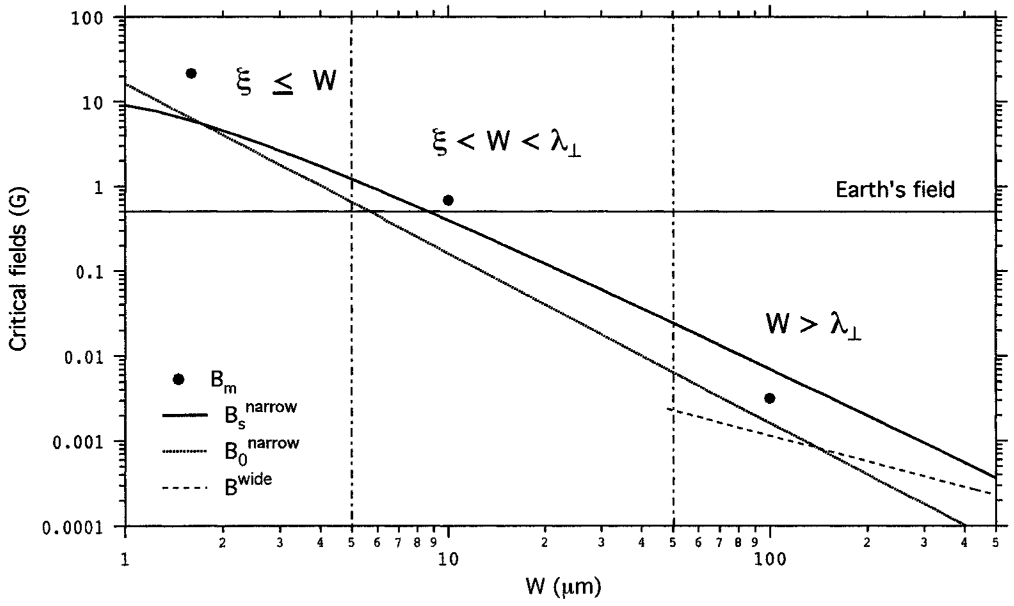

Figure 5.18: The lower critical fields as a function of the strip's width. Narrow strip behavior, $\xi < W < \lambda_\perp$, applies to strips with widths approximately in the range delimited by the vertical lines.

a one-dimensional hard cylinder parallel to the magnetic field. Obviously, such an approximation cannot be satisfied in samples of size comparable to the size of the vortex core. Indeed, as can be seen from Fig. 5.18, for widths less than 1.4 μm, B_s becomes less than B_0. This doesn't make physical sense because B_0 (the lowest field where the Gibbs free energy has its first minimum) must be always lower than B_s (the field where the Gibbs free energy is zero in the middle of the strip). A more complete theory for narrow strips should include a correct Ginzburg-Landau treatment for the vortex core.

At the other extreme, the 100 μm width does not really satisfy the assumption $\lambda_\perp \gg W$ because at the freeze-out temperature $\lambda_\perp = 24$ μm, which is less than

W. In Fig. 5.18, the dashed curve is calculated in the framework of a wide strip model [113]. We can see that our experimental point for the 100 μm strip is between the theoretical curves for narrow and wide strips. It is probably correct to assume a wide strip behavior for widths larger than about 300 μm.

Vortex Density. As was mentioned before, except for the knee due to pinning, we interpreted the field dependence of the vortex density as a linear function for each of the studied widths (Fig. 5.16). In each case, the measured slope of the fitting line, dn/dB, was quite close to the value of W^2/Φ_0. In Fig. 5.16, the slope $W^2/\Phi_0^\star$ was determined to be 0.10, 5.25, and 0.47 G^{-1} for the 1.6, 10, and 100 μm strips. Consequently, the fitting parameter $\Phi_0^\star$ was estimated to be 1.21, 0.85, and 1.00 Φ_0, respectively. This tells us that the entire magnetic flux through the strip above T_c nucleates into vortex lines below T_c. The result is perhaps surprising because it might seem that the shape of $G(x)$ would confine the vortices towards the strips' centers. With such a small effective width for vortices, it would seem more likely that the slope be rather less than W^2/Φ_0. On the other hand, this result shows that the demagnetization effects are negligible in the case of our narrow strips.

Though the linear fits look quite good, we need to understand what determines $n(B)$ once the vortices start to enter the strip. Let's begin by discussing how vortices penetrate into a *bulk* superconductor as the field is increased. In Fig. 5.19 is shown the internal field B_{in} as a function of the applied field B for a niobium bulk superconductor. The plot was reconstructed from magnetization measurements [110].

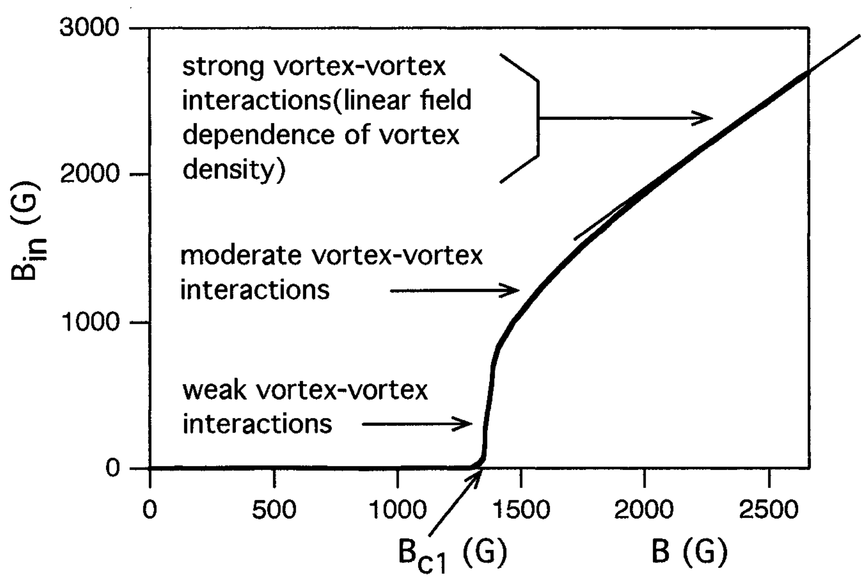

Figure 5.19: The internal field of a niobium bulk superconductor as a function of the applied field (calculated from [110]). The plot gives the actual field dependence of the vortex density.

Because in the mixed state the entire flux inside is in the form of vortices the internal field B_{in} is proportional to the vortex density.

Theoretically it can be shown [91] that in bulk superconducting samples the vortex density at fields just above B_{c1} increases very rapidly as the applied field is raised, as shown in Fig. 5.19. This is because the vortex-vortex interactions are exponentially weak until the vortices come within $\sim \lambda$ of each other. Consequently, at fields just slightly larger than B_{c1}, it is possible to form many vortices without any significant interaction energy cost. Thus, at these low fields, the vortex density increases almost vertically. Only the inherent pinning prevents the slope of the vortex density versus field, dn/dB, from being theoretically infinite at B_{c1}. At higher fields, when vortices start to interact each other, the vortex density shows a nonlinear behavior as a function of the applied magnetic field. This is the region of moderate vortex-vortex interactions in Fig. 5.19. At even larger fields, the field dependence of vortex density becomes almost linear; it is called the strong vortex-vortex interaction region in Fig. 5.19.

One result of our experiment is the field dependence of the vortex density in narrow thin-film strips at fields above the lower critical field. This was shown in Fig. 5.16. The dynamics of vortex nucleation in narrow strips is similar to the bulk one, which was described above. However, in the case of the strips, the vortex-vortex interactions become significant only when vortices come within W, not λ, of each other. This is why we chose to calculate the vortex density n as the number of vortices per unit cell of area W^2. Therefore, we expect that at fields just above B_m, the vortex density will increase very rapidly before reaching 1. After that, the vortex density as a function of field should exhibit a slower increase which, presumably, becomes linear at fields much larger than B_m.

Let's see now if the vortex density follows this general behavior in our case of narrow strips. For the 1.6 μm strip it was possible to investigate the field dependence of the vortex density only for n less than 0.25 (see Fig. 5.16). At fields just above B_m the initial steep rise of the vortex density is masked by the pinning contribution. As the field is increased we expect to see a curvature in the field dependence of the vortex density similar to that of the moderate vortex-vortex interaction region in

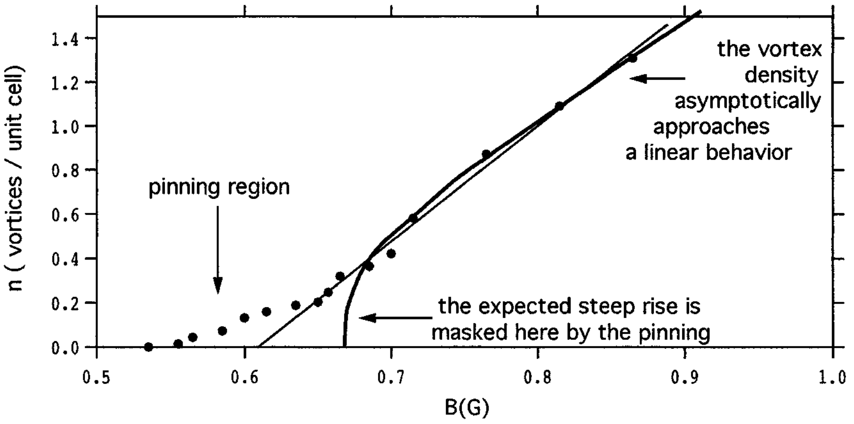

Figure 5.20: Field dependence of the vortex density for the 10 μm strip. The thin line is the linear fit considered previously whereas the thick curve is a more realistic fit at fields above the lower critical field.

Fig. 5.19. However, the vortex density for our 1.6 μm strip exhibits a quite linear field dependence in this region. This behavior is difficult to understand, and currently we don't have a good explanation for this. In Fig. 5.16b for the 10 μm strips, the vortex density n goes to values around 1. A much more detailed picture of this is shown in Fig. 5.20, where we consider only the positive fields from Fig 5.16b. We can see that the initial rise at low fields is still masked by the pinning contribution. At moderately-large fields where the vortex-vortex interaction come into play, the field dependence of the vortex density was considered previously as being linear. However, we can see better in Fig. 5.20 that only at higher fields does the vortex density approach a linear behavior. The very linear region that should be observed at large fields was not covered in our measurements. For the 100 μm strip, the vortex density in Fig. 5.16c is almost entirely in the linear region of fields much larger than B_m, and

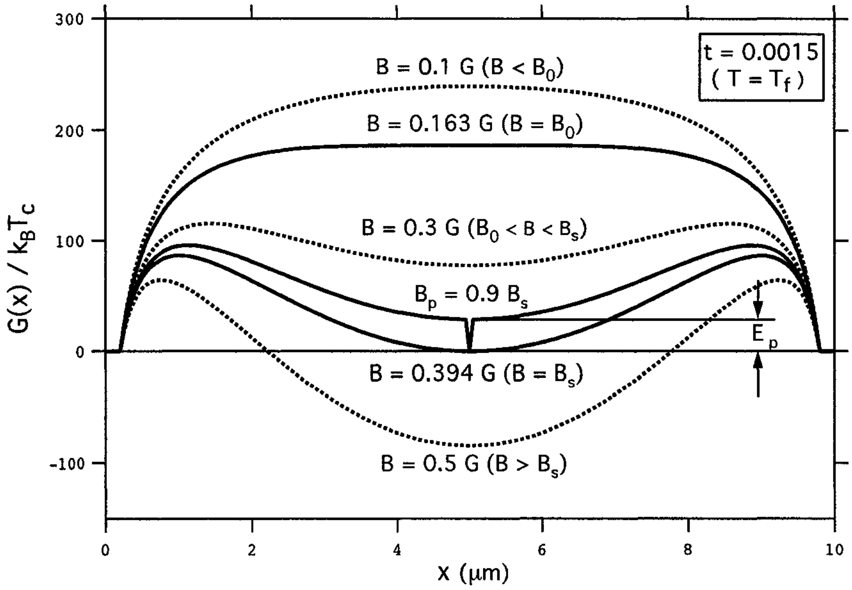

Figure 5.21: With pinning vortices will penetrate inside at lower fields than when no pinning is present.

the initial step, if present, is too small to be observed.

Pinning Contributions. As was mentioned before, at fields less than the determined critical fields we observe a knee in the field dependence of the vortex density n (Fig. 5.16). This region can be explained by effects of pinning. Pinning sites can be represented schematically as narrow deep potential wells which locally lower the Gibbs free energy. Thus the Gibbs free energy $G(x)$ reaches zero, implying a stable state for a vortex, at fields lower than if no pinning is present. Thus, vortices can remain trapped in the strip at lower fields than they could with no pinning. Qualitatively (Fig. 5.21), as the field is increased from B_p, where the first vortex enters the pinning well, to B_s, where vortices would have first entered with no pinning, the free energy changes by an amount $\Delta G = E_p$, where E_p is the pinning well depth.

The difference $\Delta B = B_s - B_p$ between the critical field with no pinning (from the extrapolation of the linear regime to $n = 0$) and the field where the first vortex enters (in the presence of pinning) is

$$\Delta B/B_s \approx \frac{1}{B_s}\frac{\Delta G}{\partial G/\partial B} \approx \frac{1}{B_s}\frac{E_p}{\partial G/\partial B} = \frac{8\pi^2\lambda_\perp}{\Phi_0^2\ln(2W/\pi\xi)}E_p. \tag{5.24}$$

In the above equation, we used Eq. 5.16 for B_s, and the slope $\partial G/\partial B$, calculated in the middle of the strip, can be found from Eq. 5.15 as

$$\partial G/\partial B\,|_{x=W/2} = \frac{\Phi_0 W^2}{16\pi\lambda_\perp}. \tag{5.25}$$

Equation 5.24 predicts, within logarithmic accuracy, that the ratio $\Delta B/B_s$ of the pinning region is independent of width. From our measurements we find that $\Delta B/B_s = 0.09$ for the 1.6 μm wide strip, and 0.10 for the 10 μm strips. For the 100 μm strip a 10 percent difference between B_m and B_p would be too small to be observed (see Fig. 5.16c). With $\Delta B/B_s \cong 0.1$ and using Eq. 5.24 we have estimated a pinning energy $E_p \approx 30\ \mathrm{k_B}T_f$.

On the other hand, if we look at the vortex depinning as a thermally activated process, this will be described, for temperatures above T_f, by the rate

$$R = \omega_0 \mathrm{e}^{-E_p(T)/\mathrm{k_B}T}, \tag{5.26}$$

where ω_0 is the attempt escaping frequency of a vortex from a pinning center, unknown in general, but assumed to be in the range MHz to THz. If we consider that vortices freeze-out at T_f when the rate R becomes as small as 0.001Hz, we have an estimation of the pinning energy E_p in the range 20–30 $k_B T_f$, in good agreement with the above estimation.

5.5 Conclusions

In conclusion, we have used scanning Hall probe microscopy to investigate the dynamics of vortex nucleation in narrow thin-film superconducting strips. One major result of this experiment is the measurement of the maximum critical field at which vortices are completely expelled from such narrow thin-film strips. We have established that the first flux penetration into the strip occurs when the vortex is absolutely stable in the center of the strip. This state is realized when the Gibbs free energy reaches zero in the middle of the strip. Further, we find that the measured maximum critical field varies as $B_m \approx \Phi_0/W^2$, in general agreement with theoretical predictions.

However, although the overall $\sim 1/W^2$ dependence has been verified, there are clear differences between our data and the theoretical predictions for the narrowest strip ($W = 1.6$ μm) and the widest ($W = 100$ μm). We obtain a good match for the intermediate width ($W = 10$ μm). This is because a strip is called narrow when its width satisfies the condition $\xi < W \ll \lambda_\perp$. From our measurements we concluded that this condition is for widths in the range 5 – 15 μm.

Scanning over a large area allowed us to measure the vortex density at low applied magnetic fields. We observed that the vortex density is quite linear with the applied magnetic field for fields just above the lower critical field. From the slope of this linear dependence we find that the total flux through the strip nucleates entirely into vortices.

At fields just below the measured lower critical field we still observed the presence of vortices. This was explained in terms of the inherent pinning of niobium films. A quantitative comparison between the measured values of applied fields where vortices are observed (due to pinning) and theoretical predictions (considering pinning) shows good agreement. We estimated a pinning energy for niobium films to be about $E_p \approx 30\ \mathrm{k_B} T_c$.

From a practical standpoint the conclusion of this experiment is that superconducting devices should be designed with narrow wires to eliminate vortices and the noise determined by their presence. For example, to exclude vortices from superconducting lines operating in the Earth's magnetic field of 0.5 G we need only to use lines of width less than 10 μm.

The $\sim 1/W^2$ dependence of the critical field on the strip width should be quite general, being valid not only for the niobium strips studied here, but for all type-II materials. High-κ materials like NbN or HTS materials would be especially interesting, since their small ξ would extend the region of width for which the strips can be called narrow. A quite interesting case would be that of amorphous thin films such as MoGe, MoSi or α-Al which are high-κ and very weak-pinning materials. In low pinning materials, the knee observed at low fields in our measurements will be suppressed and this will make easier the identification of the critical field for complete vortex expulsion. However, the pinning of these materials is so weak that vortices might remain mobile at low temperatures, significantly below T_c, where the effective penetration depth $\lambda_\perp$ is smaller than the strip's width, and the theoretical model for the case $\lambda_\perp \gg W$ is no longer valid.

Chapter 6

The Superconducting Dripping Faucet

Over the last several years significant progress has been made towards a better understanding of the complex dynamics of vortex matter in superconducting films. Not only the very interesting physics involved motivates this effort [40, 114, 41] but it appears that concrete applications could be based on confined vortex assemblies in low dimensional superconductors [58, 59, 115]. In such systems it is desired to manipulate and control the motion of the magnetic flux quanta along nano-engineered patterns. Substantial advances have been made in controlling vortices in two-dimensional (2D) submicron-modulated superconducting films [44, 59, 116] and mesoscopic channels [54, 56]. As part of superconducting devices, a further advance would be to design one-dimensional (1D) channels confining vortex assemblies [89, 117]. By reducing the dimensionality, we can obtain a direct understanding of the dynamics of individual flux entities (such as vortices) which would otherwise be difficult to reveal in a system with many more degree of freedom. However, since they carry only a small amount of flux ($\Phi_0 = 2.07 \times 10^{-7}$ G cm^2), discrete vortices are difficult to be independently monitor even when their motion is confined to a 1D channel. Thus, for instance, only 1 μV will be generated by a periodic chain of vortices flowing in a 1D channel at a frequency of 500 MHz. At this high speed, the dynamics is far too fast for the direct observation of individual moving vortices.

A much easier detection of flux is possible in the case of *multiquanta flux tubes* moving along a constriction fabricated in a type-I superconducting film. Each flux tube carries about 100 flux quanta Φ_0, so their signal is much larger. Further, the same 1 μV will be generated now at a frequency 100 times lower than in the case of vortices. It was demonstrated [118, 119, 26] that the dynamics of flux structures in both type-I (flux tubes) and type-II (vortices) superconducting microbridges exhibit similar characteristics, with both verifying a Josephson-type relation in the periodic flow regime. Consequently, we can achieve valuable information about the dynamics of vortices flowing in a 1D channel by doing similar—but much easier—experiments on flux tubes.

In microbridged configurations the current-driven dynamics of flux tubes is a complex and not yet very well understood process. Earlier work on constricted films of type-I superconductors using either stroboscopic magnetooptical flux detection [26] or time-resolved measurements of the flux-flow voltage [27] didn't explore in detail the entire dynamics of current-driven flux tubes, their analysis being restricted only to a particular highly periodic flux flow regime. The reason of this limitation is that the experiments were made either by correlating the flux detection to the driving current or averaging repetitive records.

To investigate the entire dynamics we need an experiment that allows a direct detection of individual flux tubes flowing along a 1D channel, independent of whether their motion is periodic or not . To do this, we have developed a novel high-bandwidth Hall probe to detect the nucleation and subsequent motion of the magnetic flux tubes along a fabricated 1D channel in a led film. We find that the dynamics of current-driven flux tubes share many characteristics of the well-known dripping water faucet experiment [120], so our experiment is a kind of "superconducting dripping faucet." Analysis of the times between successive flux tubes reveals high complex behavior, with regions of periodic, multiply-periodic, and chaotic behavior as the control system parameter (driving current) is varied.

In Section 6.1 we review dripping water faucet experiments, which can provide us with insights into the dynamics of the current-driven flux tubes. In Section 6.2 we discuss previous experiments made by other researchers concerning the dynamics of flux-tube flow in the current-induced resistive state of a type-I superconducting microbridge. Our experiment was developed on the basis of these observations. The detailed experimental arrangement that we developed to detect the motion of flux tubes along a 1D channel in a type-I superconducting strip is described in Section 6.3. In Section 6.4 we describe the technique employed to fabricate a microbridged constriction in a lead strip. This provides us the 1D channel along which the flux tube motion is studied. The observed dynamics of the "superconducting dripping faucet" is presented in Section 6.5. In Section 6.6 we introduce the general concepts of nonlinear time series analysis, which we use to investigate the complex dynamics exhibited by our system. Finally, we propose in Section 6.7 a model for current-driven flux tubes flowing along a 1D channel, which explains many aspects of the observed dynamics.

6.1 Dripping Faucet Experiment

The dripping faucet experiment is perhaps the canonical system illustrating basic phenomenological ideas of chaotic systems. Chaos here denotes not a completely random process but stochastic behavior occurring in deterministic systems. Therefore it is possible to observe some specific pattern in the underlaying dynamics developed by the system. It is well known that in a chaotic system a prediction can not be made for a long period but only for short developments.

The dripping faucet experiment was first carried out by Shaw in 1984 [120]. Since then, substantial work has been devoted to investigating the dynamics of the dripping faucet both experimentally [121, 122, 123, 124, 125, 126] and theoretically [127, 128, 129, 130, 131, 132].

Briefly, a water faucet or nozzle is turned on just enough for it to start dripping. At low rates, the drops detach periodically from the nozzle. If we increase slowly the rate, which is here the control parameter, the time intervals T_n between successive drops show periodicity (Fig. 6.1a), period-doubling (Fig. 6.1b), intermittency, and

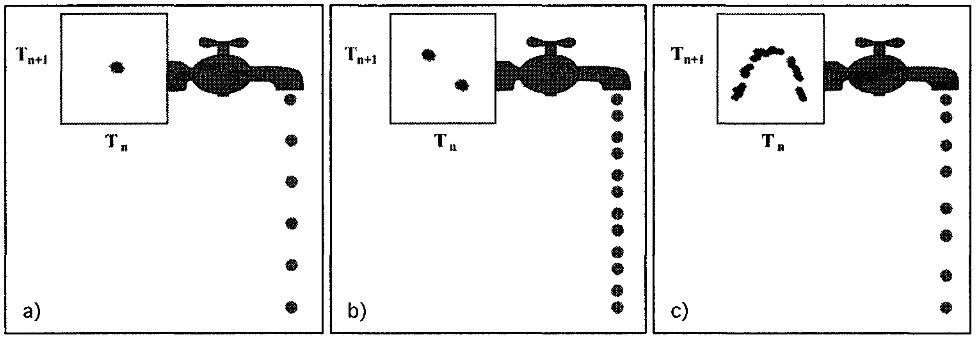

Figure 6.1: Different dripping regimes of the faucet: a) periodic; b) double-periodic; c) chaotic. The insets show the first return map for each regime.

eventually chaos (Fig. 6.1c). In the insets of Fig. 6.1 is shown also the first-return map for each regime; they are obtained by plotting each time interval versus the previous one. These give a compact picture of the temporal history of each different regime. Another important way to display the drip times is to plot *bifurcation maps* (or *diagrams*) which show the dripping interval as a function of the flow rate (control parameter). In Fig. 6.2 are shown two bifurcation maps for a dripping faucet: a) is from a dripping faucet modeled as the one-dimensional motion of a variable mass attached to a spring, and subjected to the gravitational force and a frictional force proportional to the speed of the growing droplet [128]; b) is from an experiment [122].

The breakup of a droplet from the faucet neck occurs through two successive events, the *necking* and *oscillating* processes. At a given flow rate the water builds up until the drop, subject to its weight and the attractive force of molecules, reaches a threshold point at which it detaches from the neck. After that, the remaining liquid

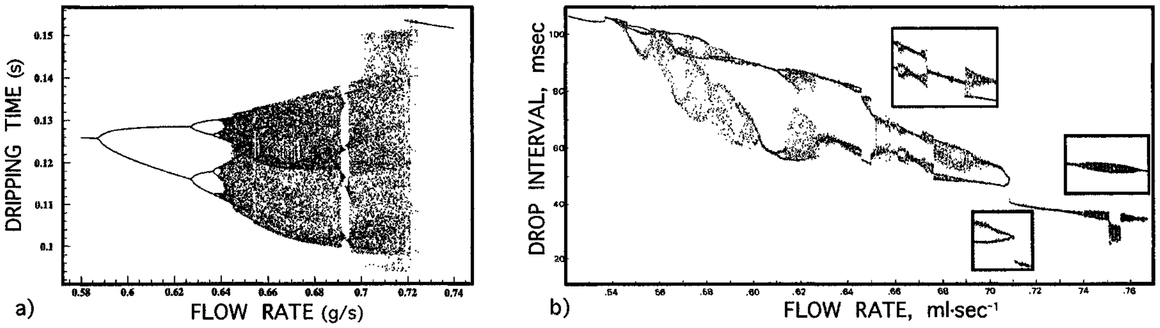

Figure 6.2: Bifurcation map of the dripping faucet dynamics: a) modeling [128]; b) experiment [122].

recoils due to capillary forces, and undergoes damped oscillations as it grows into the next drop. These residual oscillations in the growing drop determine the time of the next drop formation in a highly nonlinear way. The time intervals between successive drops falling can thus become irregular or chaotic at certain values of the flow rate.

It is plausible that similar mechanisms could be responsible for other nucleation processes. In Fig. 6.3 is shown a stroboscopic magneto-optical detection of flux tube nucleation along a fabricated channel in a lead strip [26]. The flux nucleation was induced by applying a driving current along the strip (perpendicular to the channel). If we look at Fig. 6.1 and Fig. 6.3 we may wonder if the underlying dynamics has something in common in both cases, though the systems are nominally quite different. In both experiments we have individual driven entities, which are either water droplets (water experiment) and flux "droplets" (superconducting experiment). In both cases the nucleation mechanism consists of *growth* and *detachment* of these entities at the base of a reservoir (the faucet neck and the channel end, respectively). Once the

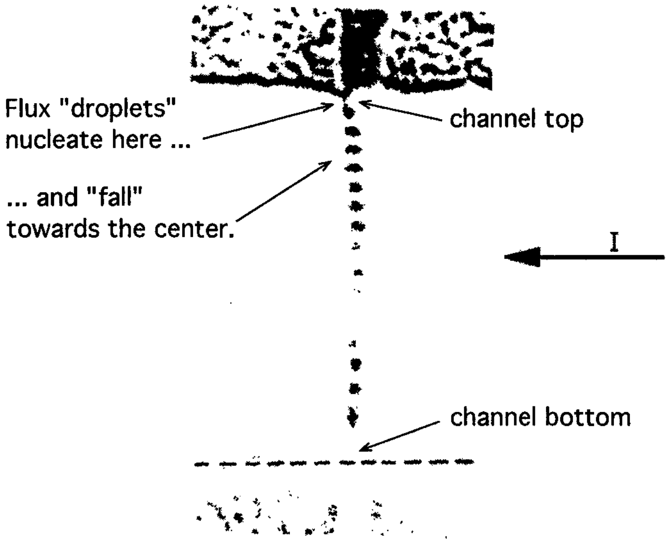

Figure 6.3: Magneto-optical detection of flux tubes flowing along a one dimensional channel [26].

droplets detach, they are pulled down by either gravity or the driving force of the applied current. Finally, as in the dripping water faucet system, each detached flux "droplet" determines the nucleation condition for the next one by modifying the magnetic field at the channel end.

The motivation for our experiment was based on these similarities, and this is why we think of it as a "superconducting dripping faucet." To explore the dynamics of the superconducting system, we have used Hall probe microscopy in novel high-bandwidth mode. This has allowed us to directly observe for the first time the entire dynamics developed by current driven flux tubes flowing along a 1D channel.

6.2 Current-Induced Breakdown of Superconductivity in Type-I Superconducting Strips

In this section we provide a short overview of the current-driven dynamics of flux tubes in type-I superconducting constricted strips. We discuss here the flux penetration in a type-I superconducting microbridge, this being the sample geometry that we used in the "superconducting dripping faucet" experiment.

The first direct observation of the dynamics of flux-tube flow in the current-induced resistive state (CIRS) came from stroboscopic magnetooptical experiments on type-I constricted strips [26, 133, 134]. The constricted geometry (see Fig. 6.4) assumes a locally weakened type-I (lead, indium etc.) strip fabricated in two successive evaporation steps: first, a channel is defined in a first layer and, subsequently, a second overlay strip bridges the channel. The channel width W is actually the length of the bridge (3–10 μm) and the width of the overlay strip dictates the channel length L (hundreds of microns which is much bigger than any characteristic lengths in superconductors). The thickness of the first layer (1–2 μm) determines the thickness modulation of the bridge; it is equal to the difference between the thicknesses of the channel and the thickness of the adjoining regions.

The channel serves two purposes: to localize the flux nucleation and to guide the nucleated tubes. Thus, at sufficiently large currents applied through the strip, so that the magnetic field due to the current exceeds the critical field at the sample's

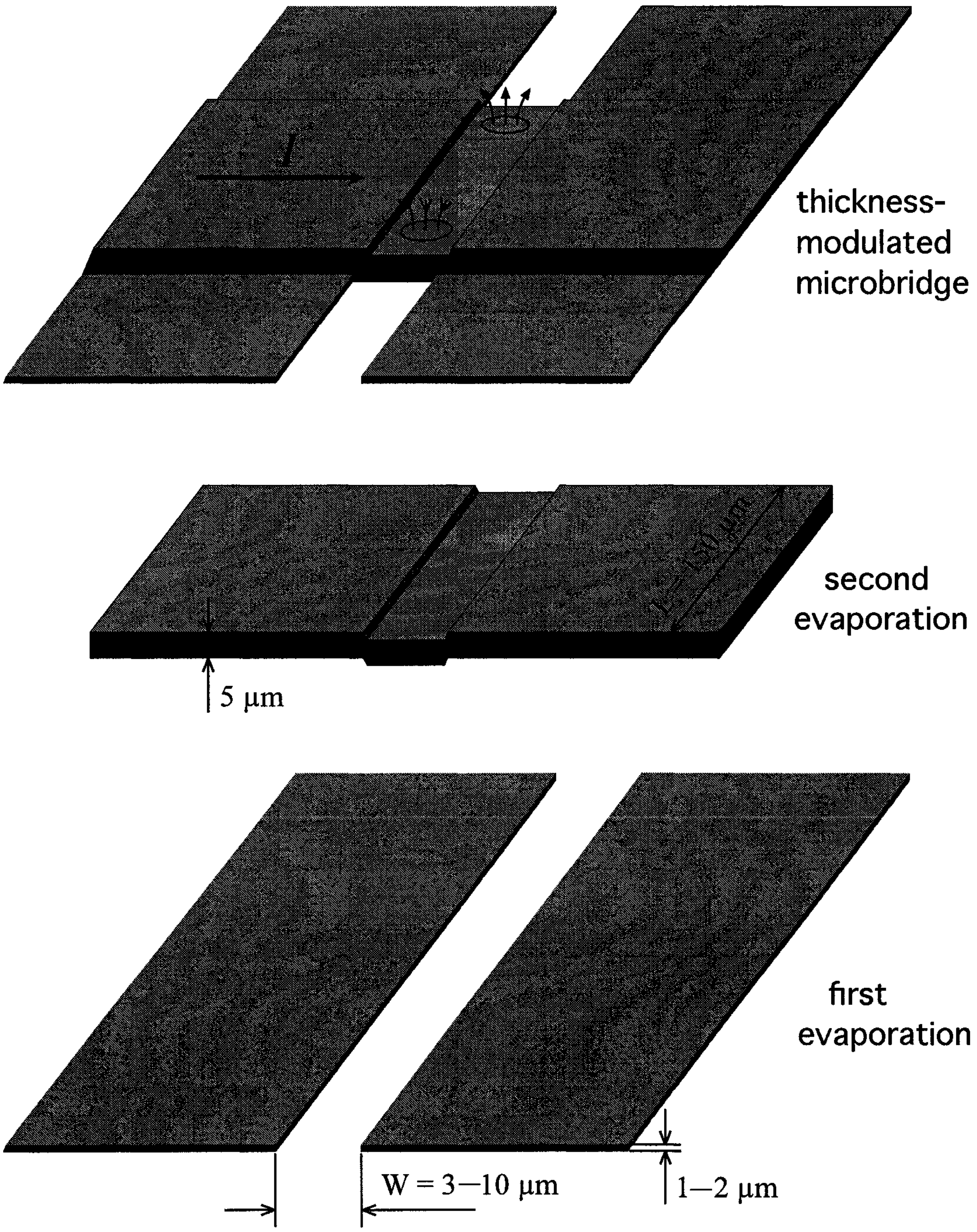

Figure 6.4: The constricted geometry (top) used to study the flux tube-flow along a one dimensional channel is made in two successive evaporations.

edges, flux domains in form of cylindrical tubes nucleate at the edges of the channel. Then, under the influence of the Lorentz force, the nucleated flux tubes move along the channel towards the center where they will be annihilated by flux tubes of opposite sign coming from the other edge.

In stroboscopic magnetooptical experiments, highly periodic flux motion can be studied with very good time resolution (better than 10^{-7}s) by combining stroboscopic illumination with magnetooptical flux detection [26]. The periodicity of flux-tube flow along the constriction is forced by synchronizing the nucleation of flux tubes using an applied ac current superimposed over the dc bias current. The dc current is slightly less than the critical current and thus the sum of the dc plus ac currents becomes, once each period, larger than the critical current. A modulator simultaneously triggers the ac current and an acousto-optical shutter, thus generating short light pulses synchronously with the flux nucleation. By varying the phase between the sample current modulation and the light pulse the entire time evolution during one cycle can be investigated (Fig. 6.3 shows one of these measurements).

In experiments done by Chimenti *et al.* [26], the frequency of ac current was 400 kHz, while the laser pulse width was 250 ns, which means 10 stroboscopic frames per cycle. The current amplitudes could be adjusted in such a way that one, two or three flux tubes were generated per cycle. We stress again that in these kind of experiments, because the perturbation was periodic, the dynamics developed by the flux tubes was forced to be periodic. Chimenti *et al.* [26] estimated the amount of flux per tube to be about 120 Φ_0 in their experiments, with an average flux-flow velocity varying between 400 cm/s (at edge) and 200 cm/s (near to the central part). A flux-flow model describing the observed dynamics of the current-driven flux tubes in this experiment has been subsequently developed [133].

The CIRS was passively (i.e. without an ac trigger) investigated in a constricted indium film strip [135]. In this experiment a high normal-state-resistivity granular aluminum strip of about 4 μm width is used as a magnetoresistive sensor to detect the passage of the flux tubes. At a given current, applied perpendicular to the constriction, the frequency spectrum of the flux motion along the constriction was recorded, rather than individual flux tubes. They found highly periodic flux nucleation for currents belonging to a certain interval. In this case, the rate ν of the flux tube nucleation as a function of sample voltage drop V was found to be a linear Josephson-type relationship,

$$\nu = V/N\Phi_0, \tag{6.1}$$

N being the number of flux quanta per tube (about one hundred in this experiment). However, for current regions adjacent to the periodic regime a broadband spectrum was observed but no explanation was provided and no further investigation was done. We believe that these broadband frequency regions are due to the non-periodic flux motion, possibly chaotic dynamics. This is because the frequency spectrum of a chaotic dynamics consists not of individual spectral lines but of a broadband background. In our experiment (Section 6.5) we observe the individual passage of the flux tubes, and this allows us to analyze the entire dynamics (periodic or otherwise) as the current is varied.

A time-resolved technique can also be used to detect individual multiquantum flux tubes moving across a type-I superconducting strip [27, 136]. The temporal structure of flux-flow voltages, generated by individual moving flux tubes, consists of fast sequences of very small amplitude pulses [137, 138, 139]. Unfortunately, opening the required wide detection bandwidth increases the noise, causing a poor signal-to-noise ratio. Thus, heavy signal averaging is required. However, for signal averaging, a repetitive voltage signal is necessary and this was realized by periodically turning on and off the flux flow state in the sample, by again superimposing a small ac current over the dc bias current, triggering the flux nucleation at controlled times. Again, this forces the flux dynamics to be a periodic one, so non-periodic dynamics cannot be investigated in this way.

By combining the above mentioned techniques, the high-resolution magnetooptical flux detection (visualize transient flux tubes) and the time-resolved flux-flow voltage (measure temporal structure of flux tubes), more details about dynamics of flux tubes in CIRS have been derived [140]. Thus, the recorded temporal voltage structures agreed well with the voltage pulses derived from velocity profiles of flux tubes observed simultaneously in magnetooptical detection.

Based on the above mentioned experiments, we did some preliminary calculations regarding the dynamics of the driven-current flux tubes that we want to study along a 1D channel. Thus, according to the Josephson relation 6.1, single-quantum vortices flowing along a 1D channel will generate a voltage of 1 μV at a frequency around 500 MHz [141]. Their dynamics is way too fast for an individual detection. However, flux tubes containing about 150 Φ_0 generate 300 nV [135] at a frequency of 1MHz. In this case, the dynamics is slow enough to detect the flux tubes as individual entities flowing along the channel. In our experiment we use the Hall probe for individual detection of the current-driven flux tubes.

6.3 High-Speed Flux Dynamics Recorded by Hall Probe Microscopy

In the previous section we saw that the dynamics of nucleation and subsequent motion of flux tubes along a 1D channel has not been explored in a direct way for the entire range of the applied current. It was either limited to a range where periodicity was naturally present (as in the direct observation of flux tube-flow [135]), or the periodic regime was induced by a periodic perturbation (stroboscopic magnetooptical experiments and time-resolved flux-flow voltage experiments).

None of the experiments concerning the current-driven flux motion along a 1D channel tried to address the investigation of a flux dynamics other than periodic. Using the Hall probe microscope we have been able to directly explore for the first time the *entire* dynamics (periodic and non-periodic) developed by current-driven flux tubes flowing along a 1D channel. In this section we present the technique that we developed for this experiment. Briefly, this consists of a Hall probe fixed above the channel at a chosen location. The Hall probe detects the flux tubes passing beneath as the current is varied. The result is a time series of individual flux "droplets." In the following is described each component of our measurement system.

We faced some inherent challenges in recording high-speed flux dynamics. Two major issues had to be solved: to have a wide detection bandwidth, and to amplify the signal in this frequency band, while keeping the signal-to-noise ratio low. The first issue comes from the high speed at which the flux tubes dynamics occurs: between 10 kHz and 1 MHz. The second issue is the gain that needed. To estimate this gain, we need to estimate the field due to a flux tube at the active area of the Hall probe. The field at the center of a flux tube is equal to the critical field of the superconductor being used which is lead in our experiment. The critical field of lead is quite high, about 500 G at 4.5 K. However, the channel which contains the flux flow is about 1μm below the adjacent regions and its small width (about 3 μm) keeps the Hall probe from coming into contact with the bottom of the channel (details about fabrication are provided in the next section). Finally, the active area of the Hall sensor is not exactly at the tip of the chip but about 13 μm from the tip. With $\sim 1/17$ slope of the Hall probe, an additional 1 μm is imposed. Thus, the active area is about 2 μm above the surface of the superconductor. Let's estimate the field above the top of a flux tube.

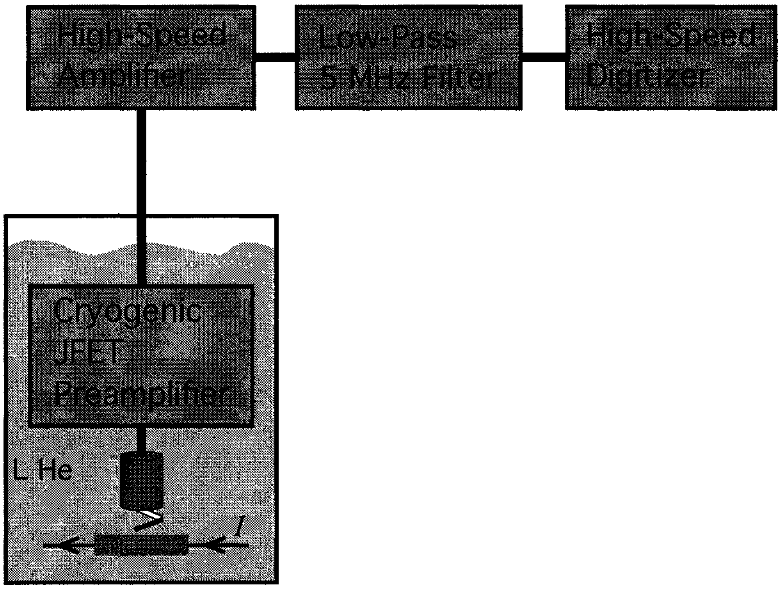

Figure 6.5: The measurement system used in detecting the high-speed dynamics of the flux tubes.

In the flux tube model [6] developed for a type-I superconducting film in an applied pependicular magnetic field, the magnetic field of a flux tube decreases with the distance above the surface as:

$$H(z) = H_c\left(1 - \frac{z}{\sqrt{z^2 + (D/2)^2}}\right), \tag{6.2}$$

where D is the diameter of flux tube. A rough estimate shows that 2 μm above the surface, the magnetic field of a 3 μm diameter flux tube at 4.5 K will be about 100 G. Though this is a large field for regular Hall probe imaging, in the present experiment, with the inherent noise brought by opening the bandwidth, we needed to maximize the signal-to-noise ratio by careful low-noise amplification.

To accomplish this, we have carefully optimized each part of our measurement line (see Fig. 6.5), which consists of a Hall probe, low-temperature JFET preamplifier, a room-temperature wideband amplifier, a low-pass filter, and a high-speed data acquisition board. In the following I will describe each of these parts.

Hall probe design for high-speed flux dynamics. We developed a new wideband Hall probe to detect the high-speed dynamics of flux tubes. Regular Hall probes (Fig. 4.12a) have an ohmic resistance of the current and voltage leads (from active area to contact pads) of about 2.5 kΩ at 4.2 K. With an estimated coupling capacitance of about 30 pF along the wires which go from the Hall probe to low-temperature JFET preamplifier we get a cut-off frequency around 2 MHz, which barely covers the desired frequency range. To increase this frequency band more we reduced the voltage probe resistance by modifying the aspect ratio of current and voltage leads. Thus we reduced the area covered by the current leads and correspondingly expanded the voltage leads (Fig. 4.12b). The resistance of a wedge arm is $R = R_\square \ln(b/a)/\theta$, where $R_\square(\Omega/\square)$ is the sheet resistance and θ is the angle between the sides of the arm; the planar shape of an arm is shown in Fig 6.6. By spreading out the voltage lead pattern (increase the angle θ) and reducing the current lead pattern as much as possible, we have been able to achieve a 1 kΩ resistance for each voltage lead at 4.2 K. This provides us a frequency bandwidth of about 5.5 MHz, large enough for the flux tube dynamics in our experiment.

In the new Hall probe design we kept an even aspect ratio of the cross (each cross arm is 1.5 μm). The only trade-off was that the active area of the cross is a little farther away from the tip (about 13 μm) compared to the standard design used for

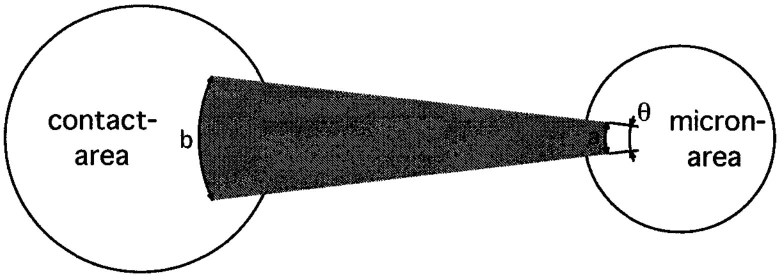

Figure 6.6: The wedge shape of the Hall leads.

imaging (about 7 μm). Of course, another way to lower the contact resistance is to choose a wafer with lower sheet resistance, which is given by $R_\Box = 1/ne\mu$. However, we also want a larger Hall coefficient $R_H = 1/ne$ for our wafers, so these requirements are somewhat contradictory. For example, the wafers presented in Section 4.2 have the sheet resistance of about 70 $\Omega/\Box$: 66 $\Omega/\Box$ (Gossard group's wafers) and 75 $\Omega/\Box$ (Shtrikman group's wafers).

Low-temperature JFET preamplifier. We used JFETs to build a low-temperature differential amplifier. We chose JFETs because they work at low temperature and we could put them near to the Hall probe (right on top of the cryostat can). This provided us a great reduction of the coupling capacitance along the way from the Hall probe's output to the JFETs' inputs .

To measure the small differential signal developed across the Hall probe's voltage leads, we need a differential amplifier with a high common-mode rejection ratio (CMRR). The circuit of this JFET preamplifier, shown in Fig. 6.7, consists of two parts, one which is inside of a box which is kept at 180 K (the box sits above the

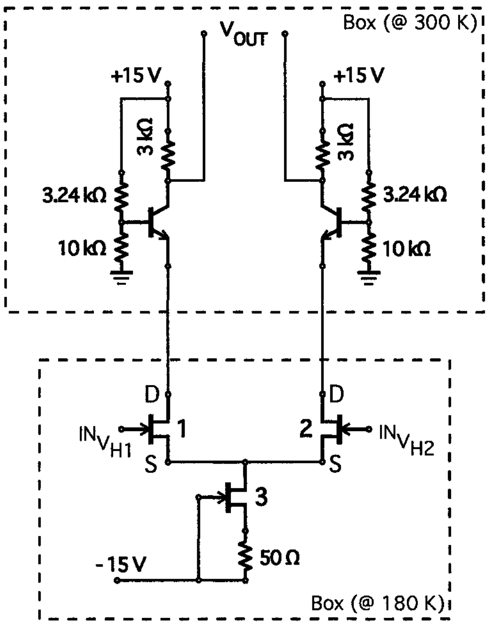

Figure 6.7: Low-temperature preamplifier followed by a room-temperature cascode configuration.

cryostat can, surrounded by but insulated from liquid helium), and one which is inside of a second box at room temperature (this box is on top of the cryostat). The low temperature part comprises two ultra low noise Toshiba 2SK117 JFETs (#1 and #2) and one NTE312 JFET (#3). The JFET #3 is used as a current source, providing about 2 mA which is shared equally between the sources of JFET #1 and JFET #2. Such current source biasing of a differential amplifier, because it has an infinite impedance, will provide a nearly zero common-mode gain: keeping the total current constant, the output will not be sensitive to common-mode input swing. As a result, the CMRR will be increased.

The input signal (the voltage from the Hall probe) goes into the gates of JFETs

#1 and #2. The JFETs work as transconductances converting the voltage signal into a current signal, so the output is taken in form of a current signal from the JFETs' drains. We need to bring this current signal all the way to the top of the cryostat ($\sim$ 35 inches) and measure it as a voltage. The easiest way to do this would be to terminate each output wire by a resistance to ground; the output signal would be then the voltage read in front of the resistors. However, for each output wire, the RC filter made by these resistors and the coupling capacitance introduced by the long wire would cut off the frequency bandwidth of the current signal coming from the JFETs' drains. The solution to this issue was to keep the two long wires at a *fixed* voltage, thereby preventing the RC filter to be formed. In this case, the coupling capacitance of the long wires coming from the JFETs' drains becomes unimportant. To fix the voltage of each wire we put a cascode section in front of the outputs, inside of the box on top of the cryostat.

The cascode (top part of Fig. 6.7) was made with two regular pnp bipolar transistors biased at fixed voltages provided by voltage dividers. Each voltage divider assures 9.6 V on each transistor base, so the operating voltage at each transistor emitter will be $V_{\rm E} = V_{\rm B} - 0.6$ V $= 9.0$ V. Therefore, by interposing transistors in the output path we prevented the JFET voltages from swinging. Because the transistors emitters are kept at fixed voltages, the drains of the JFETs will also be at fixed voltages, so the drain currents will be passed unchanged all the way to the outputs. The gain of the JFET preamplifier was about 24 at 180 K, and the CMRR was about

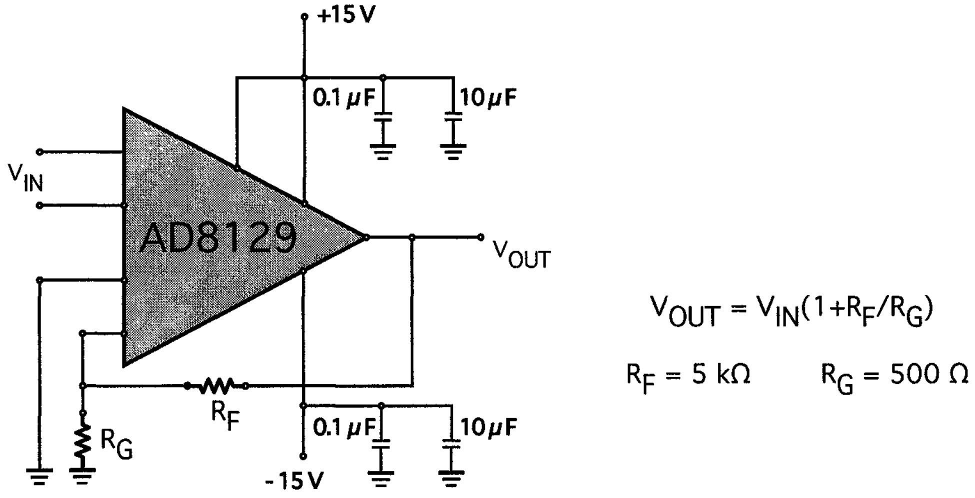

Figure 6.8: Room-temperature wideband amplifier.

50 dB.

Room-temperature wideband amplifier. For a further amplification at room temperature we found it adequate to use an AD8129, which is a low-noise high-speed differential receiver amplifier. Its noise is as low as 4.5 $\mathrm{nV}/\sqrt{\mathrm{Hz}}$, and the CMRR is about 70 dB up to 10 MHz. The basic op-amp configuration is presented in Fig. 6.8. Each power supply pin was low frequency bypassed with ceramic chip capacitors (0.1 and 10 μF).

We used the AD8129 with either dc or ac response. In the ac response mode the inputs were high pass filtered at about 3 kHz. We extensively used the ac response because with this method the $\sim$ 9 V dc voltage is blocked; this 9 V voltage was close to the maximum allowed input voltage and led to continual device failure. On the other hand, using the dc response, we were able to keep track of the zero of the magnetic field, allowing us to measure the polarity of the pulses. In the dc response we used the reference pin of AD8129 to offset its output with respect to ground and properly display it on the oscilloscope scale. The gain of the op-amplifier was set to be 11.

Chebyshev low-pass filter. Before being digitized, the signal is filtered by a low-pass band Chebyshev active filter with a measured cutoff frequency of 5 MHz. The Nyquist theorem states that a signal must be sampled at least twice as fast as the bandwidth of the signal, in order to have an accurate waveform reconstruction. Otherwise the high-frequency content will alias down to a frequency inside the spectrum of interest. This is particularly bad since it aliases down noise as well. We digitize the signal at 10 MHz, meaning that the Nyquist frequency is about 5 MHz. Using a 5 MHz low-pass filter we limited the frequency content of the input signal above the Nyquist frequency.

We chose to build a Chebyshev fourth order filter with two cascading stages to get a steeper falloff at the rolloff frequency (0.1 dB of ripple in the passband). Though they only have moderately good flatness within the passband, Chebyshev filters have a much faster cutoff of the signal at the desired frequency than other filters such as the Butterworth or Bessel filters.

The basic circuit is presented in Fig. 6.9. The components of each stage have been calculated [142] for a desired cutoff frequency of $f = 5$ MHz and a gain of 3 (2 from the first stage, and 1.5 from the second one). The frequency response of our filter is presented in Fig. 6.10.

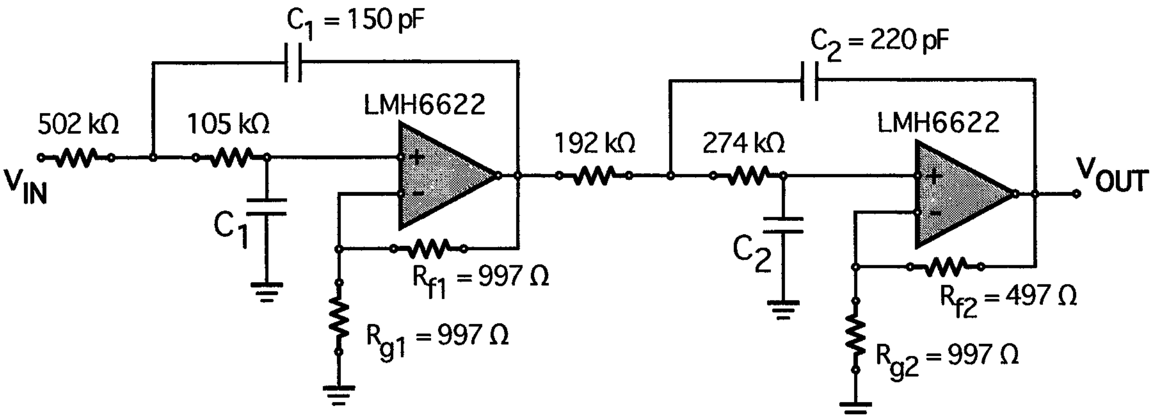

Figure 6.9: Fourth order Chebyshev filter.

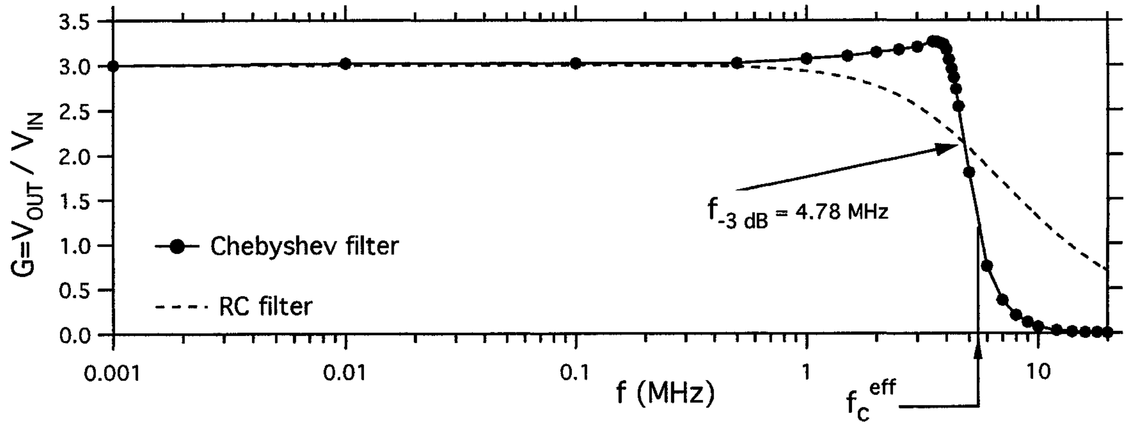

Figure 6.10: The frequency response of the Chebyshev filter compared with that of a RC filter having the same cut-off frequency at −3dB.

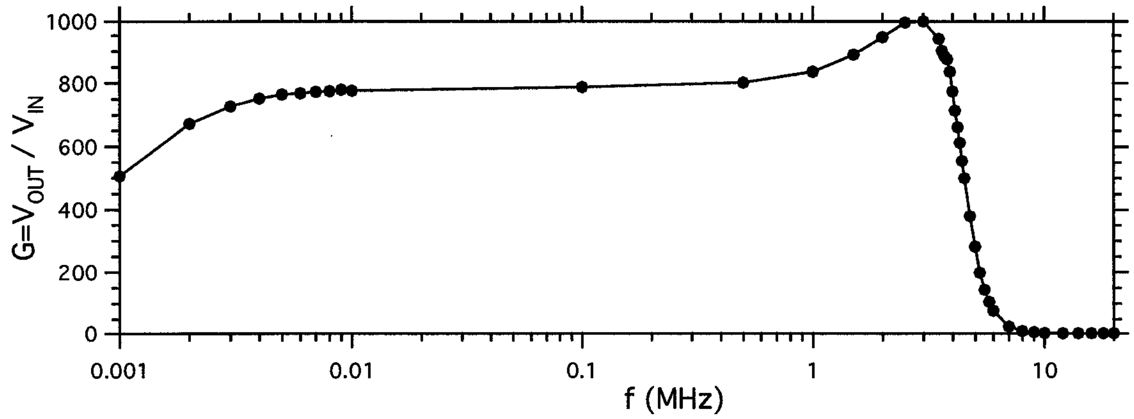

Figure 6.11: The frequency response of the measurement line at room temperature.

The root-mean-square noise $V_{\rm rms}$ over a frequency range is calculated as the sum of the root-mean-squares e_n from each frequency element df,

$$V_{\rm rms} = \sqrt{\int_0^\infty e_n^2(f)G^2(f)df}, \tag{6.3}$$

where $G(f)$ is the frequency dependence of the gain $G = V_{\rm OUT}/V_{\rm IN}$. Considering that e_n is almost independent of frequency, the effective noise bandwidth is given by

$$f_c^{\rm eff} = \frac{1}{G(0)}\frac{V_{\rm rms}^2}{e_n^2} = \frac{1}{G(0)}\int_0^\infty G^2(f)df, \tag{6.4}$$

where $G(0)$ is the dc gain. With the above formula, the effective noise bandwidth of our Chebyshev filter was calculated to be $f_c^{\rm eff} = 5.3$ MHz. In Fig. 6.10 is also shown the frequency response of a RC filter (dashed curve) having the same cut-off frequency at -3dB as our Chebyshev filter, $f_{-3{\rm dB}} = 4.78$ MHz.

Overall, the whole measurement line has a noise of 2–3 nV/$\sqrt{\rm Hz}$ and a gain of about 830 (at 1 MHz) at room temperature (25 from the JFETs, 11 from the room temperature wideband amplifier, and 3 from the Chebyshev filter). Its frequency response is presented in Fig. 6.11. We found that the noise depends on the JFET temperature. The lowest measured noise, $e_n = 1.28$ nV/$\sqrt{\text{Hz}}$, was around 180 K, so the JFET preamplifier was kept at this temperature. Over the 5.3 MHz noise bandwidth, this means a root-mean-square noise V_{rms} of 2.95 μV. The gain at 180 K was about 1300.

High speed data acquisition board. To digitize the signal we used in preliminary runs an Agilent Infiniium oscilloscope, and subsequently, for much better data storage, a high-speed PC board was used. This was a NI 5102 high-speed digitizer from National Instruments. The buffer of this board can store up to 16 million samples at a maximum rate of 20 MHz.

6.4 Fabrication of constricted lead strips

We fabricated a constricted lead strip, with a geometry similar to that used in Ref. [143], in order to control the nucleation location and the subsequent path of motion of the flux tubes (Fig. 6.12). In a two-step evaporation, a channel (1 μm deep, 3 μm wide, and 160 μm long) was patterned across the strip. First, on a clean sapphire substrate a uniform varnish fiber (3 μm in diameter) was carefully laid down across the substrate. A metal mask was centered over the varnish to define a 1-mm-wide by 6-mm-long window for the first 1-μm-thick evaporated lead layer. After the evaporation, the varnish fiber was dissolved in acetone, leaving a gap equal to the

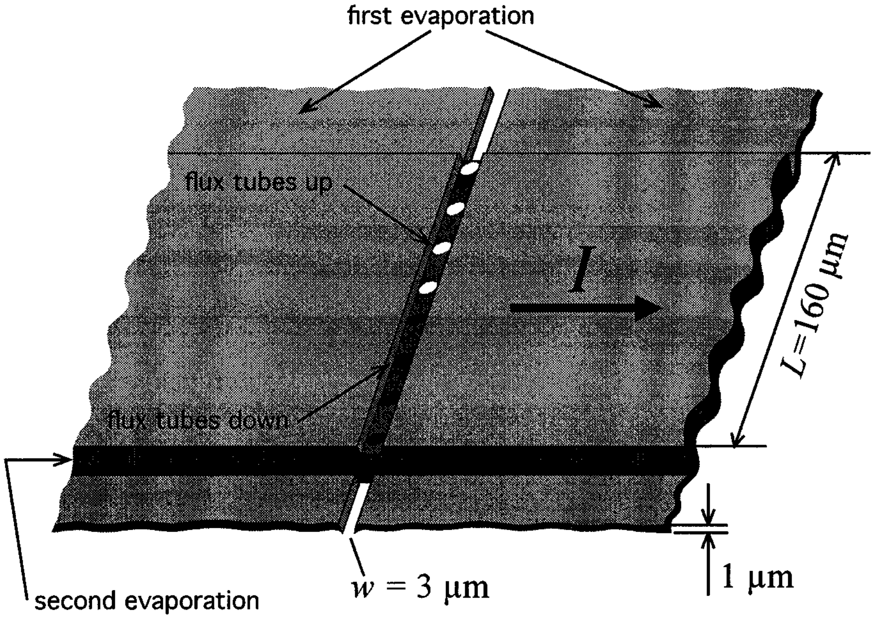

Figure 6.12: The constricted lead strip used in the "superconducting dripping faucet" experiment.

fiber width. We used the old-fashioned varnish method because this gave us good liftoff on this very thick lead evaporation. Then, using a second metal mask—two razor blades separated by a 150–160 μm space—the gap is bridged by an overlaid lead film, about 4 μm thick.

Consequently, the constriction is 3 μm wide, 160 μm long and 4 μm thick. The adjacent parts are 160 μm wide, 3 mm long from the constriction to the ends (where the contacts are soldered) and 5 μm thick. In this way, by thickness modulation, a microbridge is defined across the strip. The first layer (1 μm) thick serves not only to define the channel by modulating the thickness, but also, being wider than the strip, will funnel the applied current down to the ends of the constriction. The large current density at each end of the channel assures that this is where the flux tube nucleation first starts. The width of the channel largely determines the size of the nucleated flux tubes. A 3 μm wide channel will host flux tubes containing about 100–200 flux quanta [6], large enough to give a large Hall probe signal and to slow the dynamics down to observable frequencies.

We chose a sapphire substrate due to its high thermal conductivity, about 50 W/cm K in the temperature range 10–100 K; except for silver, sapphire has the highest thermal conductivity in this temperature range. With such a high thermal conductivity, the substrate will help to prevent an early breakdown of superconductivity due to the heat generated by large driving currents. Also, to prevent a possible thermal damage of the sample during a sudden transition to the normal state, a shunt resistance of 40–50 mΩ was placed in parallel with the current contacts. Although this is a small resistance, it is still much greater than the effective resistance of the superconductor when this is in the resistance flux-flow state.

The lead samples for this experiment have been produced by vacuum deposition of high-purity lead material. The ambient pressure during evaporation was around 10^{-6} Torr, and the deposition rate higher than 200 Å/s in order to minimize lead oxidation during the evaporation. The critical temperature of the samples varied between 7.00 and 7.15 K. At room temperature, most of our samples had an electrical resistance $R_{300\ \mathrm{K}}$ around 500 mΩ whereas at the critical temperature the resistance $R_{7\ \mathrm{K}}$ was about 1 mΩ. The resistance $R_{7\ \mathrm{K}}$ is called the *residual resistance* and is mainly due to scattering of electrons from impurities and defects. Conversely, $R_{300\ \mathrm{K}}$ is due mostly to phonon scattering and it is largely independent of the sample purity. Consequently, the ratio of the room-temperature resistance to the residual resistance, $RRR = R_{300\ \mathrm{K}}/R_{7\ \mathrm{K}}$, reflects the disorder present in the film structure. The effective mean free path of electrons is related to the residual resistance ratio RRR by [144]

$$l_{\mathrm{eff}} = (RRR - 1)\frac{\rho l}{\rho_{300\ \mathrm{K}}}. \tag{6.5}$$

In the above formula the product ρl remains basically constant upon adding impurities and for lead is $\approx 1.5 \times 10^{-11}\Omega\ \mathrm{cm}^2$ [145]. The room temperature resistivity $\rho_{300\ \mathrm{K}}$ is 21 $\mu\Omega$ cm for lead. Thus, we estimate that the effective electron mean free path is longer than 3 μm. This implies that our lead samples are of very high quality and purity, so the mean free path is not limited by scattering on defects and impurities.

We tried constriction widths between 3 and 10 μm, and depths of 1 and 2 μm. We found that the wider channels allow the nucleation of pairs of flux tube trains along the channel. The deeper channels meant the Hall probe was further from the top of the flux tubes, reducing the signal significantly. The 1 μm deep, 3 μm wide channels were found to be optimal for the experiment.

We also tried to fill the gap after the first evaporation with an insulator at the same level as the evaporated layer. In this way, the second layer would have a uniform height, even over the channel, allowing the Hall probe to come very close to the surface of the channel. Unfortunately, we were not able to evenly fill the gap. We found that in such filled channels two trains of flux tubes always developed along the channel, one at each edge. Presumably, multiple trains influence each other, complicating the analysis, so this method was not used.

6.5 Complex Dynamics of the Superconducting Dripping Faucet

In this section we present the observed dynamics of our "superconducting dripping faucet." We are mainly interested in the time intervals between successive current-driven flux tubes that nucleate and move along the fabricated 1D channel. Preliminary Fourier analysis of recorded time series reveals the complex dynamics of our "superconducting dripping faucet."

Recorded flux tube dynamics along a 1D channel. By positioning the Hall probe above different locations along the channel we have been able to record the passage of individual flux tubes at those locations as the dc driving current is varied. The Hall probe measures a voltage pulse each time a flux tube passes beneath it. Therefore, as the driving current is varied, the flux tube sequence is acquired by the Hall probe as a time series of voltage pulses. Before acquiring the time series of flux tube motion at some particular location along the channel, we took several regular scanning images to see the global development of the flux nucleation.

In Fig. 6.13a is shown a magnetic image of a constricted lead strip in a perpendicular applied field of 50 G at 6.0 K, no current flowing through the strip. The

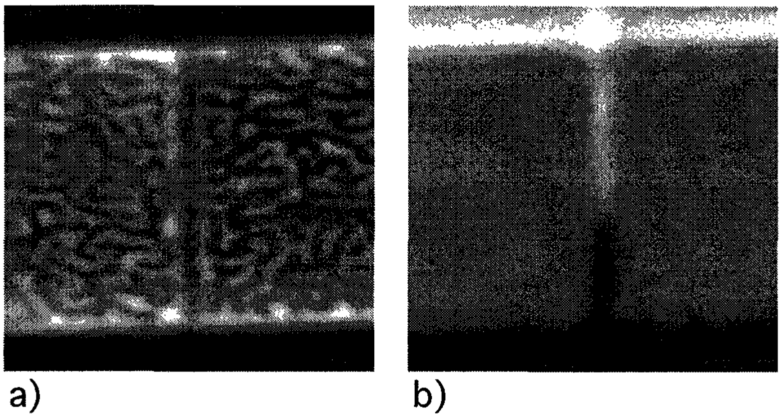

Figure 6.13: Scanning Hall probe images above the constricted lead strip at 6.5 K: a) in a perpendicular field of 50 G; b) first flux tubes nucleate into the channel when 274 mA current was applied along the strip.

fabricated channel meant to guide the flux tube-flow is clearly visible. Adjacent to the channel, the thicker regions exhibit the intermediate state typical of corrugated flux domains. In this case, with a magnetic field applied perpendicular to the strip, flux tubes will penetrate the channel in an equilibrium configuration with the flux domains in the adjacent areas.

In Fig. 6.13b is shown the magnetic field profile obtained when a current is applied along the strip, perpendicular to the channel. Here, no external magnetic field was applied. In a scanned image like this we can not see individual flux tubes along the channel because these are moving at microsecond time scales, while the picture is taken in about 4 min. So here we image the *time averaged* motion of the flux tubes. In Fig. 6.13b we also see how flux tubes of opposite polarity break off from each end of the channel. The magnetic field of the driving current makes the flux tubes at the channel top to point up (white), whereas at the channel bottom

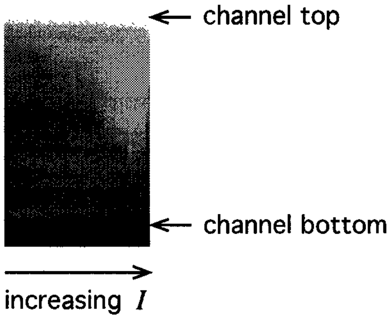

Figure 6.14: The flux annihilation point moves along the channel as the current is increased.

they are pointing down (black). Flux tubes are breaking off from each channel end just like from a faucet neck. After breaking off, they travel under the action of the Lorentz force towards the middle of the channel, where they are annihilated by the opposite sign flux tubes coming from the other end.

By regular Hall probe scanning we can also observe the magnetic profile along the channel and see the evolution of the advancing flux front as the driving current is increased through the strip. Thus, in Fig. 6.14 the current was slowly increased while the Hall probe was scanned along the channel (no scanning on the horizontal direction). We can see that the annihilation point moves along the channel, mainly around the middle of the channel whereas the top and the bottom regions are not affected. The flux annihilation point moves around the middle position as the driving current is varied because the channel is not quite perpendicular on the current direction. Also the strip's edges don't have the same cut-profile and this causes a slightly different current distribution along each edge. In an ideal sample with identical edges and uniform current distribution across the channel, the flux annihilation point should stay in the middle at any driven current above the critical current.

In the "superconducting dripping faucet" experiment we were interested in the dynamics of flux tube nucleation. Therefore, to avoid the influence of the flux annihilation point on the recorded dynamics, we positioned the Hall probe about 10–40 μm from one of the channel ends. At these locations, the flux tubes are well detached from the edge and they are always pointed in the same direction. In this way, the observed flux tube-flow dynamics is due to only nucleation and subsequent motion along the channel, without being further complicated by flux tube annihilation. At locations further away from the channel ends we observed, using the dc response of the wideband amplifier, how the flux tubes detected by the Hall probe change their polarity as the driving current is varied and the annihilation point moves past the probe.

The flux tubes start to nucleate from each channel edge as soon as the magnetic field of the driving current surpasses the critical magnetic field at the strip edge. This current is defined as the critical current of the strip, I_c, at which the flux tubes just start to nucleate into the channel. It was possible to record the individual motion of the flux tubes up to a threshold current value, I_0, at which the flux tubes coalesce into one long droplet and the channel goes normal.

For currents larger than this value, flux trains adjacent to the channel start to

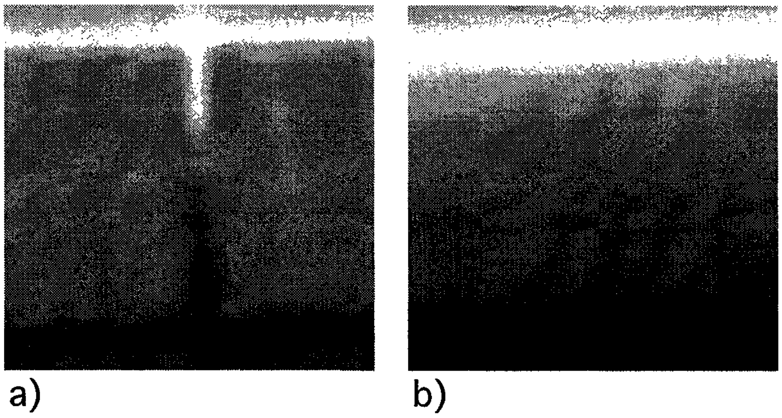

Figure 6.15: At 6.50 K flux tubes adjacent to the channel were observed at a current of 294 mA, whereas b) at 430 mA the whole sample goes into the normal state.

T(K)	I_c (mA) (nucleation starts)	I_0 (mA) (channel goes normal)	I_n (mA) (sample goes normal)
4.0	470	730	785
5.0	350	595	650
6.0	220	495	

Table 6.1: Critical currents of the CIRS of a constricted lead strip.

flow across the strips (Fig. 6.15a). As the current is further increased, more and more flux trains appear and, eventually, at currents much bigger than I_0, the sample will go normal. In Fig. 6.15b the sample is normal, with the observed magnetic profile due only to the current flowing along the strip. The current range of interest, between I_c and I_0, usually was about 250 mA. In Table 6.5 are presented values of these currents at different temperatures for a sample having a channel 5 μm wide, 1 μm deep, and 160 μm long.

Though the flux tube dynamics changes as temperature is varied, we didn't established a convincing pattern of this dependence. The most repeatable recorded dynamics, with the least hysteresis, was obtained by always cooling the sample from above T_c to the desired temperature, and then increasing the current through the sample.

Preliminary analysis of time series data. In our experiment we tried several lead samples with slightly different dimensions of the channel and made measurements at different temperatures. As the current through the strip was varied, the dynamics of flux tubes was investigated at different places along the channel. At a given place, the Hall probe recorded a time series of voltage pulses. The time series represent the temporal succession of the flux tubes passing at that particular place where the Hall probe was positioned. We observed a rich plethora of periodic and non-periodic pulse sequences. Some typical sequences observed in our time series are shown in Fig. 6.16.

After recording the time series, we first examined the pulse trains generated at different applied currents through the sample, and then analyzed the series using Fourier analysis. Fourier analysis is a standard step in time series analysis, regardless of whether the data are periodic or non-periodic. The purpose of doing a Fourier analysis is to search for possible periodic structures in the data by looking at it in the frequency domain.

We recorded the flux tube dynamics at a given location over the channel in two ways:

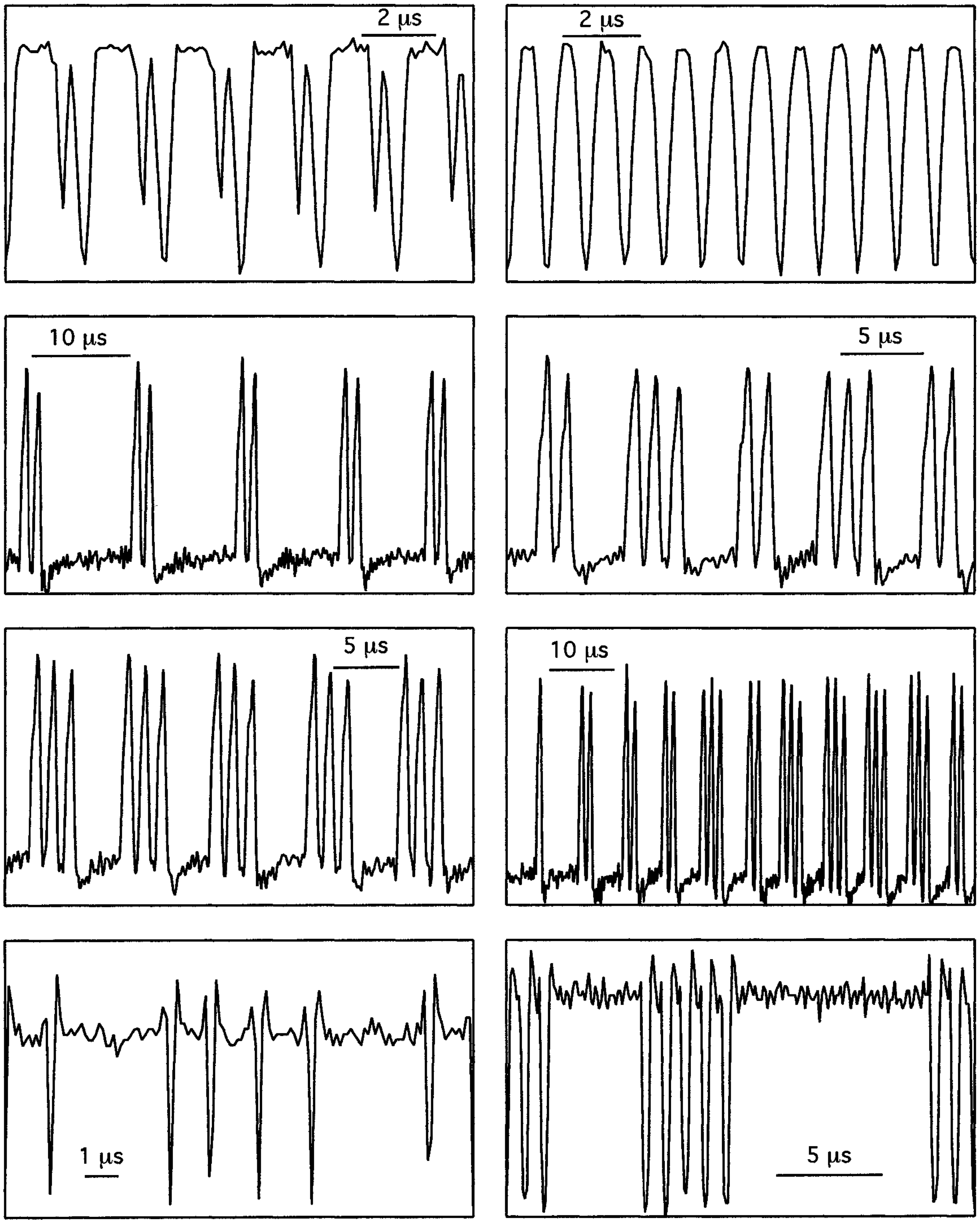

Figure 6.16: Sequences of voltage pulses recorded by the Hall probe during the flux flow along the 1D channel. On each figure the time scale is specified.

1. Varying the driving current in 100 steps over a range from I_c to I_0, and at each current taking a 100000 point time series at a rate of 10 MHz.

2. Slowly varying the driving current over the same range I_c–I_0 while continuously recording just one 16 million points time series at a rate of 10 MHz. One such run takes 1.6 s.

The second case was preferable for analysis because in these 16 million points we have the whole development of flux tube dynamics, as the control parameter is varied.

We run this experiment on 10–15 different samples. In the majority of samples we have been able to identify three distinctive regimes when the driving current is varied from the critical value I_c to the threshold value I_0. In the following we will focus on the flux tube dynamics recorded at 4.50 K above a point located about 40 μm from one channel end, in a sample for which the channel is 3 μm wide, 160 μm long, and 1 μm deep. We will refer to this as "Sample A."

When the driving current is increased above the critical current ($I_c = 497$ mA at 4.50 K for this sample), the flux tubes start to move through the channel. The corresponding voltage pulses detected by the Hall probe are irregular in size. In this **Region I** we observe pulse sequences of different periodicity (e.g., in Fig. 6.17a is shown a double-period sequence from this Region I). As the driving current is further increased, the *periodic* sequences turn into what we called *transient* sequences. Here a transient sequence consist of different periods which don't succeed regularly one after the other, but instead change randomly from one period to another. For example, a

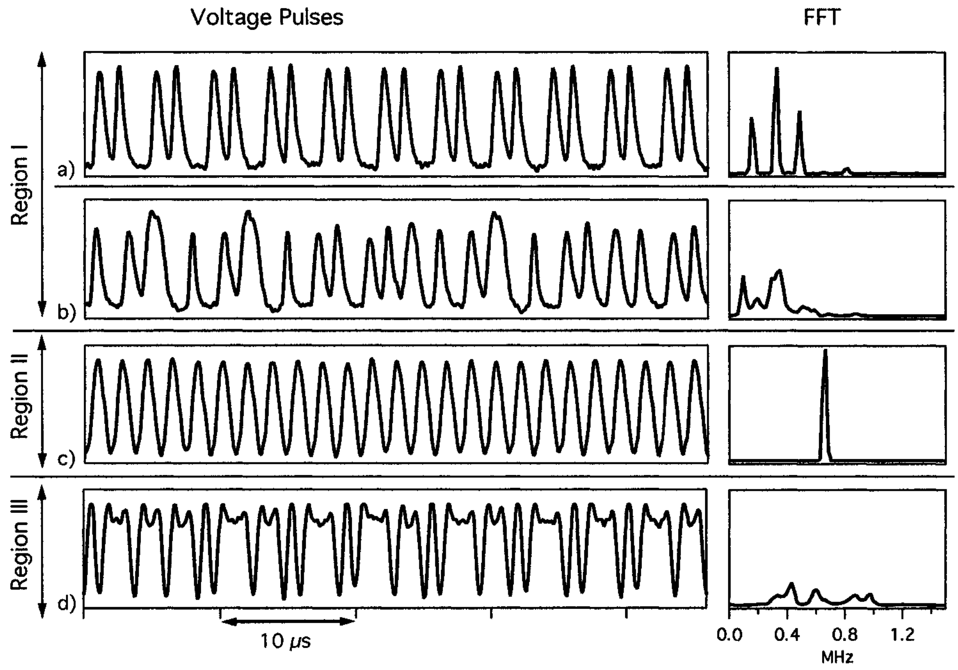

Figure 6.17: Sequences of voltage pulses and their Fourier power spectra.

transient sequence of periods A, B, and C shows the periodic order ABCABCABC... for a wile and from time to time this kinks into different combinations of A, B, and C, like ABABCBABABC or ABCABABCABABAB. Even if the order of periods is not regular in a such transient sequence, the periods are still well defined. We observed transient sequences of two, four, up to six different periods. As the current is further increased, the transient sequences turn into a quite nonuniform distribution of time intervals between successive voltage pulses. It is not possible to distinguish any particular periods. Such an irregular flux tube train is presented in Fig. 6.17b. As the current is increased, these kind of irregular sequences come in an intermittent way (between them the dynamics comes back to a quasi-periodic behavior) and mark the end of Region I.

The complex development of the dynamics in Region I is evident in the Fourier power spectrum (right panels in Fig. 6.17). We can see that well defined and quite sharp spectral lines are present in the Fourier spectrum of the periodic sequence a). However, in the Fourier spectrum of the non-periodic sequence b), the spectral lines are not sharp and is difficult to localize them; they are accompanied by a broadband background with substantial additional power. Though the power spectrum could be interpreted as individual spectral lines contaminated by noise, this could also be a first qualitative indication that the involved dynamics is nonlinear and possibly deterministic.

As the driving current is increased further, the dynamics suddenly turns into a perfectly periodic one (Fig. 6.17c). This is the beginning of **Region II**. For this particular sample, at 4.50 K, the periodic regime was observed for currents between $I_1 = 525$ mA and $I_2 = 565.5$ mA. The periodicity is also observed in the corresponding Fourier power spectrum of this region. A sharp spectral line is observed and no noise is present. The absence of noise tells us something else: the source of the broadband signal presented in the Fourier spectrum of Region I is evidently due to the underlying dynamics and not to noise such as measurement noise. In Region II the flux-tube frequency increases from about 500 kHz to 800 kHz as the driving current is increased; this shift will be explained later in terms of a model of the flux tube dynamics (Section 6.7).

At even higher driving currents, the flux tubes start to coalesce and make long sausage-shaped flux drops along the channel. This is what we call **Region III**. The dynamics again becomes irregular, showing non-periodic sequences of large droplets followed by small ones (Fig. 6.17d). The non-periodic behavior of Region III is confirmed by its Fourier power spectrum. Now it is not possible to distinguish any individual spectral lines, the spectral power being spread over a large frequency range. With the further increase of the driving current, the dynamics of Region III becomes more and more irregular and, finally, a continuous flux flow settles down through the channel: the channel goes in the normal state.

Bifurcation map of the current-driven flux tubes. By collecting the "dripping" time intervals—the time between successive pulses—as the driving current is varied, a *bifurcation map* is obtained. This shows us qualitatively how the dynamics evolves as the control parameter is varied. A bifurcation map for the dripping faucet experiment was shown in Fig. 6.2. We made the bifurcation map from our time series in the following way. First, we measured the time intervals ΔT as differences between successive intersections of the voltage pulses with a fixed level. Then, at each current corresponding to a found ΔT, we plot a dot at the height ΔT.

Such a bifurcation map for Sample A is shown in Fig. 6.18. In the upper panel is shown the bifurcation map for the entire range of the current. Here we can see clearly the distinct character of Region I, II, and III. Regions I and III show how the time intervals evolve in a complex fashion as the current is increased, while in Region

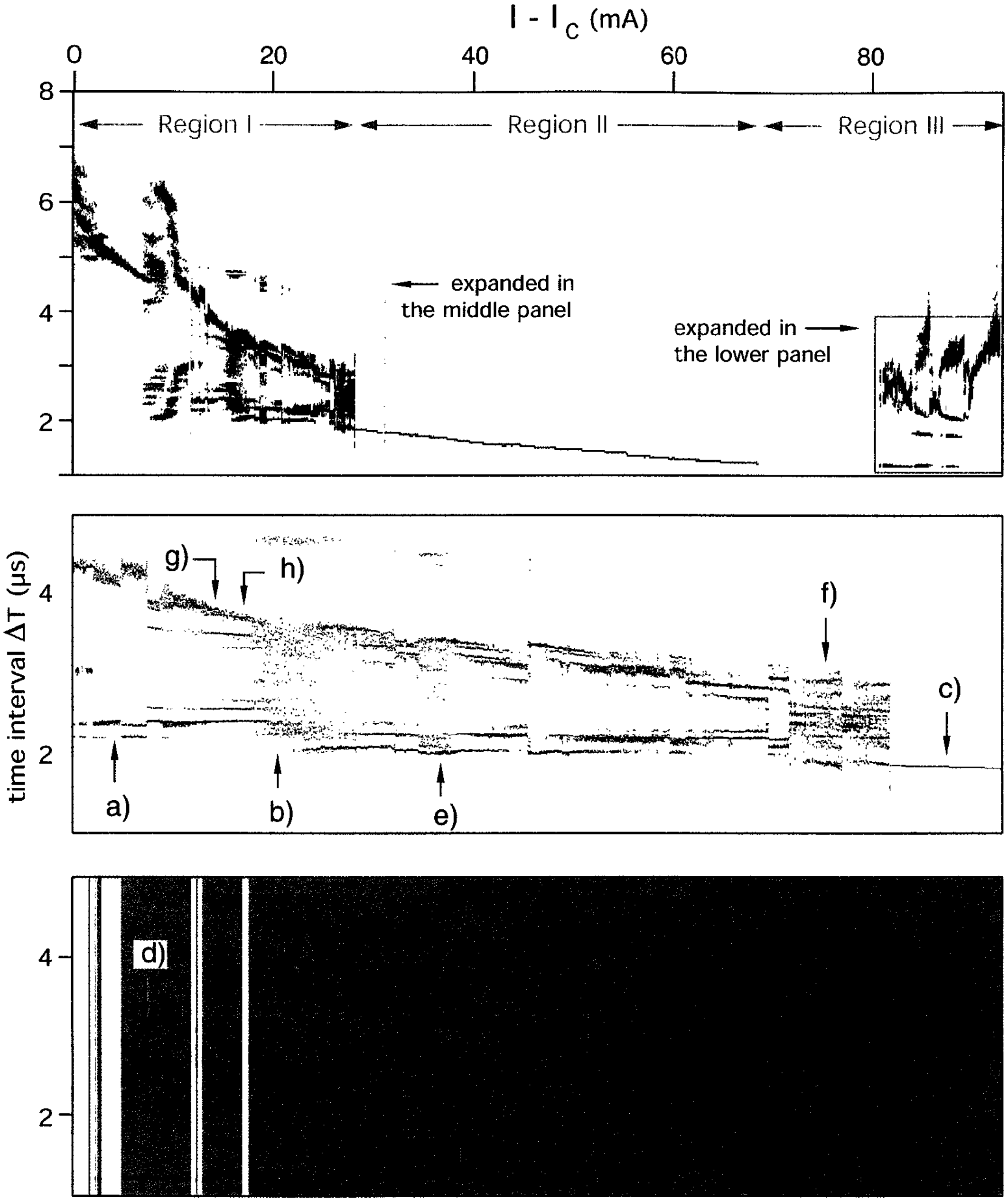

Figure 6.18: The bifurcation map of the "superconducting dripping faucet" as the driving current (control parameter) is varied. The letters a) through h) are referred to in the text.

II there is only one ΔT observed at any given current, indicating periodic behavior.

In the two lower panels of Fig. 6.18 we zoom in on the interesting details of Region I and Region III. The letters a), b), c), and d) in the middle panel of Fig. 6.18 denote the same sequences presented in Fig. 6.17; the sequences indicated e), f), g) and h) will be used later for analysis.

The bifurcation map shown in Fig. 6.18 was made by filtering the bifurcation map obtained from the original time series. This filtering was done as follows: we divided the current range into 1200 bins. Each bin was then replaced by a histogram of the time intervals ΔT from that current bin. In the top panel, the histograms were plotted on a gray scale, white for the likeliest ΔT's, dark for the least-likely ΔT's. In this way we bring out the faint areas compared to the dark areas and more features are revealed. In the middle and bottom panels, the histogram values are shown on color scales from yellow to dark and from green to blue.

In the top panel of Fig. 6.18 we can see that Region I begins with an adjustment region during which the time intervals between successive pulses converge to a value around 4.5 μs for a driving current of 504 mA ($I - I_c = 7$ mA). At this point the dynamics is quite periodic, but then a complex multi-periodic splitting develops as the current is increased. Thus, we have sequences of period-two (like sequence a in Fig. 6.18), and transient sequences of four, and even six different periods (like sequences g and h in Fig. 6.18). This succession of periodic bifurcations leads to broad frequency bands (like sequence b in Fig. 6.18). As the driving current is increased, the non-periodic regions show up in an intermittent way, between them the dynamics coming back to a multi-periodic behavior. The irregular sequences become more and more frequent, last longer, and finally mark the end of Region I. Similarly, the dripping faucet undergoes period-doublings along its route to a chaotic development [122].

The transition from Region I to the periodic Region II occurs at a certain value of driving current ($I_1 = 525$ mA at this temperature of 4.5 K), and it is a sharp and clear change in the dynamics (see the top and middle panels of Fig 6.18). In the past [26, 133, 134, 27, 136, 140], the study of current driven tube dynamics was mainly restricted to this periodic region. When a periodic flux flow is established through the channel, the voltage drop generated across the bridge follows a Josephson-type relation with the rate of flux motion, so $V = N\Phi_0\nu$ (Eq. 6.1); this was discussed in Section 6.2. Once the dynamics becomes periodic it stays strictly so for a long driving current range of about 40 mA. As the driving current is increased, the dynamics becomes faster and faster, and the end of Region II happens at $I_2 = 565.5$ mA ($I - I_c = 64.5$ mA) when the flux tubes start to coalesce.

As can be seen in the upper panel of Fig. 6.18 the transition from Region II to Region III ($I - I_c = 64.5$ mA) is marked by a gap which corresponds to very long flux droplets along the channel, probably due to some temporal instability in the dynamical development. More of such long flux droplets are visible at the beginning of Region III as white vertical strips in the lower panel of Fig. 6.18. The ΔT's corresponding to these long droplets are so high (tens of μs) that we do not plot them on the figure. However, in most of our observations the transition from Region II to Region III was continuous.

The dynamics in Region III is also quite interesting. Though we can still see some remnants of the high speed periodic trace of Region II, new periodic splittings suggest a deterministic development. In this regard, the dynamics looks similar to the faucet dynamics observed in Region I. However, the physics is different now: in Region I what was observed was the dynamics of the flux tube nucleation, similar to the dynamics of a dripping faucet, whereas in Region III the dynamics is governed mainly by inter-flux tubes interactions. At such high frequencies the flux tubes can no longer stay separated, and they form large droplets. This is possible because the flux-flux interaction are attractive in a type-I superconductor. In a type-II superconductor, the vortex-vortex interactions are repulsive, so in an experiment in a type-II material, with vortices traveling along a 1-D channel, Region III will not exist.

In Section 6.6.2 we analyze in detail several sequences from Region I of the bifurcation map shown in Fig. 6.18. These are sequences b), e), and f). From now on, we will call them sequences *chaos_01*, *chaos_02*, and *chaos_03*, respectively.

6.6 Nonlinear Analysis of the Superconducting Dripping Faucet

In this section we will investigate the nonlinear character of the observed dynamics of the current-driven flux tubes moving along the 1D channel of Sample A. Our first examination of data concluded that the underlying dynamics is more complex and not fully resolved by a linear time series analysis such as Fourier transform. Therefore, we will need to attempt a nonlinear time series analysis.

6.6.1 Short description of nonlinear dynamics.

In this subsection we describe the standard tests and specific parameters used in the nonlinear analysis that we applied to our time series. In the next subsection we present the results of this analysis performed with the TISEAN (TIme SEries ANalysis) software package [146].

Phase space reconstruction. The time evolution of a dynamical system is defined in some **phase** (or **state**) **space**. In the phase space, each state of the system is represented by a point. The coordinates of these points in the phase space are components of the **state vectors**. For a deterministic system, once a state is fixed, the states at later times are determined as well. Thus, we can study the dynamics of the system by studying the dynamics of the corresponding phase space points. To do so we have to convert the recorded time series into state vectors. Called a **phase**

space reconstruction, this is the first step of the nonlinear time series analysis and is technically accomplished using the method of delays [147].

In general, a time series is a sequence of scalar measurements $\{s_n\}$ of an experimentally measurable quantity s which characterizes the current state of the system. In our experiment, s is the Hall probe voltage. Taking the measurements at multiples of a fixed sampling time Δt, the time series can be written

$$s_n = s(\mathbf{x}(n\Delta t)), \qquad n = 1, 2, \ldots, N. \tag{6.6}$$

Here, the state of the system at time the t is described by a state vector $\mathbf{x}(t)$; N is the number of measurements. Thus, we usually do not measure the actual state $\mathbf{x}(t)$ but only quantities such as s which functionally depend on this state. Ideally, the more different state quantities s we measure, the better chance for a quality reconstruction we have.

Now that we have a sequence $\{s_n\}$ of measured values, we need to construct a phase space such that a point in this space uniquely defines a state of the system. Thus, we need to decide what should be the dimension m of the phase space and how to form the state vectors $\mathbf{y}_n$ from the time series. This is called a *delay reconstruction*, and, in a m-dimensional phase space, the state vectors $\mathbf{y}_n$ are given by

$$\mathbf{y}_n = \left(s_n, s_{n+\nu}, s_{n+2\nu}, \ldots, s_{n+(m-2)\nu}, s_{n+(m-1)\nu}\right). \tag{6.7}$$

The time difference in number of sample ν (or in time units, $\nu\Delta t$) between adjacent components of the delay vectors is referred as the **lag** or **delay time**. In Fig. 6.19

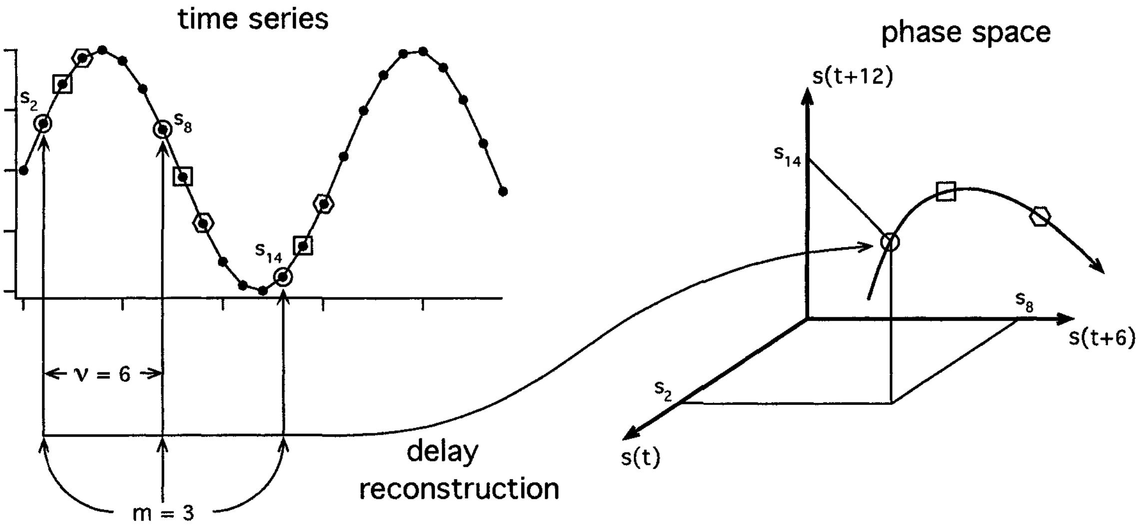

Figure 6.19: Construction of a 3-dimensional phase space from a time series using a delay of 6.

is graphically shown how the delay reconstruction acts on a time series to provide points in the reconstructed phase space.

If we embed a time series of N measurements in a m-dimensional phase space with a delay time ν, then the number of states in the phase space will be $N-(m-1)\nu$. Embedding theorems [147, 148] prove that the scalar measurements s_n are replaced by $\mathbf{y}_n$ state vectors in such a way that the invariant aspects of the original system are preserved. *Invariants* are referring here to those quantities which remain unchanged under the evolution of the system. The new phase space is related to the original one by smooth, differentiable transformations. The invariants are not affected by such transformations, so they are not so sensitive to the phase space reconstruction. Among the most used invariants of a quantitative characterization of the chaotic

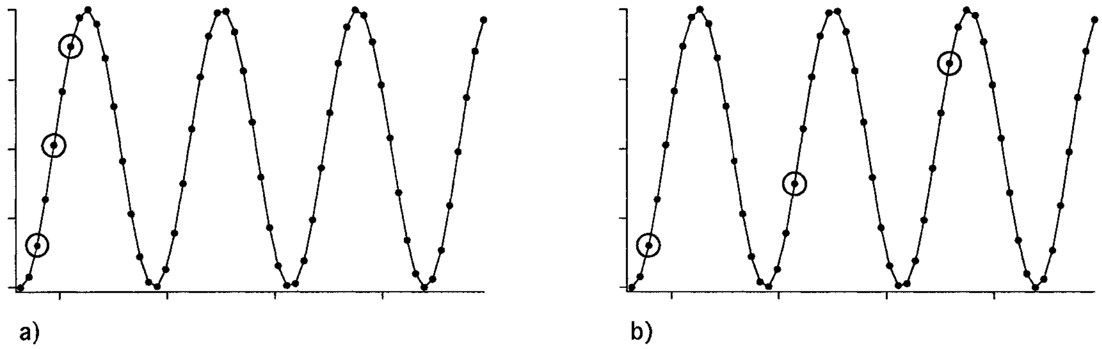

Figure 6.20: Chossing the time delay: a) the delay of 2 is too small; b) the delay of 18 is too large. In both cases the embedding dimension was chosen 3.

dynamics are Lyapunov exponents and dimensions such as the correlation dimension, the fractal dimension etc. Consequently, we can work in the "reconstructed" time delay space and learn essentially as much as we could about the system as if we were able to make our calculations directly in the "true" space of $\mathbf{x}_n$.

Let's see how the parameters m and ν are chosen. A large value of m will make the points in phase space be largely sparse and appear to be unrelated to each other. As a result, the attractor structure will be washed out, being stretched in an exaggerated manner. On the other hand, a small value of m will not allow the whole development of the attractor in phase space. In this case the orbit in phase space will be packed, so that it's not stretched enough to show the details of the attractor structure.

Regarding the time delay, if ν is small compared to the actual time scale of the system then successive state vectors $\mathbf{y}_n$ are strongly correlated. On the other hand, if

ν is very large, even for a reasonable value of m, the vectors formed will not properly describe the actual states of the system because their components are too spread out in the original time series. Two extreme conditions that should be avoided in choosing the time delay are exemplified in Fig. 6.20 for a signal consisting of a series of pulses. Here, the fundamental signature of the dynamics is evidently one pulse of the time series, so we need to be sure that a state in the phase space accurately describes a pulse. Thus, a delay of 2 is too small, since only half of a pulse is covered; a delay of 18 is too large since three different pulses contribute to a single state in the phase space. So, we need to choose a time delay which is large enough that s_n and s_{n+1} are independent, but not so large that they are completely uncorrelated due to the dynamics.

In Fig. 6.21 are shown several experimentally-measured return maps of a time series embedded in a three-dimensional phase space with the delay varying from 1 to 9. We can see that, for this embedding dimension, more and more details are revealed as the delay is increased. A delay of 6 or 7 would be about optimal to see details in the structure of the three-dimensional phase space. For a delay of 9, the points are projected on the faces of the cube, showing that by choosing too large a time delay, we stretch out the distances in the phase space.

In conclusion, it is important in the reconstruction of the phase space to choose the right embedding dimension and time delay. However, for most standard quantities in nonlinear time series analysis the most important parameter is actually the product

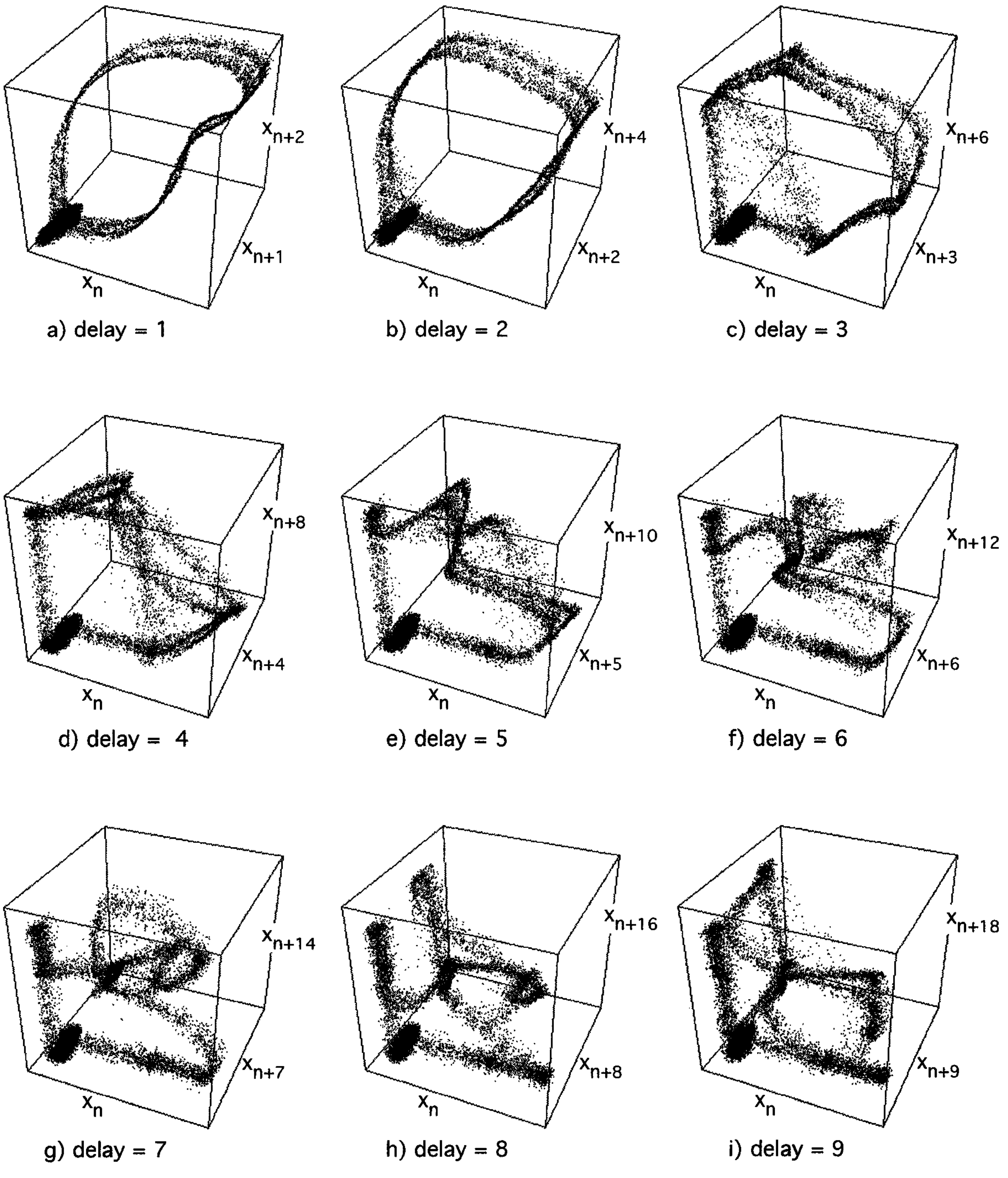

a) delay = 1 b) delay = 2 c) delay = 3

d) delay = 4 e) delay = 5 f) delay = 6

g) delay = 7 h) delay = 8 i) delay = 9

Figure 6.21: Different phase space embeddings of a time series of voltage pulses recorded by the Hall probe when flux tubes flowing along the 1D channel pass the Hall probe's position. The delay was varied from a) 1 to i) 9.

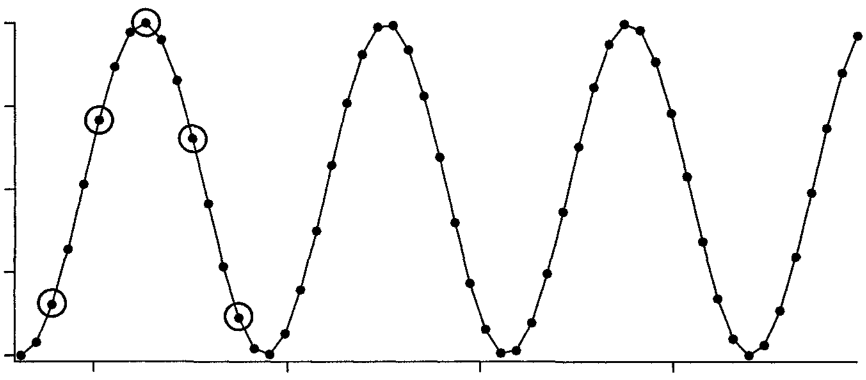

Figure 6.22: A good representation of a pulse as a state in the phase space will be provided by choosing the product $m\nu$ to be 15; this can be realized with $m = 5$ and $\nu = 3$.

$m\nu$ of the embedding dimension m and the time delay ν. This is because $m\nu\Delta t$ is the time spanned by a vector $\mathbf{y}_n$ in the original measurement. In Fig. 6.22 is shown a good choice of the product $m\nu$ for a time series of pulses; with $m\nu = 15$ a single pulse is nicely covered.

Stationarity. Before proceeding to apply nonlinear time series analysis to our data, we have to see if our data are *stationary*. From a statistical point of view, a system is considered to be stationary if the probabilistic structure of the process is conserved under the evolution of the dynamics. If this is not the case, many algorithms used in nonlinear time series analysis such as Lyapunov exponents and correlation dimension could give erroneous results, making the system to look high dimensional even if is not.

Quantitatively, in nonlinear time series analysis, stationarity is tested for by checking for compatibility of nonlinear approximations to the developed dynamics;

this is done for different segments of the tested sequence. This is called the nonlinear cross-prediction test for stationarity [149]. The test looks for possible similarity between the parts of the analyzed time series, rather than the similarity of parameters calculated from the time series by local averages. The (nonlinear) cross-prediction error is the predictability of one segment using another segment as a database. In the next section we will apply this test on different sequences of our time series.

Nonlinearity. After checking the data for stationarity, another fundamental test that must be done before attempting any nonlinear analysis on our data is a test for *nonlinearity.* A good test for this is to compare the original time series with suitable *surrogates* which are known not to be nonlinear. In this surrogate method we first specify a *null hypothesis* that we want to test against. This means that we assume that our data are not nonlinear; a positive test for nonlinearity will prove that our assumption was wrong. The most common null hypothesis is to assume that the data come from a Gaussian linear stochastic process. So, we construct some surrogate data which share certain properties with the original data, but also are consistent with the null hypothesis that we are testing for. For example, to test against the null hypothesis of a linear stochastic process with Gaussian inputs we have to fabricate surrogates sets consisting of random numbers which have the same power spectrum as the original data. This is done by making a phase randomization of the Fourier transform of the original time series. The inverse-Fourier of such modified data are random numbers but have the same power spectrum as the original data because the amplitudes are not changed. Different realizations of phase randomization yield new surrogates.

Once we have a number of surrogate data sets we need to compute some parameter for each of them as well as for the original data. In the TISEAN software package [146] it is recommended to test the null hypothesis by calculating the quantity called *zeroth-order nonlinear prediction error.* This is a locally constant nonlinear prediction used to forecast the progress of the time series one step ahead. The algorithm searches for all neighbors of the point which is forecasted and calculates the image of that point as the average of images of its neighbors. By comparing the forecasted time series with the time series itself, forecast errors are reported. If the prediction error (or whatever parameter we are testing for) is less for the original data than for any of the surrogates, then the null hypothesis is rejected at a confidence level p, $1/p - 1$ being the number of surrogate data sets.

Correlation dimension. The trajectory followed by the system in phase space builds up a particular geometrical object known as *attractor.* The most popular measure of attractor dimension is the **correlation dimension** introduced by Grassber and Procaccia [150, 151]. The concept of correlation dimension reflects how often the system visits different parts of the phase space, and, in this way, tells us something about the attractor's geometry, that is, something about the self-similarity which occurs at different scales in phase space. The correlation dimension only tests points for their spatial interrelations and ignores time correlations. For this reason, particular care should be taken in rejecting the spatial correlations which are due to time proximity.

Let's see how the correlation dimension is calculated. Once we decide on a time delay, the algorithm starts by considering a two-dimensional phase space. A ball of radius ϵ is centered on the first point in phase space, and all the other phase space points lying within the ball are counted. The ball is then centered over the second point, and all the other points within it are again counted. The ball is swept in this way over all the points in phase space, with the number of points within being counted each time. The *total* number of points counted in this way is called the number of *qualifying points*. By normalizing this total sum by the number of points $N(N-1)$ that would have been counted if the ball were of infinite size, we obtain the *correlation sum* for a ball of radius ϵ:

$$C_\epsilon = \frac{\text{number of points within the distance } \epsilon}{N(N-1)}, \tag{6.8}$$

where N is the total number of points in the phase space (i.e., on the trajectory). The next step is to increase ϵ and repeat the above calculation. A larger ball will provide more qualifying points, so the correlation sum will be larger. By systematically enlarging the ball, we finally reach the upper limit 1 for the correlation sum when the ball is so large that all the points on the trajectory are encompassed. The ball-size dependence of the correlation sum is then calculated for different embedding dimensions of the phase space (usually up to ten).

In a vector space, the correlation sum for a collection of points $\mathbf{y}_n$ is defined

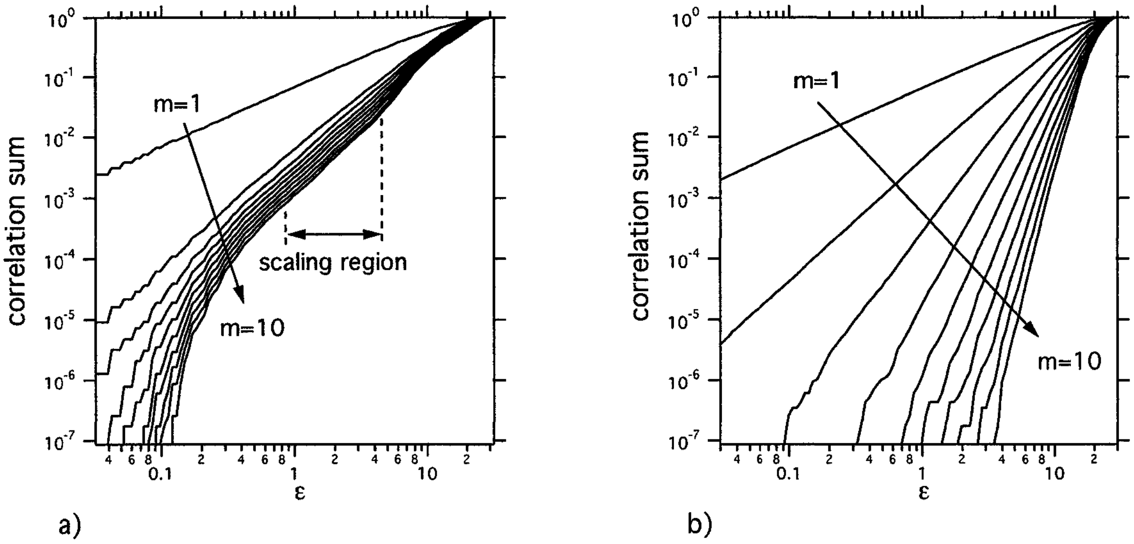

Figure 6.23: Correlation sum for a) chaotic data (Lorentz attractor) and b) stochastic data. Different embedding dimensions from 1 to 10 have been tried.

to be the fraction of all possible pairs of points which are within a given distance ϵ:

$$C_\epsilon = \frac{2}{N(N-1)} \sum_{i=1}^{N} \sum_{j=i+1}^{N} \Theta(\epsilon - \|\mathbf{y}_i - \mathbf{y}_j\|), \tag{6.9}$$

where Θ is the Heaviside step function. The sum just counts the pairs $(\mathbf{y}_i, \mathbf{y}_j)$ whose distance is smaller than ϵ. In the limit of an infinite amount of data ($N \to \infty$) and for small ϵ, we expect the correlation sum C to scale like a power law, $C(\epsilon) \propto \epsilon^D$. In this case, the correlation dimension is defined by:

$$D = \lim_{\epsilon \to 0} \lim_{N \to \infty} \frac{\partial \ln C(\epsilon, N)}{\partial \ln \epsilon}. \tag{6.10}$$

Therefore, in a log-log plot the linear region is evidence for self-similarity.

In Fig. 6.23 we show the correlation sum calculated for both chaotic and stochastic (completely random) data. The chaotic data set is a time series of the

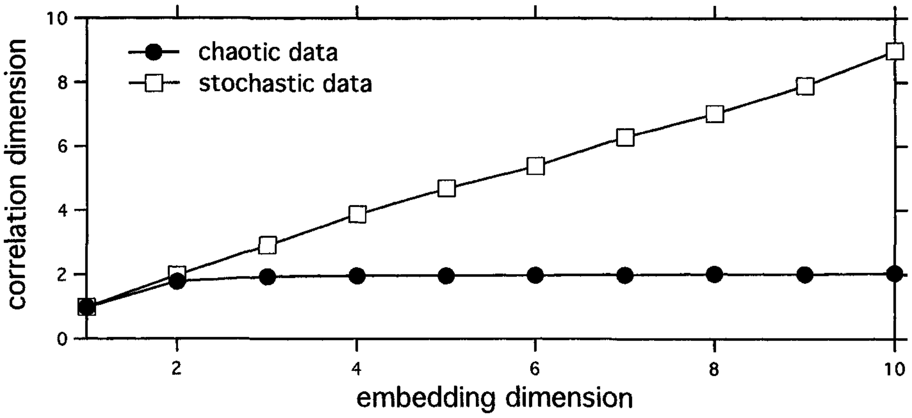

Figure 6.24: Correlation dimension calculated as the slope of the curves shown in Fig. 6.23.

well-known Lorentz attractor and the stochastic data set is just white noise. In both cases, a scaling region can be observed for all the embedding dimensions from 1 to 10. However, only if the slope of the scaling range is going asymptotically to some value as the dimension is increased can this slope be identified as the correlation dimension D. We show in Fig. 6.24 the slope of the scaling region of the curves presented in Fig. 6.23. In the case of the chaotic data, the slope of the correlation sum indeed converges to $D \cong 2$ as the embedding dimension is increased. This is because, in the case of a chaotic attractor, the phase space eventually allows the attractor to fully develop. Conversely, random data continually fill their allowed space as we increase the embedding dimension and the scaling exponent is always equal to the embedding dimension. Consequently, for random data, the slope continues to increase without any tendency to become asymptotic.

Lyapunov exponents. Lyapunov exponents tell us how orbits followed by

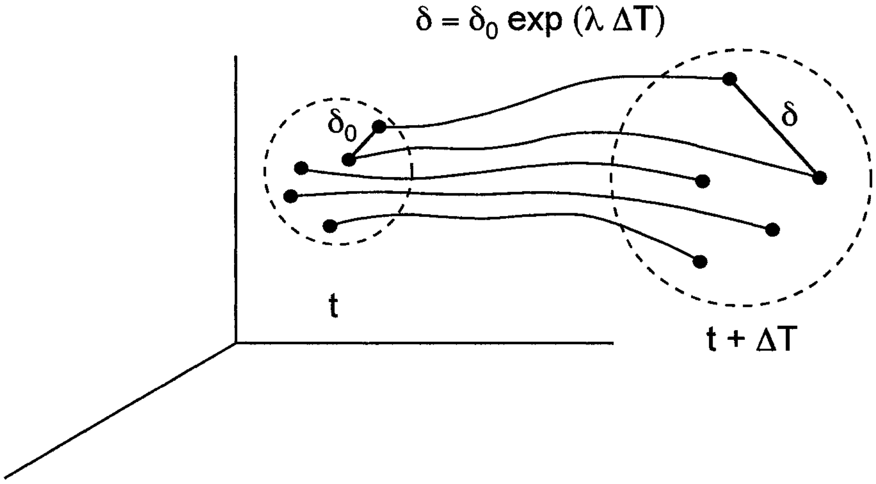

Figure 6.25: In the phase space the nearby trajectories diverge exponentially if the dynamics is chaotic. This is shown by a positive Lyapunov exponent λ.

nearby points in phase space move apart (or together) under the evolution of the dynamics. In the case of a deterministic chaos this separation is exponentially fast. As is shown in Fig. 6.25, *Lyapunov exponent* λ determines the rate of separation; for a chaotic dynamics the largest Lyapunov exponent will be positive. There are actually as many Lyapunov exponents as there are phase space dimensions. However, it is enough that only the largest exponent be positive in order to conclude that the dynamics is chaotic.

To see how Lyapunov exponents can be calculated, let's consider two points very close in the phase space at some given time. They are defined by the time-delayed vectors $\mathbf{y}_n$ and $\mathbf{y}_{n'}$ such that $\|\mathbf{y}_{n'} - \mathbf{y}_n\| = \delta_0 \ll 1$. Thus the two points are far apart in time, and just happen to be nearby in phase space. After Δn steps, the separation between the trajectories emerged from these two points will be $\delta_{\Delta n} =$

$||\mathbf{y}_{n'+\Delta n} - \mathbf{y}_{n+\Delta n}||$. Then, the largest Lyapunov exponent is defined as the exponent λ of this exponential growth:

$$\delta_{\Delta n} \simeq \delta_0 e^{\lambda \Delta n}, \qquad \delta_0 \longrightarrow 0, \qquad \delta_{\Delta n} \ll 1. \tag{6.11}$$

The algorithm used by TISEAN software package for the largest Lyapunov exponent was introduced by Kantz [152] and Rosenstein, Collins, and De Luca [153]. It is a robust algorithm which tests directly for the exponential divergence of nearby trajectories. The algorithm starts by selecting the neighbours within a distance ε with respect to a chosen point $\mathbf{y}_{n_0}$ in the phase space. Then, the average over the distances of all neighbours to the reference point along its trajectory in the phase space is calculated. The logarithm of this average at a time step Δn is an *effective expansion rate* over the time Δn of monitoring the trajectories' divergence. The logarithm contains all the deterministic fluctuations due to the projection and dynamics. Repeating this calculation for very many points n_0, the fluctuations of the effective expansion rate will be averaged out given an effective expansion rate

$$S(\Delta n) = \frac{1}{N} \sum_{n_0=1}^{N} \ln \left(\frac{1}{\mid \mathcal{U}(\mathbf{y}_{n_0}) \mid} \sum_{\mathbf{y}_n \in \mathcal{U}(\mathbf{y}_{n_0})} \mid y_{n_0+\Delta n} - \mathbf{y}_{n+\Delta n} \mid \right), \tag{6.12}$$

where $\mathcal{U}(\mathbf{y}_{n_0})$ is the neighbourhood of $\mathbf{y}_{n_0}$ with diameter ε. Because we don't know either the correct embedding dimension or the optimal distance ε, we calculate the effective expansion rate $S(\Delta n)$ for many values of these two variables. However, the size of neighbourhood is limited below by the noise size and above by the size of the attractor. Fortunately, the Lyapunov exponent is an invariant of the dynamics so it should not be much affected by choosing different dimensions for the phase space. In TISEAN documentation it is stated that "if $S(\Delta n)$ exhibits a linear increase with identical slope for all m larger than some m_0 and for reasonable range of ε, then this slope can be taken as an estimate of the largest Lyapunov exponent." Here, m is the dimension of the phase space.

Nonlinear noise reduction. A very useful preliminary step of a time series analysis is to use a noise reduction algorithm. The effect of noise can be quite significant, impacting:

- *phase reconstruction.* The replacement of the scalar measurements with vectors in the embedding phase-space is strictly valid only for data of infinite resolution. The noise always adds a high-dimensional component.
- *Lyapunov exponents.* Lyapunov exponents show the divergence of nearby trajectories in phase space. This will be bounded (at small scales) by the noise present in the data set. In the presence of noise, nearby trajectories will diverge diffusively (following a power law) rather than exponentially (which is the case of chaotic data).
- *self-similarity.* The self-similarities reflected in the correlation sum are most meaningful on length scales right above the noise level in a chaotic data set. These can be completely broken by noise.

In general, chaotic dynamics is characterized by invariant quantities such as Lyapunov exponents, the correlation dimension, etc., which are sensitive to noise. This is because only over small length scales do these quantities become independent of measurement technique, data processing, and phase space reconstruction method.

A simple nonlinear noise reduction was proposed by Schreiber [154], and this is also used in TISEAN software package. The method is closely related to the zeroth-order nonlinear prediction method described in the paragraph about nonlinearity. Instead of predicting future values, the noise reduction algorithm replaces noisy measurements by cleaner ones, by "predicting" better values. The cleaned values are determined as averages of the middle components of delay vectors selected by a *locally constant nonlinear prediction.* A local averaging reduces the nonlinear noise if it is applied to the central component of delay vectors. The noise will be enhanced if we average the first and last coordinates of delay vectors. This is due to the instabilities which occur in a system exhibiting chaotic dynamics.

6.6.2 TIme SEries ANalysis (TISEAN) applied to flux tube dynamics

In this subsection we present the main results of the nonlinear time series analysis that we performed on our data using the TISEAN software package [146].

Making "dripping" data. For consistency, we illustrate TISEAN analysis applied to the same time series presented in Section 6.5. The raw data consist of a large time sequence of pulses recorded in 1.6 s; there are 16 million points in a such data set, and approximately 640000 pulses. As in the dripping faucet experiment, the relevant dynamical parameter is the time separation between successive pulses. We collected the "dripping" times of our flux tubes dynamics in two ways: either by finding the intersections of the pulses with a given level, or by making Gaussian fits of the pulses and then finding the intersections of the fitted pulses with a given level. We found no significant difference between the two procedures; in this analysis we have used the Gaussian fit. The resulting data set of pulse (or "dripping") times contains 638900 points, corresponding to a current range between 497 mA and 590 mA. In the upper panel of Fig. 6.26 is shown the bifurcation map of dripping time intervals obtained from the Gaussian fit of our time series. This is the same data as shown in Fig. 6.18, though doesn't look as nice as here. This is because in Fig. 6.26 the ΔT time series is plotted as the original raw data, and not histogramed into gray-scale bins as in Fig. 6.18. We considered it unnecessary to again make a histogram plot of the time series, since the region of interest is enlarged enough in the lower panel to make the details visible. The lower panel in Fig. 6.26 is centered on Region I and the non-periodic sequences b) (*chaos_01*), e) (*chaos_02*), and f) (*chaos_03*) mentioned in Section 6.5 are marked explicitly; these sequences will be analyzed extensively in the following.

Phase space reconstruction. The discussion about the phase space reconstruction will be mainly focused on the sequence *chaos_01* which consists of 2000

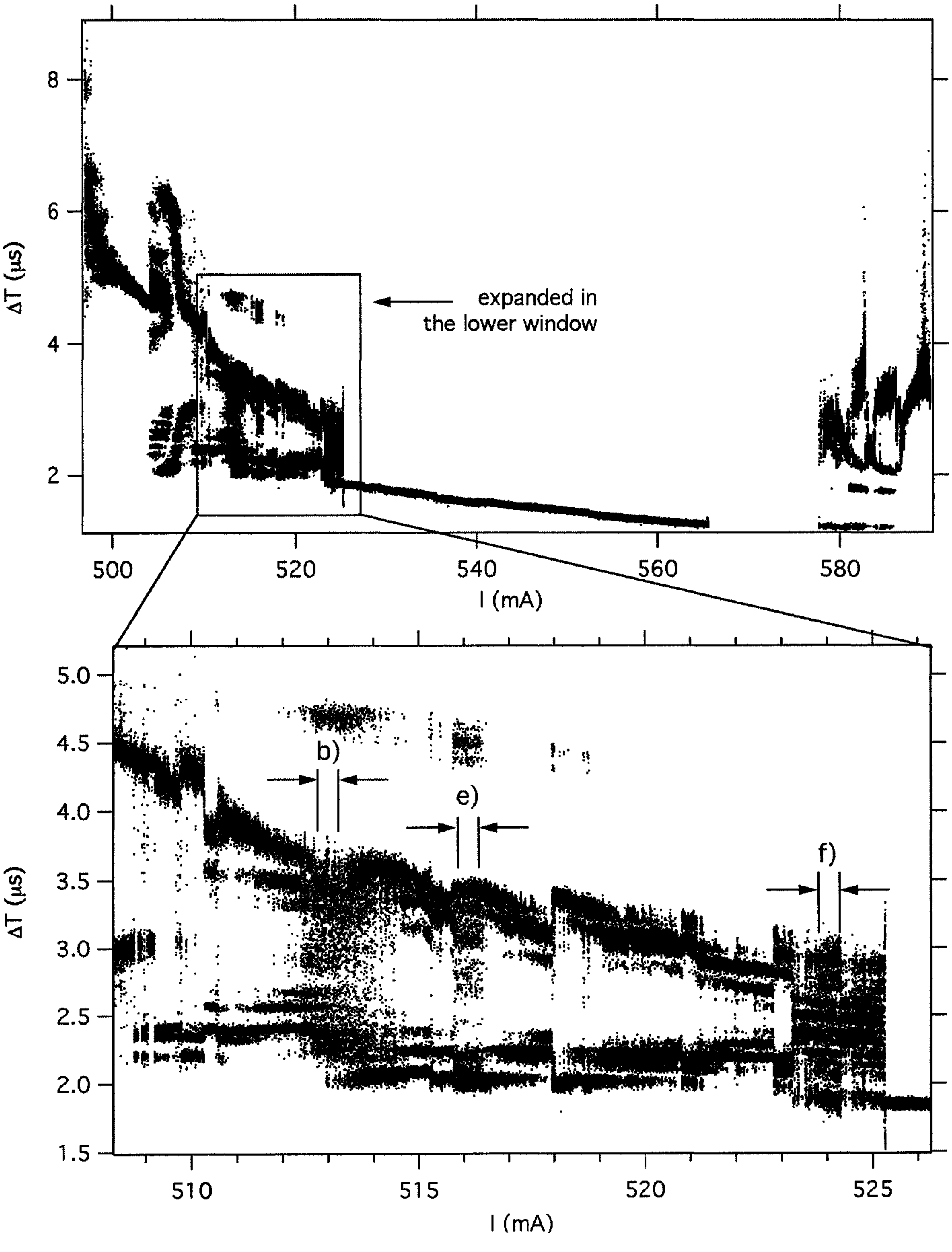

Figure 6.26: Bifurcation map of the dripping time intervals.

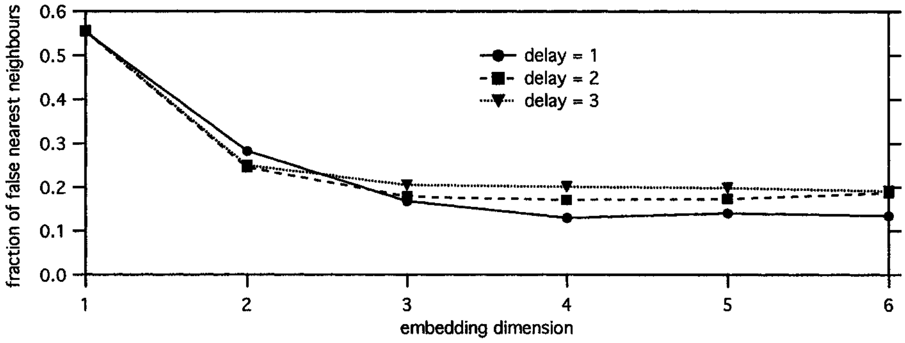

Figure 6.27: Fraction of the false nearest neighbours as a function of the embedding dimension for the sequence *chaos_01*; different time delays have been considered.

points. A practical guideline to determine the dimension of the phase space is the *false nearest neighbour* technique. This method tries to find the phase space which completely unfolds the attractor by removing the intersections between trajectories. Using the *false_nearest* program of TISEAN software package we evaluated the fraction of the false nearest neighbours of *chaos_01*. For each point in the time series, the algorithm looks for the nearest neighbor in a given phase space. Then, both points are iterated one step into the future and the distance between these points before and after the iteration is calculated. If the ratio of these distances exceeds some threshold value (we chose the ratio to be 5), the point is marked as having a "false nearest neighbor." This means that the two points appear to be close to each other only because the phase space doesn't have enough dimensions to unfold the attractor's structure. By increasing the embedding dimension, the false nearest neighbors due to low dimensionality are quickly removed in the phase space.

The embedding dimension is considered high enough if the fraction of points

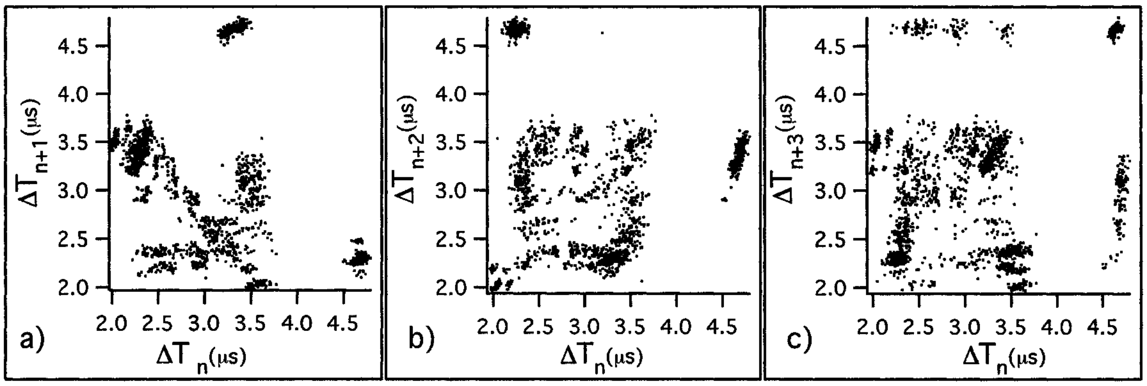

Figure 6.28: The first three return maps of the sequence *chaos_01*.

having false neighbors drops to a small value. In Fig. 6.27 we can see that, as the embedding dimension is increased, the fraction of the false nearest neighbours declines to a constant value for an embedding dimension of 3 (0.17 for a delay of 1). Therefore, we have chosen an embedding dimension $m = 3$ for the phase space reconstruction and subsequent nonlinear analysis.

Having chosen a suitable value for m, we now wish to optimize the delay ν. From the return maps shown in Fig. 6.28 we can see that a good unfolding already occurs for an increment of one (Fig. 6.28a). An increment of three (Fig. 6.28c) appears too large, spreading the points out over the whole area. Though this is done in two dimensions, it gives us a some confidence in choosing the time delay for higher dimensions.

Overall, a natural choice in choosing the time delay to be one (in the phase space of ΔTs) in our case follows from the way in which we processed the data. From

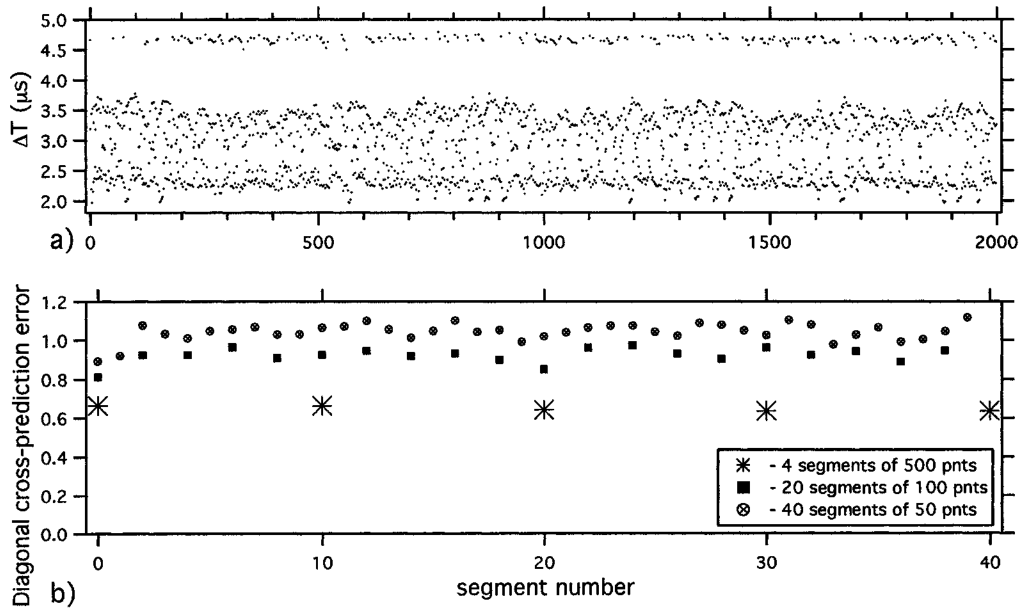

Figure 6.29: The sequence *chaos_01*: a) time intervals; b) diagonal cross-prediction errors.

the recorded time series we selected the time intervals ΔT between successive *pulses*. This eliminates the shape of pulses and the correlation due to them in the time series that we analyze now.

Stationarity. We used the *nstat_z* TISEAN program to test the selected sequences *chaos_01*, *chaos_02*, and *chaos_03* from Region I for stationarity. The program divides the data set into a number of adjacent segments S_i and uses a locally constant approximation to the dynamics (as for prediction or noise reduction) to make a one-step prediction into future for each segment. The nonlinear cross-prediction error $\gamma(S_i, S_j)$ is then the root-mean-squared prediction of the segment S_j evaluated by using the segment S_i as a data base [149].

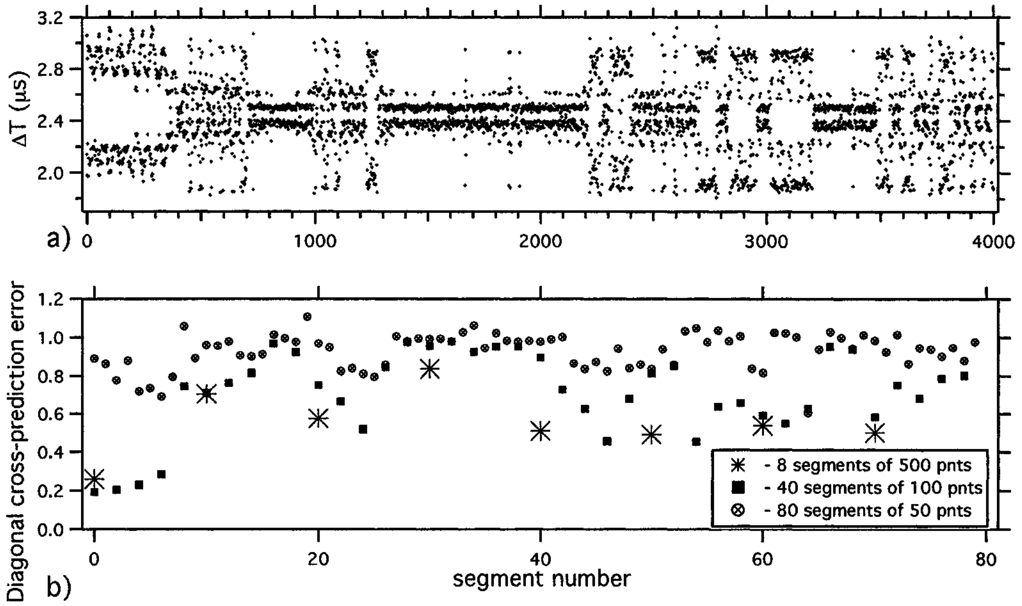

Figure 6.30: The sequence *transient*: a) time intervals; b) diagonal cross-prediction errors.

In Fig. 6.29 and Fig. 6.30 there are shown the diagonal cross-prediction errors $\gamma(S_i, S_j)$ for two very different data sets, *chaos_01* (Fig. 6.29), and a quite nonstationary sequence from Region I (Fig. 6.30); we'll call this second one the *transient* sequence. These sequences are shown in Fig. 6.29a and Fig. 6.30a. We divided each sequence in segments of 500, 100, and 50 points, and calculated the diagonal cross-prediction errors in each case. What we can see is that for the sequence *chaos_01* there are no significant fluctuations in the cross-prediction error (Fig. 6.29b) from segment to segment. Each segment is much like the others; this is what *stationarity* means. However, for the *transient* sequence there are large fluctuations from segment to segment. We observe that these fluctuations are washed out as we decrease the number of points per segment. But this is the key point: even if we consider the dynamics as stationary over a small scale (e.g. segments of 50 points), this doesn't help us very much in calculating other parameters like Lyapunov exponents or correlation dimension for which we need large data sets.

Based on this stationarity test we found the above-mentioned sequences *chaos_01*, *chaos_02*, and *chaos_03* from Region I to be *stationary* and large enough to allow us a more advanced nonlinear time series analysis (Lyapunov exponents, correlation dimension, etc).

Nonlinearity. To test our sequences *chaos_01*, *chaos_02*, and *chaos_03* for nonlinearity we used the null hypothesis method described in the preceding subsection. For the sequence *chaos_01* we fabricated nineteen surrogates, making the null hypothesis that the data has been created by a stationary Gaussian linear process.

To make the surrogates we used the TISEAN program *surrogates* which first makes a FFT (Fast Fourier Transform) of the real data, then randomizes the phases (keeping the same Fourier amplitudes), and finally inverts the FFT, creating the surrogate. In this way, the surrogate data will have the same power spectrum as the original data, but are otherwise random. Then we used the TISEAN *predict* program to calculated the root-mean-squared prediction error for the original data (*chaos_01*) and its surrogates.

As was explained in the previous subsection, the program forecasts one step ahead the progress of the time series. For that, it is used the locally constant nonlinear

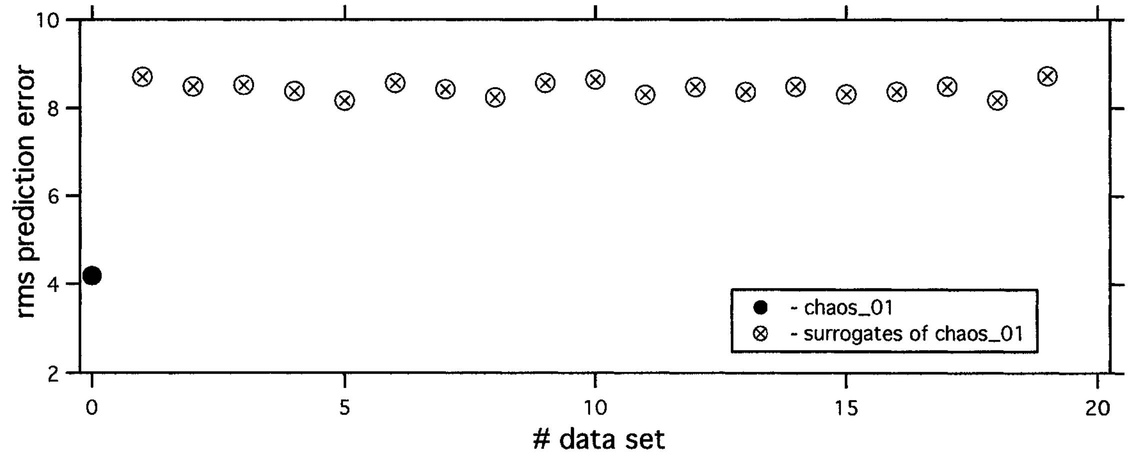

Figure 6.31: Nonlinear test for the sequence *chaos_01*.

prediction by considering the points from nearest neighbourhood of each point. We extended this neighbourhood up to 10 percent of the sequence *chaos_01*'s standard deviation in a 3D phase space. The root-mean-squared prediction error was found to be much smaller for *chaos_01* than for any of its surrogates (see Fig. 6.31). In this case, the null hypothesis was rejected at a confidence level of p=1/(19-1)=0.05.

To prove that this test for nonlinearity is not trivial, a completely random data set was fabricated (2000 points). Then using the same TISEAN program for surrogates, we generated nineteen surrogate data sets for the noise data. In Fig. 6.32 we can see very clearly that the root-mean-squared prediction error of noise data set is comparable with those of its surrogates. The null hypothesis is rejected only at a level of p=1/(6-1)=0.2, which is way too large to argue for nonlinearity in this case. In general, it is considered not acceptable if more than one result of twenty is wrong;

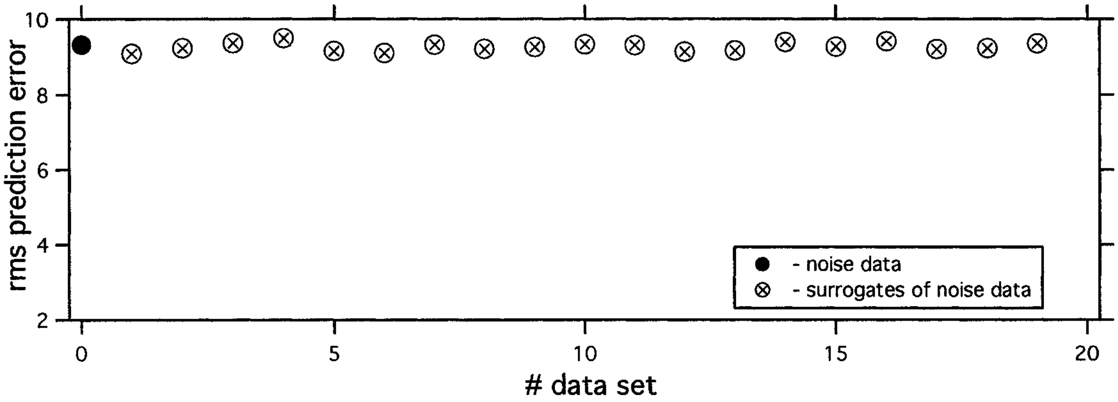

Figure 6.32: Nonlinear test for a noisy (completely stochastic) sequence.

in this example we got 13 wrong results of nineteen.

Correlation dimension. Before proceeding to calculate the correlation sum, we have to consider if our time series suffers from time correlations and, if so, discard the unwanted temporal neighbours. In the phase space, two points could be close not because of the attractor geometry, but due to the continuous time evolution; they are nearby in time. For analysis we keep points that are close in the phase space but not close in time. The problem of time correlations was solved by Provenzale *et al.*[155] who introduced the **space-time separation plot**. In such a plot we consider the number of pairs of points from the phase space as a function of time separation Δt and space distance ε between the points which make these pairs. The time separation Δt is the incremental step which moves us from point to point along the trajectory in the phase space.

The TISEAN program *stp* calculates an accumulated histogram of the spatial

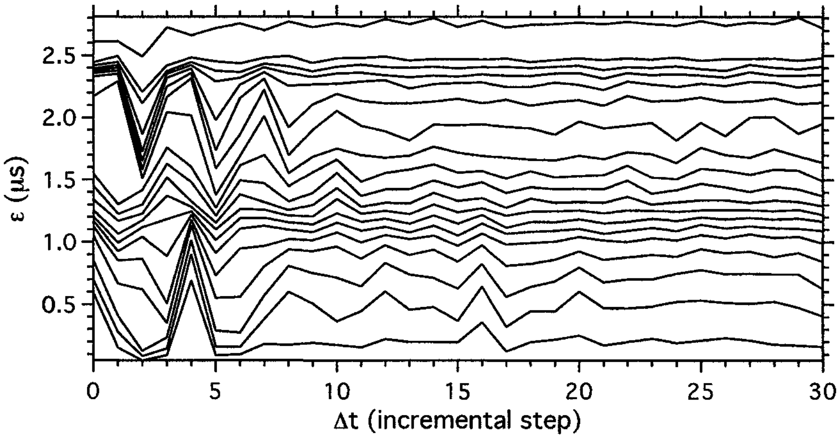

Figure 6.33: Space-time separation plot for the sequence *chaos_01*. Contour lines (from below) correspond to 0.05, 0.10, 0.15, ... fraction of pairs that have been found at given time separation and space distance.

distances ε for each time separation Δt. Therefore, the space-time separation plot consists of contour lines, each line being a percent level (10 percent, 20 percent etc.) of pairs with a given time separation Δt. From the time-space separation plot of the sequence *chaos_01* (Fig. 6.33) we can see that the contour lines are flat for time separations larger than 10 (10 incremental steps). This means that for $\Delta t > 10$ the neighbourhood configuration in the phase space is due to the dynamics, not to the time proximity. In estimating the correlation dimension and Lyapunov exponents we will be safe in discarding pairs of points which are closer more than 10 incremental steps. In the specific language of nonlinear time series analysis this is referred as a *Theiler window* [156] of 10.

Using the TISEAN program *d2*, the correlation sum $C(m, \varepsilon)$ was calculated as a function of spatial separation ε for the sequence *chaos_01* with a delay of 1, a

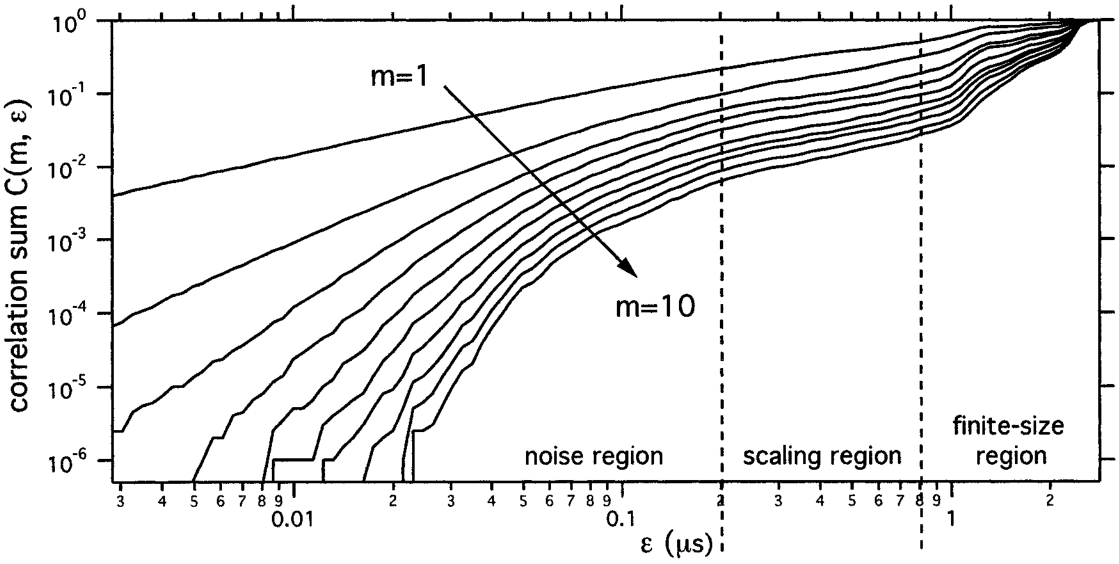

Figure 6.34: Correlation sum for the sequence *chaos_01* with the embedding dimension varied from 1 (upper curve) to 10 (lower curve).

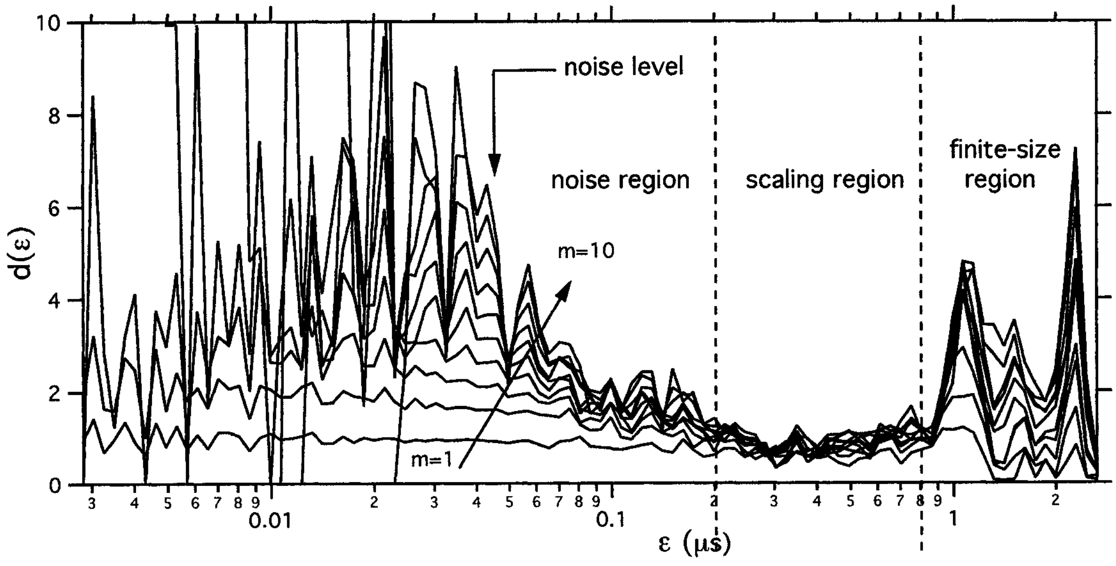

Figure 6.35: The slope of correlation sum for the sequence *chaos_01* with the embedding dimension varied from 1 (lower curve) to 10 (upper curve).

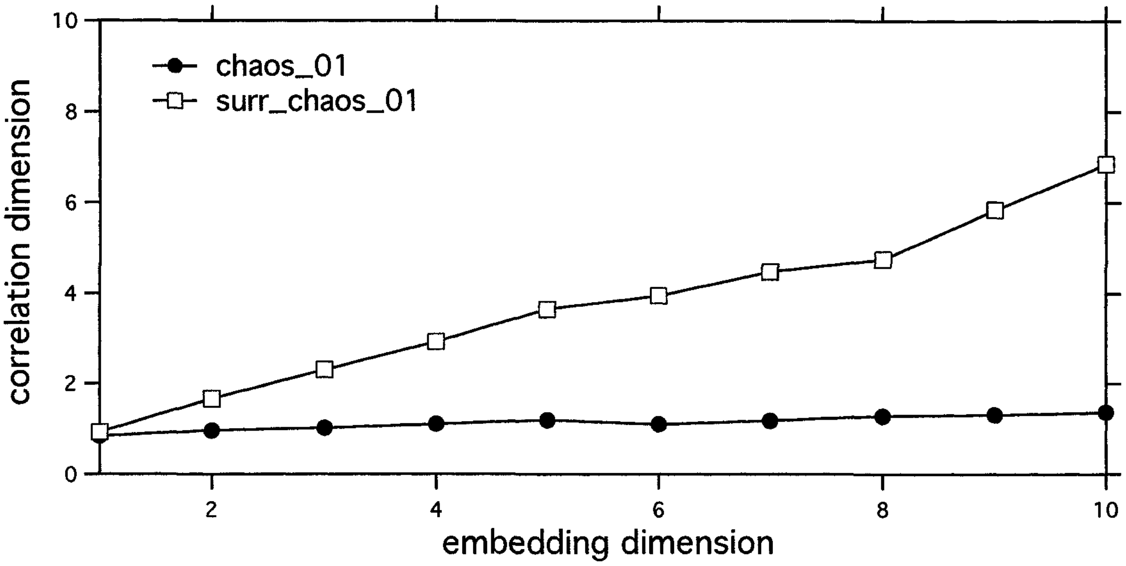

Figure 6.36: Correlation dimension versus embedding dimension for the sequence *chaos_01* and one of its surrogate.

Theiler window of 10, and embedding dimensions m from 1 to 10 (Fig. 6.34). We can identify a clear scaling region for ε between 0.2 and 0.8 μs, and, importantly, the slope in this region is independent of the embedding dimension. As the embedding dimension m is increased, the correlation sum $C(m, \varepsilon)$ saturates asymptotically but preserves the slope of the linear region. Therefore, it's appropriate to identify the correlation dimension D with the slope of this region, which is about 1.2–1.3. This is the scaling region over which we can say the attractor shows its self-similarity. There is only a slight shrinking of this linear region with the increase of the embedding dimension.

For ε smaller than 0.1 μs the correlation sum changes its slope continuously;

this is inside the noise region. Below the noise level the data are smeared out over the entire available space, which increases with the embedding dimension m. Consequently, the slope becomes steeper and steeper as m is increased and, at the noise level, the slope equals the embedding dimension m. At the other extreme, where ε is larger than 1 μs, a different behavior is displayed. Now, the disappearance of the scaling region is due to the finite size of the attractor, as we can see from the definition of the correlation sum.

The three regions just discussed are even more evident in Fig. 6.35, where we plot the slope of correlation sum curves shown in Fig. 6.34. The slope of the correlation over the scaling region as a function of the embedding dimension is shown in Fig. 6.36 for the sequence *chaos_01* and for one of its surrogate. The correlation dimension for the sequence *chaos_01* goes asymptotically to $D = 1.3$ as the embedding dimension is increased, whereas for the surrogate data the correlation dimension increases almost linearly without any sign of a saturation.

Because deterministic signals and noise scale differently with distance in phase space, we can use the correlation algorithm to evaluate the noise level present in our data. As we observed above, the scaling exponent (due to the deterministic part) is independent of the phase space dimension, $d(m,\varepsilon) \approx D$. However, in the noise region the scaling exponent is actually the embedding dimension, $d(m,\varepsilon) \approx m$. It has been shown [157] that the correlation sums $C(m,\varepsilon)$ and $C(m+1,\varepsilon)$, calculated for two consecutive embedding dimensions m and $m+1$, differ through the correlation sum

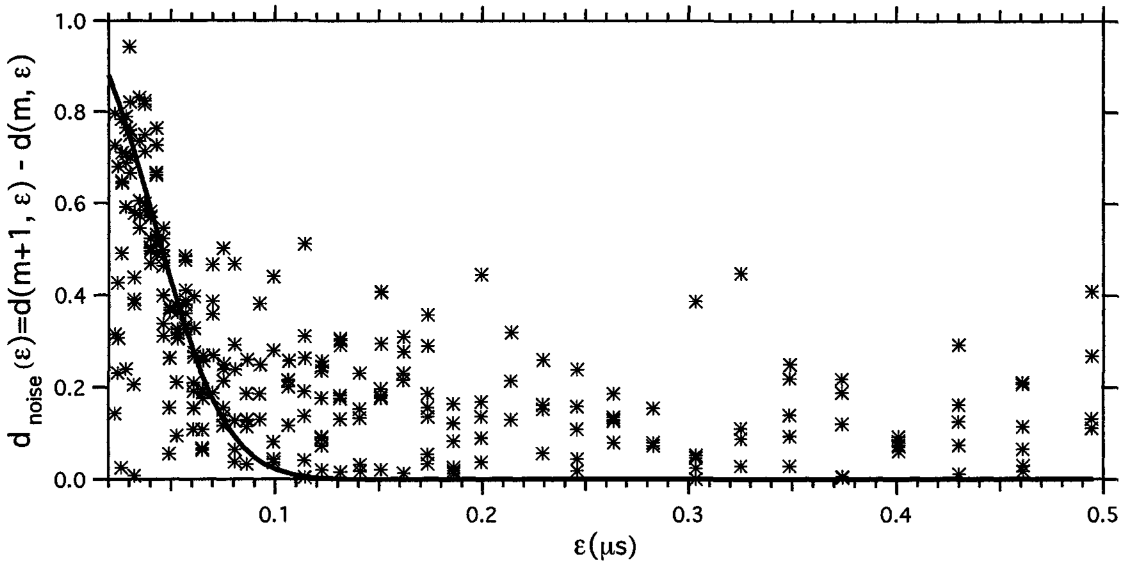

Figure 6.37: The difference between the scaling exponents as a function of the spatial separation.

of the one-dimensional distribution of noise $C(\varepsilon)$:

$$C(m+1,\varepsilon) \propto C(m,\varepsilon)C_{\text{noise}}(\varepsilon). \tag{6.13}$$

Considering a Gaussian distribution for noise, $C_{\text{noise}}(\varepsilon) \propto \text{erf}(\varepsilon/2\sigma)$, the scaling exponent for the noise region will be [158]:

$$d_{\text{Gauss}}(\varepsilon) = d(m+1,\varepsilon) - d(m,\varepsilon) = \frac{\varepsilon\exp(-\varepsilon^2/4\sigma^2)}{\sigma\sqrt{\pi}\,\text{erf}(\varepsilon/2\sigma)}, \tag{6.14}$$

where σ is the amplitude of the Gaussian noise. The differences $d(m+1,\varepsilon) - d(m,\varepsilon)$ (for m=1,..., 9) are ploted in Fig. 6.37. The solid line is a visual fit with $d_{\text{Gauss}}(\varepsilon)$ for $\sigma = 0.023$ μs. Though there are some fluctuations due to the non-Gaussian part of the noise, we can estimate the noise level present in our data as being about $2\sigma = 0.046$ μs.

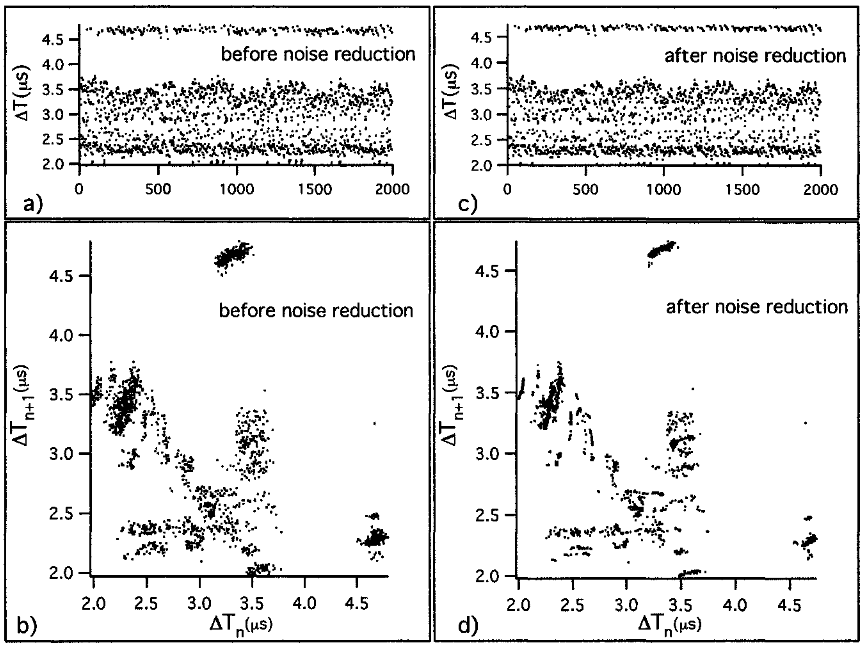

Figure 6.38: Nonlinear noise reduction for the sequence *chaos_01*.

We see in Fig. 6.34 and Fig. 6.35 that the fluctuations are really large below 0.04 μs. However, this Gaussian level noise is significantly below what we identified as the noise region. Probably, between 0.04 μs and 0.2 μs other non-Gaussian noise occurs.

Nonlinear noise reduction. We performed a noise reduction of our time series with the TISEAN program *nrlazy*. The nonlinear noise reduction algorithm used by this program was described in the previous section. Here we illustrate the simple nonlinear reduction on the sequence *chaos_01* (see Fig. 6.38). The following parameters have been used for *nrlazy* program: embedding dimension 3, delay 1, and neighbourhood size 0.08 μs. For the local averaging in the noise reduction program it is recommended to choose a neighbourhood size about twice the noise level. Having

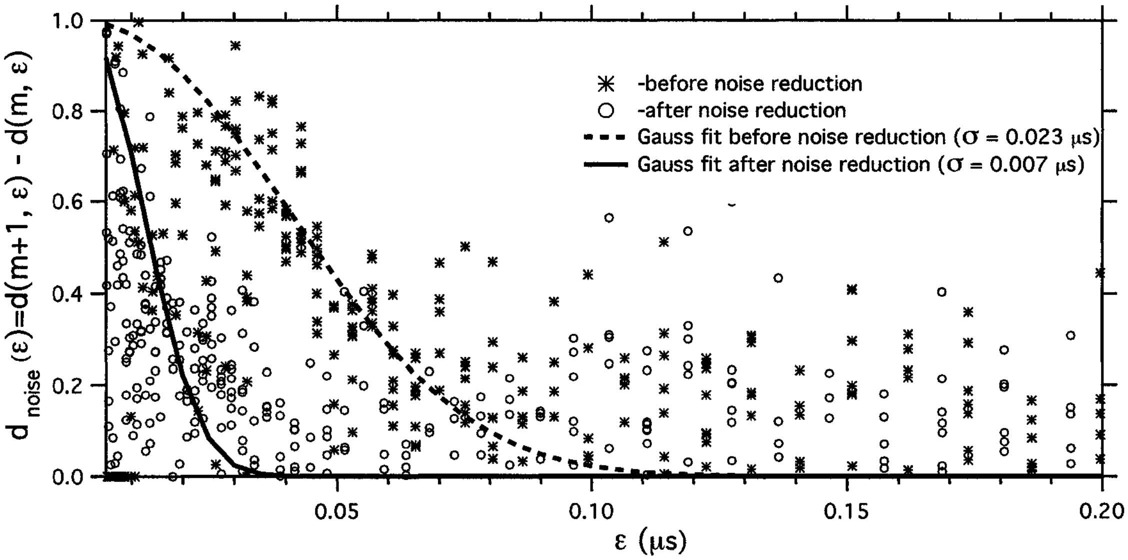

Figure 6.39: Estimation of the Gaussian noise level for the sequence *chaos_01* before and after noise reduction.

an estimated noise level of 0.046 μs (with the correlation algorithm) for the sequence *chaos_01* we tried values around 0.08 μs for the neighbourhood size. In Fig. 6.38a and c we show the bifurcation map of the sequence *chaos_01* before and after noise reduction. Though there is not an obvious difference between them, in their corresponding return maps we can clearly see the improvement, as shown in Fig. 6.38b (before noise reduction) and Fig. 6.38d (after noise reduction).

A quantitative estimation of the noise level after the noise reduction was done by using the correlation algorithm, and approximate the remaining noise with a Gaussian distribution. Again, this is not quite exact but leads to an estimate of the noise level. In Fig. 6.39 it is shown that, indeed, the Gaussian noise amplitude was reduced

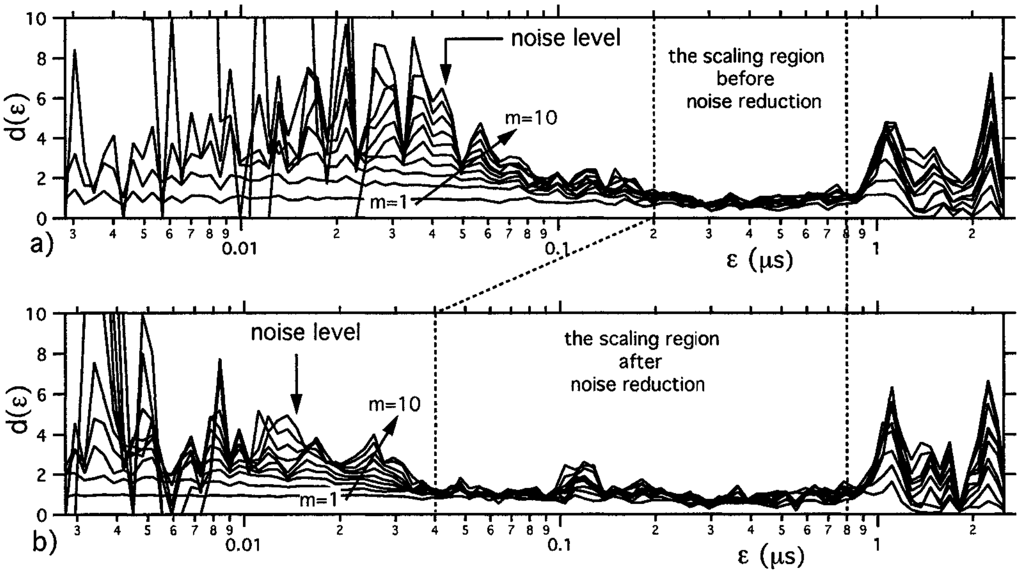

Figure 6.40: The slope of the correlation sum for the sequence *chaos_01* as a function of spatial distance: a) before noise reduction (the same as in Fig. 6.35); b) after noise reduction. In each panel m goes from 1 (lower curve) to 10 (upper curve).

from 0.023 to 0.007 μs. This improvement is observed also in the scaling region of the correlation sum. In Fig. 6.40 we can see that the scaling region was extended down from 0.2 to 0.04 μs, a quite non-trivial improvement. Of course, at large spatial distances (1–2 μs) there is not any change because this is in the finite-size region.

Lyapunov exponents. The TISEAN software package provides two programs for calculating the largest Lyapunov exponent, although both use the same basic algorithm. We used the *lyap_k* program which offers more freedom in adjusting its parameters; the algorithm of the *lyap_k* program is described in [152]. These parameters are the delay (we used a delay of 1), the embedding dimension of the phase space, the length scale over the program is searching for divergence, the number of iterations, and the Theiler window (10 is enough for our data). We also have the possibility to vary the embedding dimension. This should not affect the scaling region, since Lyapunov exponents are invariant parameters of the dynamics. Because the previous analysis established a good embedding around of 3, we tried embedding dimension from 2 to 5. Regarding the length scale over which we should look for exponential divergence between trajectories, it doesn't make sense to go below the noise level. We established that for the sequence *chaos_01* the noise amplitude is 0.023 μs before noise reduction and 0.007 μs after noise reduction.

For consistency, let's analyze the same sequence *chaos_01*. In Fig. 6.41 is shown the logarithm of the average expansion rate for trajectories in phase space, considering different embedding dimensions. In such a plot, a linear region indicates an exponential divergence between phase space trajectories which initially are close to each other. The slope of linear region can be identified with the largest Lyapunov exponent. In Fig. 6.41 we have two set of curves: the dashed ones are calculated before noise reduction, the solid ones after noise reduction. Clearly, a substantial improvement is made by the noise reduction. Mostly, the effect of noise in the Lyapunov exponent calculation is a steep initial divergence of the expansion rate. All the dashed curves in Fig. 6.41 exhibit this behavior for distances less than the noise level ($\ln 0.023 = -3.77$); it is not possible to identify a good linear region. By making a noise reduction an extended region of the exponential divergence is obtained for the average expansion rate (solid curves in Fig. 6.41), the noise level being now

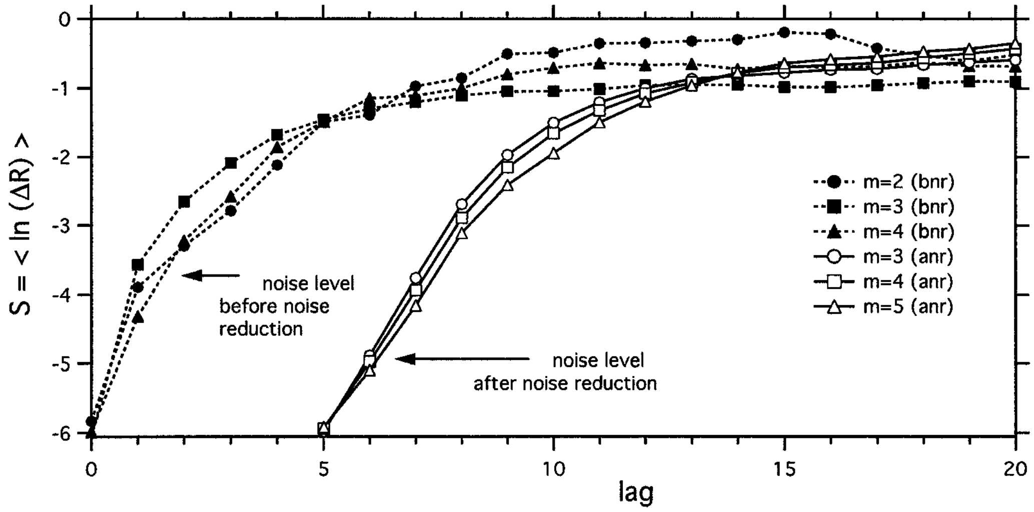

Figure 6.41: The logarithm of the average expansion rate in the phase space for the sequence *chaos_01*. Here "bnr" stays for "before noise reduction" and "anr" means "after noise reduction". The curves "anr" are shifted to right by 5 units for clarity. The lag is the increment along the phase-space trajectory.

$\ln 0.007 = -4.96$. Now, the slope is nearly the same (≈ 1) for different embedding dimensions (3, 4, and 5) because, again, the Lyapunov exponents are invariant parameters of the dynamics.

In Fig. 6.41, the solid curves (after noise reduction) are successively shifted to right by five units in order to have a better visualization. Above the noise level, the average expansion rate will expand exponentially (the linear region) and after that will go asymptotically to a value given by the size of attractor. Roughly, this is the standard deviation of distances between all pairs of points in the phase space.

Using the same program *lyap_k* (with delay 1, embedding dimension 3), we calculated the largest Lyapunov exponent for the three sequences (*chaos_01*, *chaos_02*,

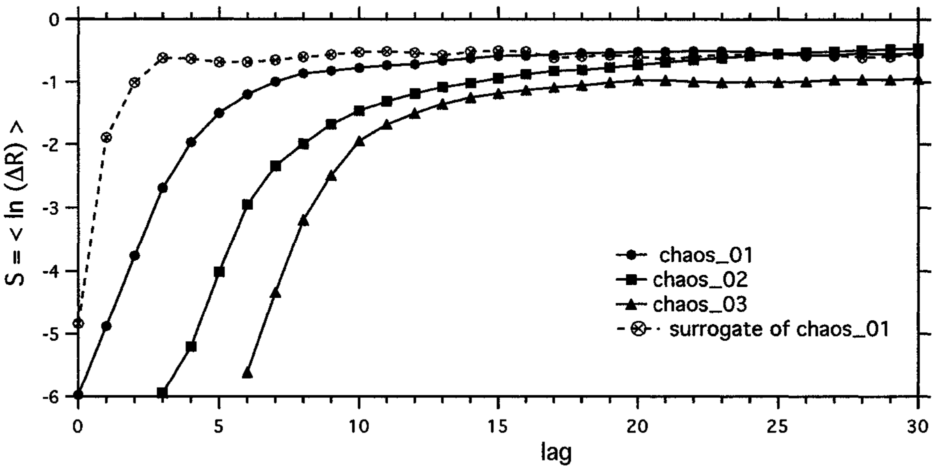

Figure 6.42: The logarithm of the average expansion rate in the phase space for the sequences *chaos_01* and its surrogate, *chaos_02*, and *chaos_03*. The curves *chaos_02* and *chaos_03* are shifted to right by 3 and 6 units for clarity.

and *chaos_03*) from Region I. Each of these sequences has 2000 points and was tested as being both stationary and nonlinear. The noise reduction was applied to each sequence before to calculate the largest Lyapunov exponent. This improved quite a lot our analysis. Thus, above the level of the remained noise, the average expansion rate in the phase space exhibits a clear linear region for each of these sequences (see Fig. 6.42). This distinctive linear region indicates the presence of deterministic behavior in the dynamics, since the slope of the linear range is the largest Lyapunov exponent. The second and third solid curves are shifted to right by three and six units, respectively, in order to have a better visualization. What we can see in Fig. 6.42 is that the largest Lyapunov exponent has almost the same value for each sequence. This might be due to the fact that each sequence comes after a periodic one and, consequently, the attractor shows similar development. The dashed curve is calculated for one of the surrogate data of the sequence *chaos_01*. In this case, the slope of the average expansion rate is almost vertical, indicating a stochastic data. This tells us that, indeed, our original data are deterministic, exhibiting a positive signature of exponential trajectory divergence in the phase space.

6.7 Current-Driven Flux Tube Model

Here we propose a model to describe the observed dynamics in terms of the nucleation of flux tubes near the sample's edges.

At low driving currents, the strip is in the Meissner state. As the magnetic field due to the current achieves the value of the critical field at the sample's edges, the sample enters a thermodynamically metastable state for which it is energetically favorable to have flux tubes inside the sample. This is the beginning of the Region I: flux tubes start to grow up and detach from the edge. There is a Gibbs free-energy barrier against the generation of a flux tube and its subsequent motion inside the sample. The height of this barrier is proportional to the flux amount carried by the nucleated flux tube [159]. The nucleation (i.e., the growth and detachment) of a flux tube from the sample edge changes the condition for the next flux tube entry into channel. This is because each nucleated flux tube can contain a different amount of flux, and thus modifies through its magnetic field the nucleation condition for the next flux tube entry.

For example, the magnetic field of a just-nucleated flux tube locally weakens

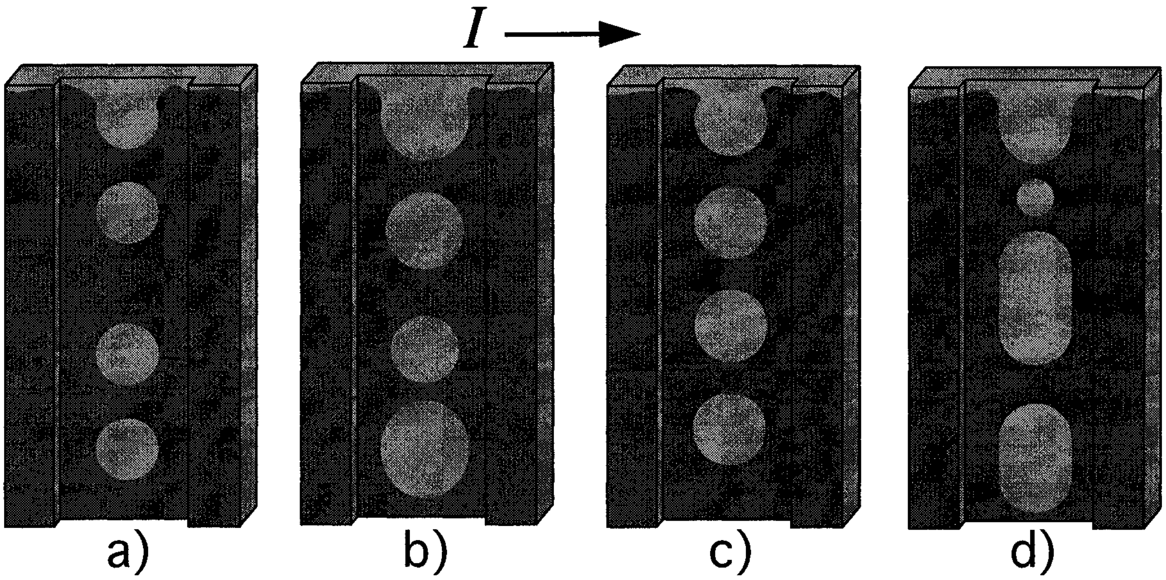

Figure 6.43: Flux-tube nucleation from the edge in the current-driven flux tube model: a) and b) are the period-two and chaotic sequences from Region I, c) sequence from Region II, d) sequence from Region III.

the magnetic field at the sample's edges. Consequently, only a flux tube containing a slightly smaller amount of flux is allowed to nucleate because the Gibbs free-energy is now higher. After this second flux tube nucleates, its influence on the magnetic field at the sample's edge will be lower. Thus the Gibbs free-energy barrier will again be lower, so that the third nucleated tube will have a larger amount of flux, and so forth. In this way, as in the dripping faucet experiment, for each tube the "dripping" time and the amount of flux are determined in part by the previous nucleated flux tube or tubes. Advances and delays of the flux tube nucleation onset come in a complex fashion and determine the "dripping faucet" behavior of Region I. In Fig. 6.43 are shown schematic drawings of the current-driven flux tube model for the two sequences observed in Region I: a) period-two, and b) chaos. The letters are assigned to the same sequences mentioned before in Fig. 6.17.

In the above proposed scenario, in Region I the flux amounts and the distances between flux tubes are continuously adjusted throughout the nucleation process. This allows evolution from periodic to chaotic dynamics. The beginning of the periodic Region II, however, occurs when the flux tubes become locked in a *collective* interacting mode. There is no more room for flux adjustments: each flux tube feels the same interaction so that there is no more change in either pulse shape (flux amount) or time of appearance. Consequently, an average uniform field is created along the channel, and this determines a constant edge barrier for flux tube nucleation at the channel edge. The nucleation condition is the same for all the flux tubes and each flux tube carries the same flux amount. Region II thus exhibits a highly periodic dynamics. A representative drawing for flux tube nucleation in the Region II is presented in Fig. 6.43c.

Experimentally, Region II has been observed to begin at a driving current $I_1 =$ 525 mA, with a corresponding frequency of flux tube motion $\nu_1 = 540$ kHz. Modeling the flux tube train along the channel as a periodic array in equilibrium we can use a flux tube model [6] to estimate the diameter and separation between the flux tubes. We assume that this model, although developed for the equilibrium static case, is still valid at this point when the flux tubes are well separated. Then Ref. [6] gives, for a type-I film of thickness d, the diameter of a flux tube as

$$D = \sqrt{\frac{2\delta d}{(1-h)(1-\sqrt{h})}}, \tag{6.15}$$

and the space between adjacent flux tubes as

$$a = D/\sqrt{h}, \tag{6.16}$$

where $h = H/H_c$ is the reduced magnetic field (the ratio between the applied field and the critical field above which the sample becomes normal). In the above equations $\delta = \xi - \lambda$ is the wall-energy parameter given by the difference between the coherence length and London penetration depth. In general, the wall-energy parameter depends on temperature as [160]

$$\delta(T) = \delta_0/\sqrt{1 - T/T_c}, \tag{6.17}$$

where δ_0 is the wall-energy parameter at zero temperature. For lead, $\delta_0 = 60$ nm, and with $T_c = 7.1$ K (the measured critical temperature of our lead samples) we have $\delta = 100$ nm at 4.50 K. The field in a flux tube is equal to the critical field of the material; at 4.5 K the critical field for lead is 481.6 G. Assuming that the reduced magnetic field at the beginning of Region II is the same as the ratio between the current $I_1 = 525$ mA and the current at which the strip becomes normal $I_n = 804.5$ mA, we have $h_1 = 0.65$. With these numbers, for a 4 μm thick lead film, the diameter of flux tubes and separation between them can be estimated from Eq. 6.15 to be $D_1 = 3.4$ μm and $a_1 = 4.25$ μm at the beginning of Region II. The velocity at which the flux tubes are moving is then $v_1 = a_1\nu_1 = 230$ cm/s. A schematic of this dynamical situation for

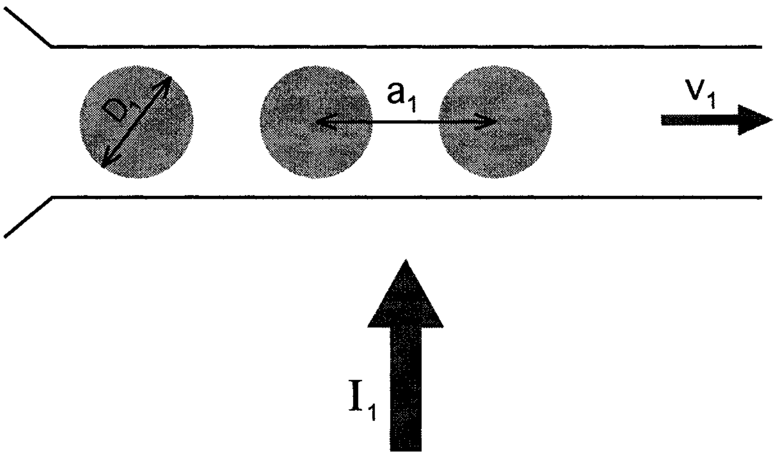

Figure 6.44: Flux tubes moving at low frequency at the beginning of Region II.

the flux tubes at the beginning of the Region II is depicted in Fig. 6.44.

During the periodic Region II, as the driving current was further increased, a slow shift to higher frequencies was observed. This is the result of speeding up of the flux tubes flow due to the current increase. Also, a small reduction in the number of flux quanta per tube was observed. At the end of Region II, the flux tubes are touching (see Fig. 6.45). At this point we have measured a frequency of $\nu_2 = 806.4$ kHz and the driving current was $I_2 = 565.5$ mA. Because now the flux tubes are almost touching, the model used above to estimate the flow parameters probably ceases to be valid. However, we can relate the velocity of the flux tubes at the end of Region II to the velocity at the beginning of this region by considering the ratio of the currents at the beginning and the end of this region.

To do so, we know that after nucleation the flux-tube motion occurs under the influence of the Lorentz force $\mathbf{j}\Phi/c$, being retarded only by the damping force

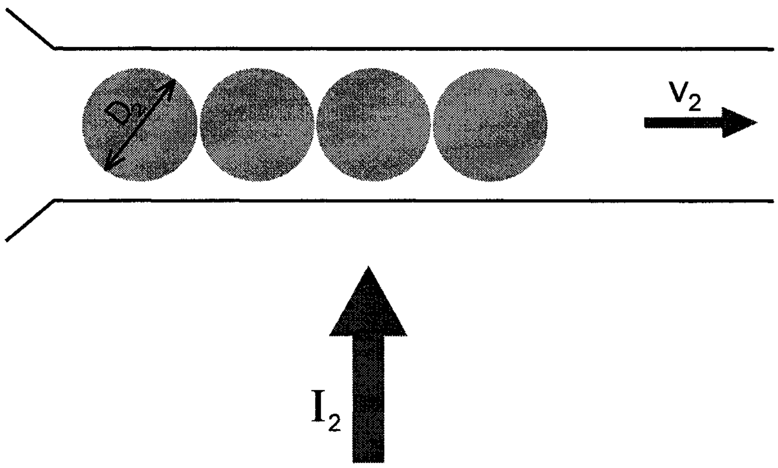

Figure 6.45: Flux tubes moving at high frequency at the end of the Region II.

$-\eta\mathbf{v}$; both these forces are per unit length of the flux tube moving with the velocity $\mathbf{v}$. Forces also act on a flux tube from adjacent flux tubes, but these cancel out each other due to symmetry. By equating the Lorentz force to the damping force, we have then the average flux-flow velocity

$$v = \frac{1}{\eta} j \frac{\Phi}{c}, \tag{6.18}$$

where $\Phi = N\Phi_0$ is the flux amount per tube. The viscous drag coefficient η for the flux-tubes motion has been shown to be given by [133]

$$\eta = \sigma_n \Phi H_c / c^2. \tag{6.19}$$

Combining Eqs. 6.18 and 6.19, we find that the flux-tube velocity is

$$v = \frac{cj}{\sigma_n H_c}. \tag{6.20}$$

Thus the flux-tube velocity is proportional to the applied current. We can write now the flux-tube velocity at the end of Region II as $v_2 = v_1 I_2 / I_1 = 247$ cm/s. Because the flux tubes are touching, the diameter of a flux tube is equal to the distance between their centers, so $D_2 = v_2/\nu_2$. Knowing the velocity and the frequency, we estimated the diameter of the flux tube at the end of the Region II to be about 3.0 μm.

The number of flux quanta per tube can be estimated as

$$N = \frac{H_c \cdot A}{\Phi_0} = \pi D^2 H_c / 4\Phi_0, \tag{6.21}$$

where $A = \pi D^2/4$ is the cross-section area of a flux tube. Our calculations show that the number of flux quanta per tube was reduced from $N_1 = 209$ at the beginning of Region II to $N_2 = 171$ at the end of Region II. The corresponding reduction in the flux amount carried by tubes $\Phi_2/\Phi_1 = N_2/N_1 = 0.82$ is in excellent agreement with the ratio 0.83 estimated from the height of recorded pulses at the boundaries of Region II. This good matching between our estimate and the measurement gives us some confidence about the correctness of our arguments in developing this model.

After coming in contact at the end of Region II, the flux tubes start to coalesce into larger flux entities as seen in Region III. Long flux tube are followed by short ones as schematically is illustrated in Fig. 6.43d. The dynamics is then again similar to a dripping faucet where a nucleated drop determines the next drop formation, leading once more to a complex dynamics as in Region I.

6.8 Conclusions

In the "superconductong dripping faucet" experiment, using Hall probe microscopy in a non-scanning way, we have been able to detect in real time the individual passage of flux tubes along a 1D channel. The channel (3 μm wide, and 1 μm deep) was fabricated across of a lead strip. The nucleation and subsequent motion of the flux tubes along the channel was induced by applying a dc current along the strip. The detection of the flux tubes was done with a novel high speed Hall probe having a bandwidth of 5 MHz; the flux flow occurs in a frequency range of 10 kHz to 1 MHz.

A preliminary analysis revealed the complex character of the dynamics developed by the flux tubes flowing along of 1D channel in a type-I superconductor. Three distinct regions have been identified as the driving current (control parameter) is varied.

In the first region, the flux tube dynamics exhibits evident similarities with the classic dripping faucet. This is because, as in the dripping faucet experiment, the flux tubes adjust their flux amount mainly by affecting the nucleation condition at the strip edge. The deterministic behavior is governed by edge barrier changes due to the magnetic field of each nucleated flux tube.

The second region shows a highly periodic flux-flow. In this region the flux amount per tube is determined by the dynamics. Because the dynamics is now much faster the flux tubes undergo an average uniform field and this determines the same nucleation condition for each flux tube.

Finally, the third region is a very nonstationary regime of flux tubes, which adjust their flux amount through both nucleation process and dynamics. This is because the flux tubes coalesce along the channel, so they effectively interact with each other after nucleation. By changing their flux amount after nucleation, the flux tubes also change the nucleation condition at the strip edge for the next entries. This is quite different by the dripping faucet dynamics, where the water drops don't interact each other after detaching.

Overall the dynamics exhibited by the flux tubes flowing along a 1D channel is much more complex than for vortices in a type-II superconductor. We expect vortices to share some of the dynamics from the first region and the second region. The third region is not possible for vortices because, unlike flux tubes, vortices are single-quantum: they can not adjust their flux amount.

A nonlinear time series analysis was performed for selected segments of the first region of the flux tube dynamics. In this "dripping faucet" region, stationary and nonlinear sequences have been identified. Correlation dimension and Lyapunov exponent analysis reveal a deterministic scaling region in the phase space of these sequences.

We proposed a schematic model to explain the nucleation of flux tubes near the sample's edges. This model is consistent with the observed dynamics. However, a more realistic simulation of the flux tubes flowing along a 1D channel would include details like pinning along the channel, driving current variation over the width of the strip, and interactions between adjacent flux tubes.

Bibliography

[1] H. Onnes, Leiden Comm. **120** (1911).

[2] V. Ginzburg and L. Landau, Zh. Eksperim. i Teor. Fiz. **20**, 1064 (1950).

[3] M. Tinkham, *Introduction to Superconductivity*, International Series in Pure and Applied Physics, McGraw-Hill, Inc., New York, first edition, 1980.

[4] L. Landau, Sov. Phys. JETP **7**, 371 (1937).

[5] F. Haenssler and L. Rinderer, Helv. Phys. Acta **40**, 659 (1967).

[6] R. Goren and M. Tinkham, J. Low Temp. Phys. **5**, 465 (1971).

[7] R. Huebener, R. Kampwirth, and V. Rowe, Cryogenics **12**, 100 (1972).

[8] R. Goldstein, D. Jackson, and A. Dorsey, Phys. Rev. Lett. **76**, 3818 (1996).

[9] A. Dorsey and R. Goldstein, Phys. Rev. B **57**, 3058 (1998).

[10] A. Abrikosov, Zh. Eksp. Teor. Fiz. **32**, 1442 (1957), [Sov. Phys. JETP **5**, 1174 (1957)].

[11] V. Essmann and H. Träuble, Phys. Lett. A **24**, 526 (1967).

[12] P. L. Gammel et al., Phys. Rev. Lett. **59**, 2592 (1987).

[13] H. Hess, R. Robinson, R. Dynes, J. V. Jr., and J. Waszczak, Phys. Rev. Lett. **62**, 214 (1989).

[14] K. Harada et al., Nature **360**, 51 (1992).

[15] A. Moser et al., Phys. Rev. Lett. **74**, 1847 (1995).

[16] J. Kirtley et al., Phys. Rev. Lett. **76**, 1336 (1996).

[17] A. Oral, S. Bending, R. Humphreys, and M. Henini, Supercond. Sci. Technol. **10**, 17 (1997).

[18] P. Goa et al., Supercond. Sci. Technol. **14**, 729 (2001).

[19] F. London, *Superfluids*, John Wiley & Sons, New York, 1950.

[20] C. Gorter, Physica **23**, 45 (1957).

[21] L. Rhoderick and E. Wilson, Nature **194**, 1167 (1962).

[22] R. Huebener, R. Kampwirth, and J. Clem, J. Low Temp. Phys. **6**, 275 (1972).

[23] R. Huebener and D. Gallus, Phys. Rev. B **7**, 4089 (1973).

[24] R. Huebener and R. Kampwirth, Status Solidi (a) **13**, 255 (1972).

[25] R. Huebener and H. Watson, Phys. Rev. B **9**, 3725 (1974).

[26] D. Chimenti and R. Huebener, Solid State Commun. **21**, 467 (1977).

[27] B. Mühlemeier, J. Parisi, R. Huebener, and W. Buck, Phys. Lett. **102** (1984).

[28] J. Bardeen and M. Stephen, Phys. Rev. **140**, A1197 (1965).

[29] A. Schmid, Phys. Kondensierten Materie **5**, 302 (1966).

[30] C. Caroli and K. Maki, Phys. Rev. **159**, 306 (1967).

[31] C. Hu and R. Thompson, Phys. Rev. B **6**, 110 (1972).

[32] P. Leiderer, J. Boneberg, P. Bruell, P. Bujok, and S. Herminghans, Phys. Rev. Lett. **71**, 2646 (1993).

[33] K. Harada et al., Science **274**, 1167 (1996).

[34] T. Matsuda et al., Science **294**, 2136 (2001).

[35] U. Yaron et al., Nature **376**, 753 (1995).

[36] M. Hellerqvist, D. Ephron, W. White, M. Beasley, and A. Kapitulnik, Phys. Rev. Lett. **76**, 4022 (1996).

[37] A. Marley, M. Higgins, and S. Bhattacharya, Phys. Rev. Lett. **74**, 3029 (1995).

[38] F. Pardo, F. de la Cruz, P. Gammel, E. Bucher, and D. Bishop, Nature **396**, 348 (1998).

[39] M. Marchevsky, J. Aarts, P. H. Kes, and M. Indenbom, Phys. Rev. Lett. **78**, 531 (1997).

[40] A. Koshelev and V. Vinokur, Phys. Rev. Lett. **73**, 3580 (1994).

[41] C. Olson, C.Reichhardt, and F. Nori, Phys. Rev. B **56**, 6175 (1997).

[42] F. Nori, Science **271**, 1373 (1996).

[43] C. Olson, C.Reichhardt, and F. Nori, Phys. Rev. Lett. **81**, 3757 (1998).

[44] M. Baert, V. Metlushko, R. Jonckheere, V. Moshchalkov, and Y. Bruynseraede, Phys. Rev. Lett. **74**, 3269 (1995).

[45] V. Moshchalkov et al., Phys. Rev. B **54**, 7385 (1996).

[46] J. martin, M. Velez, J. Nogues, and I. Shuller, Phys. Rev. Lett. **79**, 1929 (1997).

[47] A. Bezryadin, Y. N. Ovchinnikov, and B. Pannetier, Phys. Rev. B **53**, 8553 (1996).

[48] A. Grigorenko et al., Phys. Rev. B **63**, 052504 (2001).

[49] S. Field et al., Phys. Rev. Lett. **88**, 067003 (2002).

[50] V. Metlushkoa, M. Baert, R. Jonckheere, V. Moshchalkova, and Y. Bruynseraedea, Solid State Commun. **91**, 331 (1994).

[51] V. Metlushko et al., Phys. Rev. B **60**, R12585 (1999).

[52] J. Wambaugh, F. Marchesoni, and F. Nori, Phys. Rev. B **67**, 144515 (2003).

[53] S. Anders, A. Smith, R. Besseling, P. Kes, and H. Jaeger, Phys. Rev. B **62**, 15195 (2000).

[54] N. Kokubo, R. Besseling, and V. V. P. Kes, Phys. Rev. Lett. **88**, 247004 (2002).

[55] A. Pruymboom, P. Kes, E. van der Drift, and S. Radelaar, Phys. Rev. Lett. **60**, 1430 (1988).

[56] P. Kes, N. Kokubo, and R. Besseling, Physica C **408**, 478 (2004).

[57] J. Wambaugh, C. Reichhardt, and F. Nori, Phys. Rev. Lett. **83**, 5106 (1999).

[58] C. Lee, B. Janko, L. Derényi, and A. Barábasi, Nature **400**, 337 (1999).

[59] J. Villegas et al., Science **302**, 1188 (2003).

[60] H. Kirchner, Phys. Lett. A **26**, 651 (1968).

[61] A. Chang et al., Appl. Phys. Lett. **61**, 1974 (1992).

[62] L. Vu, M. Wistrom, and D. Harlingen, Appl. Phys. Lett. **63**, 1693 (1993).

[63] A. Moser, H. Hug, O. Fritz, I. Parashikov, and H.-J. Güntherodt, J. Vac. Sci. Technol. B **12**, 1586 (1994).

[64] L. Vu and D. V. Harlingen, IEEE Transactions on Applied Superconductivity **3**, 1918 (1993).

[65] S. Bending, Advances in Physics **48**, 449 (1999).

[66] F. Bitter, Phys. Rev. **38**, 1903 (1931).

[67] H. Träuble and V. Essman, Phys. Stat. Solidi **18**, 813 (1966).

[68] H. Träuble and V. Essman, Phys. Stat. Solidi **25**, 395 (1968).

[69] H. Träuble and V. Essman, J. Appl. Phys. **39**, 4052 (1968).

[70] P. Alers, Phys. Rev. **105**, 104 (1957).

[71] L. Vu and D. Harlingen, IEEE Trans. Appl. Superconduct. **3**, 1918 (1993).

[72] J. Kirtley et al., Appl. Phys. Lett. **66**, 1138 (1995).

[73] C. Tsuei et al., Phys. Rev. Lett. **73**, 593 (1993).

[74] A. Oral, S. Bending, and M. Henini, Appl. Phys. Lett. **69**, 1324 (1996).

[75] Y. Martin and H. Wickremasinghe, Appl. Phys. Lett. **50**, 1455 (1987).

[76] H. Hug et al., Rev. Sci. Instrum. **64**, 2920 (1993).

[77] H. Hug et al., Physica C **235**, 2695 (1994).

[78] J. Chapman, J. Phys. **D 17**, 623 (1984).

[79] K. Harada et al., Jpn. J. Appl. Phys. **33**, 2534 (1994).

[80] J. Siegel, J. Witt, N. Venturi, and S. Field, Rev. Sci. Instrum. **66**, 2520 (1995).

[81] S. Field and J. Barentine, Rev. Sci. Instrum. **71**, 2603 (2000).

[82] R. Dingle, H. S. A. Gossard, and W. Wiegmann, Appl. Phys. Lett. **33**, 665 (1978).

[83] J. van Hulst, H. Jaeger, and S. Radelaar, Phys. Rev. B **52**, 5953 (1995).

[84] I. Tan, G. Snider, and E. Hu, J. Appl. Phys. **68**, 4071 (1990), free software is available at http://www.nd.edu/ snider.

[85] Y. Mori and N. Watanabe, J. Electrochem. Soc. **125**, 1510 (1978).

[86] X. Li and F. Peeters, Superlattices Microstructur. **22**, 2 (1997).

[87] R. Williams, *Modern GaAs Processing Methods*, Artech House Publishers Inc., Boston, 1990.

[88] E. Dantsker, S. Tanaka, and J. Clarke, Appl. Phys. Lett. **70**, 2037 (1997).

[89] G. Stan, S. Field, and J. Martinis, Phys. Rev. Lett. **92**, 097003 (2004).

[90] H. London, Proc. Roy. Soc. (London) , 650 (1935).

[91] P. de Gennes, *Superconductivity of Metals and Alloys*, Advanced Book Classics, Perseus Books Publishing, L.L.C., Reading, Massachusetts, third edition, 1999.

[92] J. Pearl, Appl. Phys. Lett. **5**, 65 (1964).

[93] R. Mints, V. Kogan, and J. Clem, Phys. Rev. B **61**, 1623 (2000).

[94] L. Helseth, Phys. Rev. B **66**, 104508 (2002).

[95] J. Clem, Bull. Am. Phys. Soc. **43**, 411 (1998).

[96] J. Clem, private communication to Stuart Field.

[97] G. Maksimova, Phys. Solid. State **40**, 1610 (1998), [Fiz. Tverd. Tela (St. Petersburg) **40**, 1773 (1998)].

[98] K. Likharev, Sov. Radiophys. **14**, 722 (1972).

[99] E. Zeldov, J. Clem, M. McElfresh, and M. Darwin, Phys. Rev. B **49**, 9802 (1994).

[100] E. Zeldov et al., Phys. Rev. Lett. **73**, 1428 (1994).

[101] M. Benkraouda and J. Clem, Phys. Rev. B **53**, 5716 (1996).

[102] V. Jeudy and D. Limagne, Phys. Rev. B **60**, 9720 (1999).

[103] M. Kupriyanov and K. Likharev, Phys. Solid. State **16**, 1835 (1974), [Fiz. Tverd. Tela (St. Petersburg) **16**, 2829 (1974)].

[104] G. Maksimova and I. Maksimov, Physica **C 282**, 2198 (1997).

[105] D. Vodolazov and I. Maksimov, Physica **C 349**, 125 (2001).

[106] B. Plourde, D. V. Harlingen, and D. Vodolazov, Phys. Rev. B **64**, 014503 (2001).

[107] J. Sok and D. Finnemore, Phys. Rev. B **50**, 12770 (1994).

[108] D. Kouzoudis, M. Breitwisch, and D. Finnemore, Phys. Rev. B **60**, 10508 (1999).

[109] M. Tinkham, *Introduction to Superconductivity*, International Series in Pure and Applied Physics, McGraw-Hill, Inc., New York, second edition, 1996.

[110] H. Weber et al., Phys. Rev. B **44**, 7585 (1991).

[111] R. French, Cryogenics **8**, 301 (1968).

[112] B. Goodman, IBM J. Res. Dev. **6**, 63 (1962).

[113] A. Kuznetsov and D. Eremenko, Phys. Rev. B **59**, 1507 (1999).

[114] T. Giamarchi and P. L. Doussal, Phys. Rev. Lett. **76**, 3408 (1996).

[115] M. Hastings, C. J. Olson-Reichhardt, and C. Reichhardt, Phys. Rev. Lett. **90**, 247004 (2003).

[116] R. Wördenweber, P. Dymashevski, and V. Misko, Phys. Rev. B **69**, 184504 (2004).

[117] I. Grigorieva et al., Phys. Rev. Lett. **92**, 237001 (2004).

[118] P. Anderson and A. Dayem, Phys. Rev. Lett. **13**, 195 (1964).

[119] C. Guthman, J. Maurer, M. Belin, J. Bok, and A. Libchaber, Phys. Rev. B **11**, 1909 (1975).

[120] R. Shaw, Aerial Press - Santa Cruz (1984).

[121] X. Wu and Z. Schelly, Physica D **40**, 433 (1989).

[122] X. Wu, E. Tekle, and Z. Schelly, Rev. Sci. Instrum **60**, 3779 (1989).

[123] R. Cahalan, H. Leidecker, and G. Calahan, Comput. Phys. **4**, 368 (1990).

[124] K. Dreyer and F. Hickey, Am. J. Phys. **59**, 619 (1991).

[125] J. Sartorelli, W. Goncalves, and R. Pinto, Phys. Rev. E **49**, 3963 (1994).

[126] R. Pinto, W. Goncalves, J. Sartorelli, and M. de Oliveira, Phys. Rev. E **52**, 689 (1995).

[127] G. SanchezOrtiz and A. SalasBrito, Physica D **892**, 151 (1995).

[128] A. D'Innocenzo and L. Renna, Phy. Rev. E **55**, 6776 (1996).

[129] A. D'Innocenzo and L. Renna, Phy. Rev. E **58**, 6847 (1998).

[130] L. Renna, Physics Letters A **261**, 169 (1999).

[131] K. Kiyono and N. Fuchikami, J. Phys. Soc. Japan **68**, 3259 (1999).

[132] B. Ambravaneswaran, S. Phillips, and O. Basaran, Phys. Rev. Lett. **85**, 5332 (2000).

[133] D. Chimenti and J. Clem, Phil. Mag. **38**, 635 (1978).

[134] K. Selig and R. Huebener, J. Low Temp. Phys. **43**, 37 (1981).

[135] K. Selig, D. Chimenti, and R. Huebener, Z. Physik. B **29**, 33 (1978).

[136] B. Mühlemeier, J. Parisi, R. Huebener, and W. Buck, J. Low Temp. Phys. **64**, 131 (1986).

[137] J. Clem, Phys. Rev. B **1**, 2140 (1970).

[138] J. Clem, J. Low Temp. Phys. **42**, 363 (1981).

[139] W. Buck, J. Parisi, and B. Mühlemeier, J. Low Temp. Phys. **55**, 51 (1984).

[140] J. Parisi, B. Mühlemeier, R. Huebener, and W. Buck, J. Low Temp. Phys. **60**, 45 (1985).

[141] M. Orlowski, W. Buck, and R. Huebener, J. Low Temp. Phys. **27**, 159 (1977).

[142] M. Sauerwald, *Designing High Speed Active Filters,*Application Note AO-26, National Semiconductor, http://www.national.com, 1997.

[143] D. Chimenti, H. Watson, and R. Huebener, J. Low Temp. Phys. **23**, 303 (1976).

[144] K. Koepke and G. Bergmann, Z. Phys. **242**, 31 (1971).

[145] G. Brandli and J. Olsen, Mater. Sci. Engr. **4**, 61 (1969).

[146] http://www.mpipks-dresden.mpg.de/~tisean/TISEAN_2.1.

[147] F. Takens, *Detecting Strange Attractors in Turbulence,* in *Dynamical Systems and Turbulence,* ed. by D.A. Rand and L.-S. Young, volume 898 of *Lecture Notes in Math.*, Springer, Berlin, 1981.

[148] T. Sauer, J. Jorke, and M. Casdagli, J. Stat. Phys. **65**, 579 (1991).

[149] T. Schreiber, Phys. Rev. Lett. **78**, 843 (1997).

[150] P. Grassber and I. Procaccia, Phys. Rev. Lett. **50**, 346 (1983).

[151] P. Grassber and I. Procaccia, Physica D **9**, 189 (1983).

[152] H. Kantz, Phys. Lett. A **185**, 77 (1994).

[153] M. Rosenstein, J. Collins, and C. D. Luca, Physica D **65**, 177 (1993).

[154] T. Schreiber, Phys. Rev. E **47**, 2401 (1993).

[155] A. Provenzale, L. Smith, R. Vio, and G. Murante, Physica D **58**, 31 (1992).

[156] J. Theiler, Phys. Rev. A **34**, 2427 (1986).

[157] T. Schreiber, Phys. Rev. E **48**, R13 (1993).

[158] H. Kantz and T. Schreiber, *Nonlinear time series analysis*, Cambridge University Press., Cambridge, UK, 1997.

[159] J. Clem, R. Huebener, and D. Gallus, J. Low Temp. Phys. **12**, 449 (1973).

[160] Y. Sharvin, Sov. Phys. JETP **6**, 1031 (1958).